Using a Smartphone for Point-of-Care Urinalysis of Chronic Kidney Disease

by

Shaymaa Akraa

Thesis

Submitted to Flinders University

for the degree of

Doctor of Philosophy

College of Science and Engineering

December 2018

Table of Contents

List of Figures

List of Tables

Abbreviations

ACR   Albumin-to-creatinine ratio

AIE   Aggregation-induced emission

AU   Artificial urine

AWB   Automatic white balance

BL   Smartphone-based bioluminescence

BSI   Backside illumination sensor

Car   Carotenoid

CCD   Charge-coupled device

CDS   Compact disk spectroscope

CFA   Colour filter array

Chl   Chlorophyll

CIELab   International Commission on Illumination

CKD   Chronic kidney disease

CMOS   Complementary metal-oxide-semiconductor

CMYK   Cyan, magenta, yellow, and black

CSPT   Computer screen photo-assisted technique

e-literacy   Electronic literacy

ESKD   End-stage kidney disease

FL   Fluorescent light

HDR   High-dynamic-range imaging

HSA   Human serum albumin

HSL   Hue-saturation-luminance

HSV   Hue-saturation-value

IaaS   Infrastructure as a service

IMHMS   Intelligent mobile health monitoring system

IRRI   International Rice Research Institute

ISO   International Standards Organization

ITE	Intensity transport equation
JSON	JavaScript object notation
KNN	K-nearest neighbour
L	Luminescence
LAMP	Loop-mediated isothermal amplification
LCC	Leaf colour chart
LED	Light-emitting diode
LOOCV	Leave-one-out cross-validation
MLP	Multi-layer perceptron
MSE	Mean square error
OpenCV	Open source computer vision
OTA	Ochratoxin A
PCA	Principal component analysis
PCR	Polymerase chain reaction
PLS	Partial least squares
POC	Point-of-care
QPI	Quantitative phase imaging
QUASR	Quenching of unincorporated amplification signal reporters
RGB	Red-green-blue
ROI	Region of interest
SPD	Silicon photodiodes
sRGB	Standard RGB
TPE	Tetraphenylethene
UV	Ultraviolet

Abstract

The main objective of this research is using a smartphone to provide early detection and periodic monitoring of chronic kidney disease (CKD) by analysing the human serum albumin (HSA) in urine using aggregation-induced emission (AIE) bioprobes. The intensity of AIE probe fluorescence increases as the HSA concentration increases. This knowledge is exploited by preparing precise graded concentrations of HSA that cover the five levels of CKD. AIE bioprobes are used to enhance the fluorescent intensity of the HSA solution. The solution is imaged within an imaging housing that ensures the same imaging conditions for all samples. The captured images are transformed from the red-green-blue (RGB) colour space into the hue-saturation-luminance (HSL) colour space to extract the intensity of the images. These intensity values are used to derive a linear regression between image intensity mean values and the corresponding HSA concentration. An important stage in the imaging process is the enhancement of the relation between image intensity and HSA concentration in order to avoid distortion. The colours of images that have been captured by one smartphone camera may not be equivalent to those that have been captured by other smartphones' cameras. The intensity values of images cannot be identical across various smartphone cameras due to differences in sensor response; therefore, a calibration process is applied to get a united intensity relation. The images are also affected by gamma correction that is applied by the smartphone's camera software after they are captured. This results in the intensity value relation to be non-linear. As the gamma values used during gamma correction is unknown or unpublished by the smartphone manufacturers, a blind inverse gamma correction technique is applied in order to estimate the unknown gamma values so that gamma corrected images are converted back to the raw images from which the original intensity values are extracted. Principle component analysis (PCA) is applied to calculate the linear regression between image intensity and HSA concentration, while K-fold supervised machine learning, where the best model is picked based on mean square error (MSE), is applied to predict the linear regression using the Least Squares Method. Both PCA and K-fold machine learning create an equivalent linear regression with trivial error. The predicted linear regression is used to determine the HSA concentration corresponding to the intensity value of the captured image.

Declaration

I certify that this thesis does not include any prior material submitted for a degree or diploma in any university without acknowledgment; and to the best of my knowledge and belief it does not include any prior material published or written by another individual with the exception of where due reference is used in the text.

Shaymaa Akraa

December 5th, 2018

Acknowledgements

First, I would like to thank God for inspiring me with patience and faith and for guiding all benevolent people to assist me.

Also, thank you to all who have instilled faith in my heart through their thoughts and tenets, especially to the Holy Prophet Mohammad and his honorable family.

I would like to express my sincere gratitude to the Australian government for supporting me to live a safe life with my daughter.

Also, I thank all the institutions that continued to support me to live and study in Australia.

I thank the gentleman supervisor, Dr. Haifeng Shen, for all his humanitarian attitudes, brilliant knowledge and beneficial supervision.

Also, I thank the supervisory team: Dr. Youhong Tang, Dr. Jimmy Li, and Dr. Gobert Lee for providing knowledgeable consults.

I would like to express my sincere gratitude to all my best friends and colleagues, and I'd like to thank especially:

Haroula Chronopoulos, Samra Qaraguli, Tran Tam Anh Pham and Rasiah Ravichandran.

Last but not least I would like to express my gratitude to Flinders University for providing an excellent environment for study, and I hope my humble effort to be a great representation of Flinders University.

Dedication

I would like to dedicate the fruit of my effort:

To the Iraq's martyrs,

All the heroes of the Iraqi army and the Popular Mobilization Forces (PMF), who defended my beloved and invaluable homeland.

Both the apple of my eyes, my beloved mother and my precious father, by whom I can see the hopefulness light to continue my way, and my little sweet angel, who has inspired me to face challenges and obstacles, my baby Zainab.

Publications

1   Shaymaa Akraa, Feng Guo, Haifeng Shen, Youhong Tang, Jimmy Li, Gobert Lee and Benzhong Tang. 2017."On the Feasibility of a Smartphone-based Solution to Rapid Quantitative Urinalysis using Nanomaterial Bioprobes", MobiQuitous 2017, the 14th EAI International Conference on Mobile and Ubiquitous Systems: Computing, Networking and Services, November 7–10, 2017, Melbourne, VIC, Australia.

2   Akraa, S, Tam, APT, Shen, H, Tang, Y, Tang, BZ, Li, J & Walker, S 2018, 'A smartphone-based point-of-care quantitative urinalysis device for chronic kidney disease patients', *Journal of Network and Computer Applications*, vol. 115, pp. 59-69.

1 Chapter 1: Introduction

1.1 Project Background

One of the most vital organs in the human body is the kidney. The main function of the kidney is to filter blood to remove waste and toxins. The kidney also has other responsibilities such as regulating blood pressure, balancing the amount of water in the body and activating vitamin D. Kidney failure occurs for many reasons, some of which are obvious like accident trauma that leads to loss of a significant amount of blood. Kidney failure can also happen silently, leading up to a patient's condition that worsens over time but with no evident medical symptoms. As such, chronic kidney disease (CKD) is described as 'the silent killer'. When a patient realises they have a CKD, mostly it is too late to undergo effective treatment. At this stage, the only remedial options are dialysis or kidney transplants. (Weiner et al. 2004).

CKD is a health problem worldwide because it shares a number of risk factors with other chronic diseases. Hypertension and diabetes increase the danger of cardiac disease; consequently, these chronic diseases are associated with declining lifestyle and are a major cause of death (Rauh et al., 2018). Smoking is linked to both cardiovascular and respiratory problems (Hamer & El Nahas, 2006) (Soria-Olivas, Martín-Guerrero, Redón, Tellez-Plaza, & Vila-Francés, 2015). More than 500 million people—7% of the world's population—have some form of CKD, causing millions of deaths every year (Couser, Remuzzi, Mendis, & Tonelli, 2011). In Australia alone, over 1/3 of the population aged over 65 are at risk of CKD; however, many of them are unaware of that danger (White, Polkinghorne, Atkins, & Chadban, 2010). Shortcomings in identifying CKD has caused many problems: underreported burden of CKD, hampered early detection of CKD, and limited application of therapeutic measures that retard progression of the disease to improve health results (Coresh, Astor, Greene, Eknoyan, & Levey, 2003).

CKD is defined as kidney damage or glomerular filtration rate (GFR) < 60 ml/min/1.73 m^2 for three months or more, irrespective of cause. Kidney damage in lots of kidney diseases can be ascertained by the existence of albuminuria at an albumin-to-creatinine ratio > 30 mg/g in two of three spot urine specimens. Kidney disease risk is classified into five stages, which are trace, 1+, 2+, 3+ and 4+, based on the level of GFR (Lenart, Mascarenhas, Xiong, & Flower, 2016) (Levey et al., 2005).

Early and regular testing of high-risk groups, such as people with diabetes, hypertension, cardiovascular disease, and family history of kidney failure, can prevent progression to end-stage

kidney disease (ESKD) that may result in dialysis, transplantation, and renal replacement therapy outcomes (Johnson, 2004) (Iseki, Ikemiya, Iseki, & Takishita, 2003). In Australia, age-standardized incidence of ESKD is significantly higher in Aboriginal and Torres Strait Islander people compared with other Australians mainly due to limited access to early detection facilities (Hoy, Wang, Baker, Mcdonald, & Mathews, 2001).

Urinalysis, also called urine diagnosis, is a standard process used to identify people early in the course of CKD when signs or symptoms are not necessarily evident. One method of urinalysis is by measuring the amount of HSA (Keane & Eknoyan, 1999). Serum protein normally occurs in high concentrations in the blood, but must not exceed more than a clinically normal threshold of 30 mg/dl in urine. Early stages of kidney damage allows a small amount of albumin to filtrate into urine and leads to the condition of microalbuminuria that presents in albumin levels of more than 30 mg/dl in urine (Winocour, 1992). Microalbuminuria urinalysis measures albumin concentrations. The urinalysis is conducted every few hours over a 24-hour window since a number of specimens can be more reliable (Ruggenenti, Gaspari, Perna, & Remuzzi, 1998). Analysis relies on massive and expensive bench-top urine analysis equipment and trained skills, which are generally only available in laboratory settings. Therefore a patient may need many visits to clinics or hospitals with long turnaround times for results (Agu et al., 2013) (Celler & Sparks, 2015) (Coskun, Nagi, Sadeghi, Phillips, & Ozcan, 2013).

In contrast to large, centralized analysis facilities, point-of-care (POC) testing has played an important role in transforming the healthcare industry. POC testing has a vital positive effect on patient care as well as improving operational efficiency. It is mentioned "*with a rising focus on providing cost-effective and timely medical care for ambulatory patients, POC laboratory testing has become one of the fastest growing areas in the medical field*" ("Global Urinalysis Market: Rising Demand for Point-of-care Testing Strongly Impacting Growth, Notes TMR," (2016, October 04)) . The advantages of POC testing are also reflected in urinalysis, with the segment poised to witness a big boom in the coming years. The increase in the elderly population, rapid progress in medical technology, and the increasing incidence of diabetes and kidney diseases all contribute to the global urinalysis market. The high cost associated with advanced analysers and the lack of laboratory staff are major barriers to the urinalysis market ("Global Urinalysis Market: Rising Demand for Point-of-care Testing Strongly Impacting Growth, Notes TMR," (2016, October 04)). In addition, POC testing is preferred to laboratory urinalysis as it can provide rapid results on site and is particularly suitable for screen for prevention, treatment monitoring, and patient self-testing. Existing POC urinalysis devices in the market use reagent strips and most

of them can only provide qualitative results (Of, 2013) (White et al., 2011).

The latest generation of smartphones is regarded more as a handheld computer rather than just a simple telephone. These smartphones are categorized based on their powerful on-board computing ability, high quality cameras, big screens, large memory and its open operating systems. All these reasons promote the applications to be developed. In addition, some studies have highlighted the successful use of smartphones to promote telemedicine and remote healthcare enabling smartphones to make healthcare more comfortable and affordable without compromising on the care's quality (D. Gupta, Khare, & Aggarwal, 2016) (Boulos, Wheeler, Tavares, & Jones, 2011). Smartphones now come equipped with high-resolution cameras enabling them to capture digital images that can be used to monitor changes over time for some diseases particularly in pathology, plastic surgery and dermatology (Landman et al.). However, there is a lack of confidence in the process of acquiring, saving, and sharing images in an efficient and secure way (Landman et al.). For both medical and scientific applications, an optical imaging requires precise quantification of characteristics like object size, colour and brightness. Although imaging by modern mobile cameras that have a high pixel density has made photography simple, there is still a barrier to acquiring precise quantified image data (Skandarajah, Reber, Switz, & Fletcher, 2014).

This research aims to improve quality of life by enabling the use of smartphones for early detection and self-monitoring of CKD. This requires the design and development of a smartphone-based urinalysis device that allows patients to conduct rapid, quantitative diagnosis anytime, anywhere and with any mobile device. This capability would reduce, or dispense with, the number of visits patients are required to make to clinics or hospitals and non-recourse to experts and would provide a cheaper and continuous means of monitoring CKD. The developed solution can estimate all concentration values within the five levels of CKD. This ability to calculate and estimate a concentration value is a key contribution of this research as most conventional methods for determining concentration depend on approximate calculations. Therefore, often, the obtained concentration values do not represent the real values.

The method for urinalysis using a smartphone is developed using several brands and models of smartphones to capture one or more images under ultra-violet (UV) light for different concentrations of artificial urine. The prepared samples of artificial urine contain varying amounts of HSA and BSPOTPE, which become emissive in the existence of HSA according to the aggregation induced emission (AIE) phenomenon. The concentrations of HSA in the samples were designed to reflect the various stages of CKD. The samples of artificial urine were poured into test tubes in order to be imaged under UV light using smartphones' cameras. The imaging

process of the artificial urine samples in the test tubes was conducted using an imaging housing that prevents ambient light while providing consistent UV light for all samples.

To deduce the amount of fluorescence intensity emitted from the artificial urine via the captured images, it is necessary to transform an image into an appropriate colour space such that through that colour space the image intensity can be extracted and calculated as an indicator of emitted fluorescence. These transformations are used to enable linear regression between intensity mean values and the corresponding concentrations of HSA because the fluorescence emission is directly proportional to the HSA concentration and that relation can be represented by a linear regression.

One major issue encountered was that photos taken using different smartphones with different camera characteristics resulted in images having different features. Therefore, there was a need to calibrate all smartphones used for capturing photos. This method is called "Ensuring Colour Consistency across Multiple Cameras".

Another problem encountered during imaging was the impact of gamma correction. Gamma correction is a power function that can change the luminance of the image to be brighter or darker to make the image clearer. Theoretically, applying the inverse of the gamma correction could eliminate the effect. However, because the gamma values of smartphone devices are unknown, there is a need to apply a technique that can estimate the gamma value that had been applied. This technique is called "blind inverse gamma correction".

From the image intensity values, we want to derive a regression that enables the prediction of HSA from an arbitrary intensity value. Principal component analysis (PCA) is one technique that can give us a predicted linear regression. K-fold supervised machine learning can pick the best intensity values with the least mean square error (MSE) to the best model. Both these techniques can give a predicted linear regression with an insignificant error between them. It is worth mentioning that the best model can be used not only to calculate the predicted linear regression, but also to calculate the predicted intervals for both the concentration and intensity with 95% prediction bounds for response values specified by the vector of both concentration and intensity respectively.

1.2 Contributions of the thesis

The proposed research introduces a novel method to measure HSA concentration over all levels of CKD. Moreover, the key contribution of this thesis is not only to determine the degree of CKD at point of care (POC) but also includes the ability to evaluate actual concentration values of

protein in urine using images captured by a smartphone camera. In the proposed research in this thesis, real colours of the captured image samples were used for colour calibration, while in traditional methods, colour calibration uses a colour checker with approximate colours, which often leads to inaccuracy in measured concentration values.

1.3 Outline of the Thesis

- **Chapter 1:** the chapter first provides information about CKD and its risk generally in the entire world and specifically in Australia. All these reasons motivated us to choose the proposed. Next, the chapter summarises other work that has been done by explaining the gaps that the proposed research will strive to fulfil. Lastly, the chapter introduces the proposed research method by explaining briefly the used materials, techniques, and devices.

- **Chapter 2:** the chapter presents a review of related work and procedures developed for therapy plans. This includes research highlighting smartphones as cheap and accessible adjuncts to improve POC.

- **Chapter 3:** the chapter firstly presents the key issues for smartphone-based urinalysis of CKD. Next, the chapter outlines research on novel solutions that may be employed rather than the traditional techniques. The driving force for employing a smartphone specifically for CKD urinalysis is its modern technical features and the versatility of a smartphone camera and cost. A smartphone-based urinalysis would present point-of-care testing for early detection and continuous monitoring of CKD.

- **Chapter 4:** this chapter first presents the review of related work of the previous imaging housing including imaging housing structures, components and material used to build them. The next part of the chapter explains the imaging housing design requirements of the proposed research, the imaging housing structure including the external housing, the tube holder and light-emitting diode (LED), and the imaging housing controls.

- **Chapter 5:** this chapter first presents the review of related work and highlights on the methods of collecting variant data via a smartphone camera, which is both a fluorescence source and detection device, to quantify the fluorescence and determine the data values. The next part of the chapter concentrates on preparing the samples and how the process of preparing samples takes into consideration choosing a proper concentration of samples within each grading of proteinuria. The last part of the chapter demonstrates and underlines the camera hardware calibration that must precede the process of capturing images that represents the final data to be processed.

- **Chapter 6:** this chapter first presents the review of related work of image processing and analysis, what the proposed method features are to process the captured images and how accurately the novel method can predict concentration values. Next, the chapter presents some theoretical concepts related to smartphone camera components, each of which has a particular function and can affect negatively on captured image's colours. The chapter proceeds with theoretical concepts that motivate the researcher to choose the appropriate techniques for processing the captured images including image colour calibration and gamma correction.

- **Chapter 7:** this chapter first presents the theoretical concepts about K-fold cross validation, Principal Component Analysis (PCA) and simple linear regression. For the model, the main function is to learn from the obtained data. Basically, both K-fold cross validation and Principal Component Analysis (PCA) are used to obtain eventually the best model where that best model is used to get a simple linear regression with 95% confidence limits for all points on the regression line. An inverse prediction procedure is used to predict HSA concentration values (s) at the value (s) of the Image Intensity. After that, the chapter presents a modelling correlation between image intensity and HSA Concentration that can determine the level of CKD based on the grading of concentration. Finally, the chapter presents a urinalysis mobile app that shows the quantified results and the level of CKD.

- **Chapter 8:** this chapter concludes the thesis by discussing the major contributions of this research and providing an outline of potential future work to improve and enhance the presented research effort.

2 Chapter 2: Review on Related Work

This chapter is a general review of research related to that presented in this thesis. Most previous research highlights how use of a smartphone at POC can improve quality of life, allowing regular and inexpensive monitoring of CKD while dispensing with frequent hospital visits and need for physicians. Related work is classified based on use of the smartphone as a platform, the detection method and applications in different fields.

2.1 Using Smartphone as a Platform

Portable computation and advanced communications are combined into one device, a smartphone that is able to run software applications. Smartphone user numbers have increased rapidly. More specifically, the number of healthcare professionals using smartphones is increasing. Mosa, Yoo, and Sheets (2012) classified healthcare technology according to their functions. Lots of medical applications are developed for healthcare professionals and patients. Therefore, smartphones in the healthcare field have become widespread. Medical applications make a smartphone very useful in medicine, especially in care. In addition, it is useful in clinical communication. A smartphone is regarded as a tool for patient instruction, disease self-monitoring, and remote patient monitoring. The proposed research in this thesis supports quality of life through the use of a smartphone for the early detection and self-monitoring of CKD. Patients can themselves conduct rapid quantitative diagnosis anytime, anywhere and with any mobile device.

Stankevich, Paramonov, and Timofeev (2012) concluded that a smartphone is one of the most important devices in our life because it has a computing interface and lots of sensors. These sensors, which are embedded within the smartphone, can be used in many fields; for example, environmental monitoring, social networks, safety and healthcare. They also surveyed the main uses of smartphone sensors in the healthcare field, classifying mHealth applications according to the type of sensor used. In addition, they explained the main advantages of these applications. The smartphone's camera is a very popular sensor and its main task is capturing images and recording videos. The use of the camera sensor can be expanded to react to real world objects, so images or video frames need to be analysed. In the proposed research in this thesis, high-resolution smartphone cameras can capture digital images to monitor changes over time for CKD patients. Captured image data is transformed into a convenient colour space, where an intensity band is extracted and analysed.

Shahriyar, Bari, Kundu, Ahamed, and Akbar (2009) developed Intelligent Mobile Health

Monitoring System (IMHMS), a mobile health monitoring system that uses a Wearable Wireless Body/Personal Area Network for collecting and mining data from bio-sensors worn by patients. This data is used to intelligently predict the patient's health status and to provide direct feedback to the patients. Mobile devices are used by the patients to participate in their healthcare anywhere, anytime. In research presented in this thesis, the smartphone is not only used for periodic monitoring of CKD, but also for early diagnosis.

U. Kim, Ghanbari, Ravikumar, Seubert, and Figueira (2013) pointed out that unclean water is a reason of sickness in children in developing countries. Methods for discovering disease causes are often costly in terms of time, money and effort, putting them out of reach of many developing countries. However, these countries have widespread adoption of smartphones. The authors presented an embedded microfluidic electrochemical sensor with a smartphone interface, which can detect a series of bacterial pathogens, enabling monitoring of water or point-of-care water monitoring within a suitable time and budget. The smartphone app compares and displays the measurement curve and baseline data. By using multiple calculations, the perpendicular distance for each curve can be calculated and compared to be assessed later for whether the distance is slightly different or exceeds the threshold. The proposed research in this thesis can calculate and show, in detail, all possible quantitative concentration values, whether low or high.

Patients with CKD can view complete treatment plans prescribed by doctors using their smartphones in a way that maintains privacy. Such applications would be easily available, reliable and simple to use to attract people with CKD to use them. Simplicity is the most important ingredient since it serves patients with low e-literacy. The term e-literacy stemms from "electronic literacy" that is a synonym for skills-based computer literacy. While health IT cannot replace the patient-doctor relationship, it can be an effective and efficient planning aid to provide therapy to patients with CKD. The proposed research in this thesis presents a novel method for not only viewing treatment plans, but also enabling patients to use a smartphone for the early detection and self-monitoring of CKD anytime, anywhere. These features would dispense with the multiple visits patients need to make to clinics or hospitals and no need for physicians and would provide an inexpensive and continuous means of monitoring CKD(Diamantidis & Becker, 2014) (Brandtweiner, Donat, & Kerschbaum, 2010).

2.2 Detection Methods

Kharrazi, Chisholm, VanNasdale, and Thompson (2012) proposed a method in which chemical strips are analysed using an application that processes photos taken by a smartphone at

predetermined times. Then, the results of the wet strips are compared with a colour map. Finally, it interprets the level of glucose, bilirubin, proteins, specific gravity, ketones, leukocytes, nitrites, urobilinogen and haematuria existent in the urine. The application results are beneficial for patients who have diabetes and kidney, bladder and liver problems, or for ferreting out the presence of a urinary tract infection. Thus, the application can provide good, understandable information. This information either has positive or negative results; for example, numbers or descriptors. If someone doesn't have knowledge that the existence of leukocytes can mark to a urinary tract infection, he can click on the tab of leukocytes for more information. The conception is to qualify people to know their health better by providing sufficient relevant information. Often a captured image does not perfectly match any colour in the colour map and as such a closest match has to be selected. This can result in a computed value over or under the real value. The solution presented in this thesis can precisely estimate all concentration values falling within the five levels of CKD via a machine learning technique that estimates concentration value from the intensity value of a captured image.

El Kaoutit, Estévez, García, Serna, and García (2013) concluded that the concentration can be detected by naked eyes due to change in the colour of the membranes. Also, the concentration of HG (II) can be quantified from millimolar to nanomolar range by analysing the information in the digital images that are captured after dipping the membranes in water. The Red-Green-Blue (RGB) colour model was used for processing, but RGB is psychologically non-intuitive and perceptually non-uniform. In the research presented in this thesis, the Hue-Saturation-Luminance (HSL) colour space is used. This does require a colour transformation from the RGB colour space into the HSL colour space. HSL is intuitive and efficient for real world applications (Jayashree, 2013).

Coskun et al. (2013) invented a new digital sensor, an albumin tester, attached to a smartphone. A smartphone captures images and analyses the fluorescence of the albumin in urine in test tubes as a means of calculating the albumin concentration in the urine. The camera of the smartphone captures the images using an outer plastic lens, which is inserted in front of the camera, facing the sample. The resulting sample images are processed by an Android application, installed on the smartphone, that computes the concentration of albumin. The designed app can exhibit three different qualitative levels, ''Normal'', ''High'', and ''Extremely High'', reflecting concentration ranges of 1 to 30 µg/mL, 30 to 200 µg/mL, and >200 µg/mL, respectively. The proposed research of this thesis can distinguish all five quantitative levels of CKD, corresponding to concentration ranges of 0 to 20 mg/dl, 20 to 30 mg/dl, 30 to 100mg/dl, 100 to 300 mg/dl and 300 to 1000 mg/dl respectively. The reason for that accuracy the source of the fluorescence with the wavelength of

470 nm generated in the urine comes from the combination of HSA (Urine) and AIE dye, which was excited by the outside fluorescent lamp with wavelength of 365 nm while in calculating the albumin, the concentration of HSA (Albumin) with the unit of µM/L.

Bourouis, Zerdazi, Feham, and Bouchachia (2013) developed an intelligent system for skin analysis to identify diseases by using an inexpensive smartphone with its integrated camera. Many advantages were presented for patients in rural, poor and developing countries such that, patients can scan, analyse and make regular skin check-ups. An Artificial Neural Network algorithm—Multi-Layer Perceptron (MLP)—was used to analyse images of 100 abnormal and 100 normal skin cases. The MLP algorithm is a feed forward neural network, i.e., it has one or more layers between input and output layer. Also, the data flows in one direction from input to output layer. This type of network is trained with the back propagation-learning algorithm. The captured image is represented in RGB mode by one-dimensional vector, which consists of red, green and blue data values. In the proposed research in this thesis, HSL instead of RGB is used since HSL is intuitive and efficient for real world applications. HSL has been adopted as a standard alternative to RGB due to its faster processing feature.

S. Gupta, Liaw, Vadakkepat, and Starmer (2015) proposed a means for making colorimetric measurements using a spectrophotometer prototype attached to a smartphone. The prototype was designed to work with a range of smartphone types and models. Colorimetry-based point-of-care diagnostics provides a lower cost technique, compared with large and costly traditional equipment, which are inappropriate for use in low-resource settings. High dynamic range imaging ensured images captured the necessary colour range for analysis. Images were stored in JPEG image format. The design of spectrophotometer prototype is different from the system described in this thesis. In our research, the imaging housing is used to block external light, while in their research, the test sample was placed between the spectrophotometer slit and an illuminating LED. Ambient light was not blocked and that may affect the image quality.

Qiu et al. (2017) contributed a method for diagnosing influenza A (H1N1) virus. A simple heating platform enabled a convection polymerase chain reaction (PCR) in a capillary tube. An LED was used to illuminate the reagent in the tube. Fluorescence was detected in real-time using a smartphone camera. Images were analysed via an algorithm running on the smartphone to interpret the detection results. This system allowed the H1N1 virus to be successfully detected in around 30 minutes using only 5V DC powered heater. In the research presented in this thesis, a UV light was placed to the side of the test to distribute the light equally and get homogenous fluorescence of images.

2.3 Applications in Different Fields

To improve patients' lives and minimize the expense for long-term hospitalisations, demand for telemonitoring techniques is increasing. Vacher, Istrate, Besacier, Castelli, and Serignat (2003) developed a smart audio sensor for a telemonitoring system. This sensor is provided with microphones to detect a sound incident like an abnormal noise or asking for help. The extracted sound information is sent over a CAN bus. The approach authenticity is replacing video camera monitoring with where the patients are uncomfortable with microphones for collecting and analysing sounds. They presented the hardware implementation, the software development and an evaluation of the algorithms used.

Soares, Lima, and Rocha (2017) developed a spot test to identify iodine in biodiesel using a smartphone camera. Two tubular fluorescent lamps illuminated the spot test in front of a white sheet to reduce the background reflectance and the impact of external light. The distance between the smartphone and the spot test paper was 5 cm. The images were taken with a smartphone camera and converted to RGB values. Controlled samples were prepared to develop a reference model from iodine concentration to image characteristics. This reference model was used in the analysis of biodiesel testing. In the research presented in this thesis, an imaging housing is used to avoid the influence of external light and background reflectance. The background colour of the housing is black since black is minimally reflective and absorbs all wavelengths in the visible range. The housing material is opaque in order to prevent all light passing through. This design provides a consistent environment for image capture and later analysis of reagent assays.

Rigon, Capuani, Fernandes, and Guimarães (2016) developed a process for using a smartphone to estimate total chlorophyll (Chl) and carotenoid (Car) content of soybean plants. Images captured of leaf discs were correlated with readings from a Chl meter used on the same leaf discs. The images were represented using the RGB, HSB and CIELab colour models. The smartphone camera proved sensitive enough to successfully resolve a wide range of Chl and Car content found in soybean leaves. The model developed mapping the image colour values and Chl meter readings provided a good representation allowing a smartphone to be used for accurate estimation of Chl and Car content. However, no housing was used in the imaging process so external light impacted the captured images, which led to a decline in accuracy and quality. In the research presented in this thesis, an imaging housing was used in order to block ambient light so that the image data is captured under consistent illumination conditions.

Moonrungsee, Pencharee, and Peamaroon (2016) proposed a method to identify iron in zeolites

prepared by incipient wetness impregnation. A calorimetric analyser was built using polystyrene foam. The imaging device was created to image a solution filled plastic test tube. Imaging conditions were controlled by wrapping the device with black plastic board and using a table lamp above the box for illumination. To further maintain consistency, the properties of the smartphone camera were maintained across multiple images: flash was disabled, the camera was set to a fixed-focus, International Standards Organization (ISO) control and White Balance (WB) were set to automatic, and a single image was captured at each trial. The smartphone was positioned in a straight line with the plastic test tube at a distance of 5cm to match the camera focus. The captured image stored in the JPEG image format and a program was built to read the intensity of the red, green, and blue colour values of the image. The program was configured with a calibration graph that was used to analyse the iron in the zeolites from the information available in the captured images. In the research presented in this thesis, lighting is the most important component since UV stimulation is required for human serum albumin (HSA) and BSPOTPE in the urine samples to fluoresce. The imaging housing was designed for consistent image capture by ensuring that the light source comes from the same side, angle and region and that the light is distributed equally over the entire test tube. Locating a lamp at the upper right corner above the box, as was done in the research described above, would not provide a homogenous light over the samples and will decrease the captured image quality. Also, camera settings like picture size, ISO, AWB and High-dynamic-range imaging (HDR) must be calibrated by choosing special settings to avoid image size differences, high sensitivity, colour-balancing problems and different program settings respectively.

Thanakiatkrai, Yaodam, and Kitpipit (2013) proposed the use of a smartphone camera integrated with an illumination system to be used in forensic investigations to estimate the age of bloodstains. Three smartphones/tablets, Samsung Galaxy S Plus, Apple iPhone 4, and Apple iPad 2, were used to image bloodstains on various substrates under various environmental conditions. A model was developed from images of controlled samples to correlate the colour values, particularly magenta, in the captured images with the time since bloodstain deposition. The Samsung Galaxy S Plus provided the best resolution and reliability of magenta across captured images. Imaging was conducted using a light box with a fluorescent lamp creating white light in the range 350 nm to 750 nm. An aperture was open at the top of the light box to allow the smartphone camera to image the sample inside. All imaging settings (white balance, ISO, focus, metering) of the Samsung Galaxy S were set to automatic. Images were captured in a 24-bit JPEG format at a consistent resolution. The images were represented using four colour models: RGB, CMYK, HSV and HSL. In the research presented in this thesis, camera settings like picture size, ISO, AWB and HDR are

calibrated by choosing specific settings to avoid image size differences, high sensitivity, colour-balancing problems and different program settings. Also, UV light stimulates the urine containing HSA and BSPOTPE to fluoresce. Consequently, the captured images, whether low or high fluorescence, suffer from gamma correction. A blind inverse gamma correction was applied to reverse the effect since gamma transforms the relationship from linear to non-linear. In the above research, the gamma correction effect was trivial or non-existent.

Solomon, Abdel-Raziq, and Vanapalli (2016) developed a stress-controlled microfluidic shear viscometer based on smartphone imaging. The method involved fluid being pushed into a micro-channel that had fixed pressure with a smartphone camera was used to track the fluid. The flow rate was determined by observing the slug propagation. The smartphone camera was used to record the motion of the fluid at 30 frames/sec and 1024p resolution. The video was analysed frame-by-frame using edge detection to find the fluid front. Movement across frames was used to calculate the distance travelled. Distance versus time was revealed to be a linear relationship. In the research presented in this thesis, samples to be imaged were pre-prepared and therefore could not be recorded as a movie. In addition, still images provide a higher resolution for analysis compared with video frames.

Wei et al. (2015) proposed the establishment of simple experimental setups for monitoring liquid surface waves to study the dispersion relation and for acquiring the liquid surface tension coefficient to validate the correlation between temperature and liquid surface tension coefficient. A smartphone camera was used to capture images for the surface wave paradigm, and wavelength was measured by software analysis based on image recognition. The simple experimental setup consisted of a plexiglass sink full of tap water, and a speaker linked with a signal generator, which provided the vibration frequency. In addition, the speaker's membranes were appended to a light bar, the end of which was submerged in the water. A flashlight was chosen as a light source that was placed under the sink and toward the vibration source. A piece of paper was placed on top of the sink. When the light beam, which was put under the sink, passed through the liquid, the image of the liquid surface wave was shed onto the paper. Therefore, a smartphone must be put in a place where it was parallel to the liquid surface. Also, the height of the smartphone must be adjusted until the wave image on the paper can be seen clearly from the camera. In the experiment, a simple light cannot provide a large contrast between dark rings and bright rings in an image. Images were processed using a sharpening process and adding a filter for detecting edges. The main function for the algorithm was to improve the accuracy of the wavelength. Two neighbouring dark rings close to the centre were chosen. Large contrast between dark rings and bright rings were beneficial

for reducing errors. The differences between the inner radius and the outer radius in two dark rings were calculated and the average obtained as a real wavelength. In the proposed research in this thesis, the function of the imaging housing is to block ambient light to capture images precisely while in the prior research, ambient light did not block light, so the dark rings of water were not sharp and clear enough during the imaging process.

Mei et al. (2016) suggested the use of a smartphone camera for imaging the luminescence variations on test paper and then quantitatively analysing pesticide theorem by making use of 3D printing technology. The incorporation of a smartphone with paper sensors has been gaining attention because of the accomplishment of quantitative and rapid analysis. However, smartphone-based conversional paper sensors have been inhibited by the lack of efficient methods to obtain luminescence signals on a test paper. Their proposed process was to drop different amounts of thiram on the test paper that was put into an attachment cavity to monitor luminescence intensity while images were captured for these different amounts of thiram on the test paper. Thereafter, the captured images demonstrated the increase of luminescence on the test paper with the increased thiram amounts. The blue colour intensity of the captured images was extracted to quantify the luminescence via a self-written Android program. While their method is somewhat similar to the proposed research in this thesis, the objective is different and so are the material, equipment and design of the smartphone's attachment. For instance, in our research, the light source is UV light while in their research the light source was laser light. Our samples are calculated, prepared and poured into test tubes while in their research, a piece of filter paper was used and immersed into the aqueous solution and ultrasonically stirred for 10 min. Then, the filter paper was removed from the solution and dried at 50 °C. Image luminescence intensities of test paper exhibited a descending linear relationship with the logarithm of thiram concentrations from 0.1 μM to 1 mM, while in our research, image luminescence intensities exhibit a cumulative linear relationship with the logarithm of bioprobe and HSA concentrations from 0.045 μM to 1.5 μM.

Priye and Ugaz (2016) developed a thermocycling system harnessing natural convection for rapid DNA amplification through the polymerase chain reaction (PCR). A simple prototype enabled PCR to be completed in about 15 minutes. Harnessing natural convection to actuate the PCR allowed the system to operate via a standard 5V USB powered from solar battery packs. This system allows a smartphone, with its camera, to provide immediate detection and analysis of PCR reagents deposited on disposable reactor cartridges. Fluorescence was generated using a diode gained from a blue laser pointer. An excitation and emission band-pass filter allowed a smartphone camera to detect successful PCR replication. An app on the smartphone was able to acquire,

quantify and analyse the image fluorescence. All components were housed in an exchangeable smartphone cradle that ensured exact alignment of whichever smartphone was being used. The ability of this system to deliver performance similar to current generation systems at reduced cost has expanded the use of PCR-based detection assays in settings where they are needed most. In the research presented in this thesis, a smartphone-based urinalysis device could dispense with the number of visits patients are required to make to clinics or hospitals and non-recourse to experts and would provide a cheaper and continuous means of monitoring CKD.

2.4 Advantages of the Proposed Research

In general, the advantages of the proposed research can be summarised as follows:

Rather than providing only treatment plans, smartphones can be used by patients themselves for early detection and self-monitoring of CKD, by frequent rapid quantitative diagnosis using any type of smartphone. Availability of this means of monitoring CKD would reduce the frequency of visits to clinics or hospitals and the need for appointments with physicians, thus improving quality of life for CKD patients.

In addition, for detection the new method is not based solely on the RGB colour space, but also extracts the intensity value of HSL colour space to deduce the corresponding HSA concentration, since HSL colour space is intuitive and efficient for real world applications. Moreover, the new method in this thesis can use a machine learning technique to relate the intensity values of captured images to estimate all HSA concentrations within the five levels of CKD.

3 Chapter 3: Key Issues and Solutions

The chapter firstly presents the key issues for smartphone-based urinalysis of CKD. Next, the chapter outlines research into novel solutions rather than the traditional techniques. The driving force for employing a smartphone specifically for CKD urinalysis is its modern technical features and the versatility of a smartphone camera and cost. A smartphone-based urinalysis would present point-of-care testing for early detection and continuous monitoring of CKD.

Traditional urinalysis of CKD measures the amount of Human Serum Albumin (HSA) in urine. The key to measuring HSA levels with a smartphone lies in the observation that the fluorescent intensity of urine under ultraviolet (UV) light increases with the concentration of HSA in the urine. The goal then becomes finding a method and a tool to sense the fluorescence intensity of urine under UV as this leads to identifying the HSA concentration in urine.

Fluorescence is defined as "*… a member of the ubiquitous luminescence family of processes in which susceptible molecules emit light from electronically excited states created by either a physical (for example, absorption of light), mechanical (friction), or chemical mechanism.*" (Herman, Lakowicz, Murphy, Fellers, & Davidson, 2009). Since the fluorescence of urine with an HSA concentration is visible with the naked eye, it can be imaged with a digital camera.

It is necessary to understand how a digital camera creates images in order to be able to accurately measure information from those images. An important building block of a camera system is the two-dimension array of pixels that forms the image sensor. Optics focus a scene to be imaged onto the image sensor, which converts the incident light into electrical signals. Colour imaging is achieved using a Colour Filter Array (CFA) between the image source and sensor. The electrical signals generated through different parts of the CFA are interpreted as different colours. Therefore, the sensor plays an important role in the process of creating a digital image (Wang, Wang, Xu, & Huang, 2017) (Matasaru, 2014). "*It is the image sensor that often limits ultimate performance*" (Wang et al., 2017). The sensors' response to the UV components of natural scenes are likely to be much greater in the human visible region (Pike, 2011) .

Modern technical features of smartphones such as the camera sensor, the ability to capture high-resolution images, large display area, multi-core processor with high computing ability, and, in some cases, an open-source operating system provide a computational platform for a modern diagnostic test device (Park, Han, Chun, & Yoon, 2017). In particular, the versatility of a smartphone camera sensor system enables it to take high-resolution images by transforming the

visible electromagnetic spectrum into digital images.

It is worth mentioning that the captured images for the urine fluorescence under UV contain much information such as sample size, colour, and intensity (Skandarajah et al., 2014). But the most important information is the fluorescence intensity of the urine in each image. The captured images are stored with reference to a particular colour space. However, that colour space may not be the most amenable to extraction of intensity information. It may be better to transform the images into a different colour space.

Digital images are typically captured and stored using the RGB (Red, Green, Blue) colour space (Ford & Roberts, 1998). However, RGB is not the best way to represent images in the real world as it is psychologically non-intuitive and perceptually non-uniform (Jayashree, 2013). The RGB colour space is also easily affected by any change in ambient light. The HSL (Hue, Saturation, Lightness or Luminance) colour space is more robust to ambient light changes (Juang, Tsai, & Fan, 2015). HSL is broken down according to physiological criteria: hue refers to the pure spectrum colour and corresponds to the prevailing colour as perceived by a human, saturation refers to the proportional purity, and luminance refers to the amount of light in a colour (Sanz, Museros, Falomir, & Gonzalez-Abril, 2015). The luminance value of an image is used to measure fluorescent intensity. While the HSL colour space provides better analysis across different ambient light conditions, it is highly desirable that all images are captured under similar circumstances. To that end, a physical image housing needs to be designed to control environmental effects and present an appropriate and consistent ambient environment during the imaging process. The imaging housing creates a dark environment that prevents ambient light, reflection and shadow effects on samples being imaged. The housing contains a UV light to illuminate the sample and to generate fluorescence in the sample. A filter is provided to improve the captured image quality. Clamp controls provide the ability to align the smartphone's camera, the sample and the UV light in a straight line that enables the smartphone's camera to capture images consistently across many samples.

Designing an algorithm that derives an HSA value from the image analysis requires data across a range of known samples. Obtaining this data from urine samples available from hospitals or clinics is a challenge due to the need to ensure reliability, precision and a sample space that covered the required HSA range, representing various levels of CKD, at regular intervals. To address this, artificial urine samples are created containing precise concentrations of HSA. In addition, the new BSPOTPE bioprobes containing tetraphenylethene (TPE) are added to the artificial samples. This enhances the fluorescence of the HSA when   illuminated by UV light and makes the imaging

process simpler. TPE is non-luminescent at solution state but becomes more emissive with the existence of albumin.

Kessler, Meinitzer, Petek, and Wolfbeis (1997) showed the Albumin Blue 580 fluorescence assay could define albumin even at low concentrations in urine. It relates to albumin and emits a strong red fluorescent light with albumin level determined by emission intensity at 616 nm (Sanz et al., 2015). Coskun et al. (2013) employed the same Blue 580 in their Albumin Tester for calculating the albumin concentration using a smartphone-based algorithm.

However, Tong ((2007)) and T. Chen et al. (2017) experimentally demonstrated that the discovery of BSPOTPE aggregation–induced emission (AIE) bioprobes is more effective than Blue 580 fluorescent assay for detecting HSA concentration in urine. The phenomenon of AIE leads to non-luminescent silole molecules starting to emit fluorescent light by restricting intermolecular rotation of the chromophoric molecules. The fluorescent light intensity of AIE bioprobes is directly proportional to aggregation extent. Their studies demonstrated that the new BSPOTPE bioprobes containing Tetraphenylethene (TPE), which is non-luminescent at solution state, becomes more emissive when it is in an aggregate state. For albumin concentration detection in urine, BSPOTPE has demonstrated higher sensitivity detection down to 1 nM. Figure 3- 1 illustrates the structure of the BSPOTPE.

Figure 3- 1: The structure of the BSPOTPE

Different cameras will often show different colour profiles in images of the same scene due to automatic colour enhancement. For example, contrast may be automatically increased in order to produce visually appealing pictures rather than a precise colour representation. Also, changing light conditions during image capture may produce large deviations in the captured colours even when using the same smartphone. Cameras of different brands, and even different camera models of the same brand, cannot exhibit substantially consistent colour responses, and these differences

can lead to considerable errors in scene interpretation (Ilie & Welch, 2005). A two-phase method is used to address this problem of colour consistency. The first phase is to calibrate the camera hardware, followed by the colour calibration of the images as a second phase.

The relationship between the HSA concentration values and the image intensity values is not a linear relationship. However, the real relationship should be linear because a fluorometer responds linearly to the HSA concentration within the five-concentration range, which we can call it as dynamic range. Whereas outside that range, the Intensity values can be saturated. The contradiction between the fluorescent intensity and its corresponding image intensity is due to the effect of gamma correction that occurs during image creation. The main reason for gamma correction is due to the fact that sensors respond linearly while human eyes respond nonlinearly. Manufacturers have found that there is a need to adjust the raw image from the linear sensor response into a nonlinear response in order to imitate what happens in the human visual system. It is worth mentioning that the human vision response varies. For instance, some people may feel the corrected image is brighter while others might think that image matches the scene. Manufacturers of sensors provide a special gamma lookup table based on the sensor. The main function of gamma correction used by a smartphone is to compensate and correct the errors caused by the non-linear response of modern CMOS (complementary metal-oxide-semiconductor) image sensors before saving a raw image as a compressed one (Cao, Pan, Zhao, & Wu, 2014). Gamma correction is able to automatically lighten shadows while darkening highlights in images. Gamma correction is a problem for our purpose, as we need an accurate representation of fluorescent intensity. Our solution is to apply a blind inverse gamma correction based on an estimate of the amount of gamma correction in an image.

After calibration and the blind inverse gamma correction are applied, the resulting images are assumed to reflect the raw images captured by the sensor. With the image intensity values and the associated HSA concentrations, our goal is to create a model of the data that can be used to derive an HSA concentration given any intensity value. The task is reduced to find a linear model where its image intensity values have the minimum mean square error (MSE) from all possible linear relations of the entire image intensity values using K-fold supervised machine learning.

K-fold machine learning is appropriate in scenarios that have low sample counts. It is able to reduce over fitting by dividing data into alternately exclusive subsets: a training set and a validation set. The model is trained with the training set and assessed with the validation set. Different data partitions create different training and validation sets. Averaging performance across these different partitions provides an estimate of generalised performance

(Nematzadeh, Ibrahim, & Selamat, 2015). Principal Component Analysis (PCA) is also used to model a linear relationship. PCA uses mathematical rules to reduce a number of correlated variables into a small number of uncorrelated principal components (Saad, Khalid, & Mohamed, 2015).

When the best model of the data has been picked, as assessed on the validation set, whose intensity values have the least mean square error (MSE), the last main issue is to represent the linear relationship with the predicted intervals for both of the predicted concentration values and the predicted Intensity values.

Figure 3- 2 illustrates the methodological steps used in this research. These steps are described in the following chapters, starting with designing the imaging housing and ending with modelling correlation.
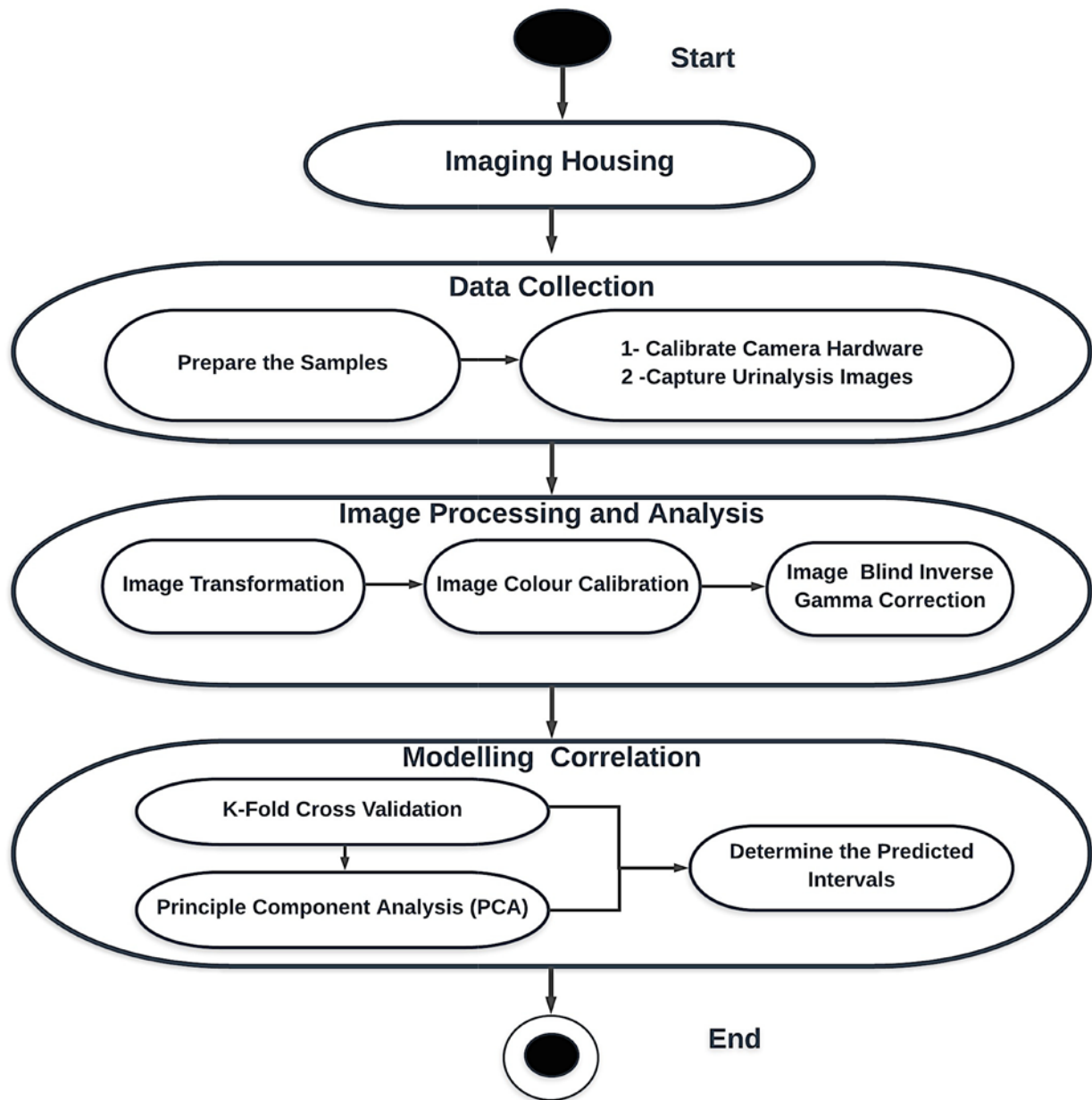
Figure 3- 2: Methodological steps of the proposed research

4   Chapter 4: Imaging Housing

This chapter first reviews previous work on imaging housings, including imaging housing structures, components and material used to build them. The next part of the chapter explains the imaging housing design requirements of the proposed research, the imaging housing structure including the external housing, the tube holder and LED, and the imaging housing controls.

4.1   Related Work

Lee, Jang, Jung, Jeon, and Ihm (2011) designed a pocket-sized colorimetric urine reader that could read and quantise multi-analysis tests into degrees and then send the data to a smartphone. It used an inexpensive Chromatic Light-Emitting Diodes (LED) as the light source and Silicon Photodiodes (SPD) as a light detector. The light signal data, in Red, Blue and Green, were converted into the hue (H) or the Y colour model and quantised accordingly. The proposed research in this thesis merges two devices into one: a mobile phone. This allows the same objective to be fulfilled without the use of the separate pocket-sized colorimetric reader since the mobile phone can be used to capture, process and analyse the images.

Webster et al. (2012) suggested the diagnosis of patients based on the analysis of patient's urine samples using a chemiresistor sensor. A mobile phone was used as an interface for a healthcare worker. Different gold nanoparticle chemiresistor sensors can distinguish between healthy and unhealthy urine. The project focused on three things: detection of disease using a sensor; data processing and analysis; and mobile phone software and user interface requirements. The proposed research in this thesis makes use of one device, a mobile phone, instead of two – a chemiresistor sensor and a mobile phone – to fulfil the same objective in such a way that is easier, faster and cheaper.

Wiens, Green, and Grecov (2014) contributed a device and technique to measure urine flow rate. The device consisted of a camera, a light source and a container. The camera was used to record a video of urine flowing in the container. Each frame of the recorded video could be analysed to identify fluid height, which was used to calculate fluid volume. The video was recorded at 29 frames/sec allowing flow rate to be computed. The proposed research in this thesis has a different objective in that it analyses the intensity values rather than the object dimensions of the images captured by a smartphone camera.

Y. Zhang, Wu, Zhang, and Ozcan (2016) designed a smartphone-based microscopy with an attached 3D printed housing containing a white LED behind a diffuser to give uniform illumination. A sample was placed close to the external lens, and the lens was placed next to the camera module of the mobile

phone. Colour calibration was achieved with a colour checker being the ground truth. The colour captured by the digital microscope was compensated via a mapping process to the actual colours defined by the ground truth. The colour calibration procedure included four steps: image normalisation and white balance, correction of light, correction of de-saturation and colour transformation. The proposed research in this thesis uses different imaging housing structure, components, and material due to the characteristics of the images to be captured. While colour calibration was performed using approximate colours using a colour checker in their research, the proposed research in this thesis uses real colours from captured sample images for colour calibration for "Ensuring Colour Consistency across Multiple Cameras".

Spyrou, Kalogianni, Tragoulias, Ioannou, and Christopoulos (2016) proposed a method of chemiluminometric genotyping development. A digital camera, either standalone or integrated in a smartphone, was used to perform the detection. The camera was used to detect emerging chemiluminescence from sensing areas on a test strip. A 3D printed smartphone attachment was created to house lenses to convert a smartphone into a portable chemiluminescence imager. The method was applied successfully to genotyping of real clinical samples. For the proposed research in this thesis, design of the imaging housing is different since the intent is to image liquid samples instead of solid strips.

Debus et al. (2015) developed two home-made platforms to assess levels of creatinine in human urine: compact disk spectroscope (CDS) and computer screen photo-assisted technique (CSPT). Despite the fact that several techniques have been proposed in order to accurately quantify the creatinine in human serum or urine, they require costly or complex equipment, sophisticated sample preparation and availability of skilled specialists. A digital camera mounted on a tripod was used to take photos, in a darkened environment, of absorption spectra of solutions. CSPT used a smartphone to record a video of 350 frames (14 frames/second) that was subsequently processed to create a 50-frame sequence. A region of interest in each frame was analysed to calculate a spectral fingerprint from the RGB intensity values of the pixels. Both CDS and CSPT output data were analysed with partial least squares (PLS) to create a regression model for determining creatinine concentration. Trade-offs were made between exposure time and light sensitivity (ISO) that impacted image quality. As the sensitivity to light increases, noise enters and blurs the overall picture. The camera's automatic mode was relied on to set photo capture parameters. In the proposed research in this thesis, all experiments carried out for HSA used UV light for stimulation. High quality single images were captured as opposed to analysing lower quality frames from a video recording.

S. C. Kim, Jalal, Im, Ko, and Shim (2017) developed a smartphone-based optical platform

for colorimetric analysis of blood haematocrit using a disposable microfluidic. The platform made use of the flash light on the smartphone in a way that minimised problems typically associated with flash photography, such as image-burning. The light from the flash was redirected through a semi-opaque diffuser. This platform was integrated into a white acrylic-imaging box that also minimised the impact of ambient light. The smartphone camera captured images of the microchannel inside the white box. The image was cropped, processed and analysed on the smartphone. In the proposed research in this thesis, all experiments were carried out using a UV light, instead of the smartphone's flash light, since UV light is required to excite HSA with AIE.

Cruz-Fernández, Luque-Cobija, Cervera, Morales-Rubio, and de la Guardia (2017) proposed image processing smartphone captured images of cold meat products (Salchichón, chorizo, Salami and cured ham) to determine fat content. Matlab was used to process images, and the average of the RGB values were calculated for each image. These averages were correlated with fat content values determined by the Soxhlet method from a series of commercial samples (Chmiel, Słowiński, & Dasiewicz, 2011). The smartphone camera was used in automatic mode and its flash used as a light source. An illumination chamber was created to capture photos under constant illumination conditions. The upper part of the chamber was covered by a flat sheet that had an aperture to allow the smartphone camera flash to strike a sample at an angle of 16°. Photos were captured of sample slices from both sides. Problems like reflections, glare and sensor saturation were minimised via controlling factors such as the colour within the illumination chamber, illumination conditions, background colour, inclination angle over the sample, and use of filters. In the proposed research in this thesis, the main colour of the housing material is black, which is minimally reflective, as it absorbs all wavelengths in a visible range. The housing material is opaque to prevent all light passing through. Important requirements for imaging are that the test sample location, the distance between the test sample and the camera, and light direction, angle and region.

("Zika Virus," 2017) suggested using the smartphone camera sensor instead of the traditional laboratory sample analysis equipment for Zika virus. An app with a simple interface was designed for users to operate the mobile device. Clinicians and specialists could use the device to make faster decisions about caring for, or isolating, affected patients and health authorities can be rapidly alerted so they can take measures to prevent the virus's spread. Traditional viral testing needs extensive power for heating and cooling the sample. The viral material detection also needs costly components like fluorimeters. The complexity and expense of traditional detection machines has been the main obstacle for moving analysis from laboratories into clinics where they are most needed.

A novel algorithm was designed in their research to allow for a smartphone sensor to act as a

fluorimeter for detecting QUASR—quenching of unincorporated amplification signal reporters—by loop-mediated isothermal amplification (LAMP) light signals. The role of LAMP was very simple: the user put the smartphone on top of the LAMP box and used an app that turned on the heater to begin the LAMP reaction. The testing period was up to 30-minutes, and the smartphone captured the sample. Then, the app used an image analysis algorithm to determine precisely the colour and brightness emitted from the LAMP reaction. The cost of a LAMP box prototype was largely dependent on the cost of the phone chosen for the test. The only requirements on the phone used are that it must have an optical sensor and be able to run the app. The cost of the smartphone used in the experiment was approximately $20. In this research, the role of the prototype LAMP is as a heater for samples controlled by the smartphone app, while the smartphone subsequently captures photos of these samples. In the proposed research in this thesis, a UV light is used to excite HSA fluorescence with the existence of AIE in urine and a smartphone is used to capture photos of these samples.

Cevenini, Calabretta, Tarantino, Michelini, and Roda (2016) report on the design, manufacture, and introductory assessment of the performance of a smartphone-based bioluminescence (BL) whole-cell toxicity biosensor. 3D printing was used to create cartridges for the samples and an adaptor for the smartphone. The adaptor, which supplied a dark box for imaging, was designed to fit the Samsung Galaxy Note II smartphone. An image-processing algorithm was implemented as an app for the phone. In the proposed research, the imaging housing is compatible with various smartphone models, sizes and types.

Archibong, Konnaiyan, Kaplan, and Pyayt (2017) developed a point-of-care mobile phone-based platform for characterising the level of patient haemolysis by imaging and measuring blood plasma colour. The platform integrates a mobile phone and an attachment to hold a sample. The sample holder had a slide-on lid and a ring slot to allow the smartphone camera to capture images of different samples under near-constant illumination conditions. After imaging the blood samples, a region of interest (ROI) is determined that captures the plasma portion of each image. The colour is averaged over the neighbourhood of adjacent pixels of the ROI. RGB colour is converted to CIELab values, where CIE L*a*b* is a colour model and space combo in which L is the image intensity, a is the red colour band, and b is the yellow colour band. A pre-computed calibration curve was used to map image details of the plasma into haemolysis groupings. In this research, the obtained results are only qualitative, while in the proposed research in this thesis, the obtained results are fully quantitative.

4.2 Imaging Housing Design Requirements

The imaging housing is built using rapid prototyping, utilising 3D computer design software, and is thus able to support a wide range of smartphones with different dimensions and camera positions such that consistent imaging conditions are maintained. The design of the housing is driven by these requirements:

- **Using Affordable and Accessible Manufacturing Technologies**

  The device must be usable and marketable to people with diverse abilities and be manufactured using technologies such as Laser Cutting and/or 3D Printing.

- **User-Friendly**

  The device should be easy to use by most users without prior experience or training.

- **Rapid and Robust**

  The device can produce accurate results in a short period of time.

- **Retesting**

  The device can be used to make multiple tests within 24 hours so that more precise results can be obtained.

- **Adaptable to Camera Position**

  The device must cater for smartphones having different camera positions, such as in the top-middle or top-left corner.

4.3 Imaging Housing Structure

The imaging housing design is illustrated in Figure 4- 1.
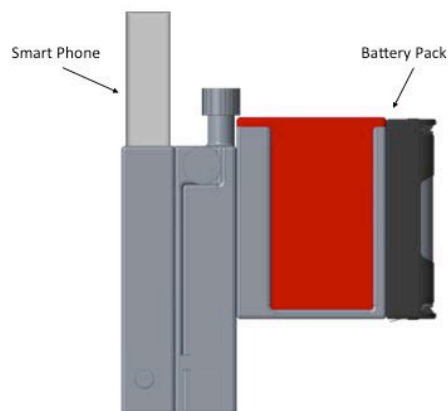
(a) Exterior design of the imaging housing
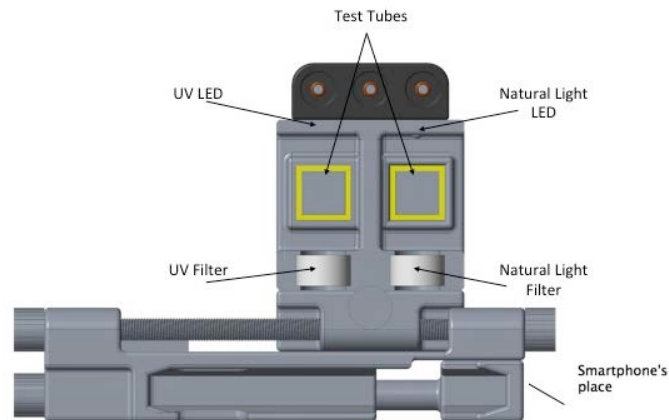
(b) Interior design of the imaging housing
Figure 4- 1: The imaging housing attached to a smartphone

4.3.1 External Housing

The external housing is an optomechanical black-box that is installed on the existing camera unit of the smartphone. The main function of this part is to hold the test tubes and to block ambient light. Therefore, this area is designed to be a dark space in order for the specimens to be imaged with complete isolation from ambient environmental effects. In particular, no light can enter and affect the reflected fluorescent image. It is also desirable that the only colour to be imaged comes from the fluorescence emitted from the test tube. The rest of the image should be a uniform colour. That drives the decision that the main material for the external housing to be black. Black is minimally reflective as it absorbs all wavelengths in a visible range. The housing material is opaque in order to prevent all light passing through. These design strategies provide the best opportunity for the image analysis of the reagent assays to be consistent, as shown in Figure 4- 1.

4.3.2 Tube Holders

The samples to be imaged and assessed are provided in test tubes. An important requirement is for the test tube's location within the housing to be consistent across tests and smartphones in terms of both the distance between the test tube and the camera and the alignment with the light source. The tube holders are manufactured based on that concept. The imaging housing contains two tube holders, each of which is used for a specific test. The left tube holder is specified for holding the tube that is filled with the BSPOTPE, while the right tube holder is reserved for testing creatinine (to be developed in the future), as shown in in Figure 4- 1(b).

4.3.3 LED light sources

The housing contains two LEDs as light source, one for each test tube holder. There is a UV light for the left tube holder, which is used to excite BSPOTPE. On the right side is a natural light LED, intended to light the creatinine in the future, see Figure 4- 1(b). It is important to note that the lighting is the most important component of the imaging housing because it generates the UV stimulation required for the urine containing HSA and BSPOTPE to fluoresce.

4.3.4 Batteries and optical filters

The housing accommodates two AAA batteries providing 3V. The main function for these batteries is the operation of the LED lighting sources; see Figure 4- 1(a). Space for optical filters is designed to provide a suitable exciting light for the urine solution.

4.4 Imaging Housing Controls

The location of the camera on a smartphone differs from one brand to another. The imaging housing is designed to be configurable to accommodate the smartphone being used, as shown in Figure 4- 2. With this design, external light is blocked out of the photo capturing process to ensure the quality of the result. In addition, controls are provided to align one of two tube holders, the lighting source and an optical filter with the smartphone's camera in order to provide a stable and consistent condition for capturing images, see Figure 4- 2. To support a variety of smartphones in the market, the imaging housing should be lightweight and adjustable to work with existing smartphones that have different dimensions and camera positions, as shown by Figure 4- 2.
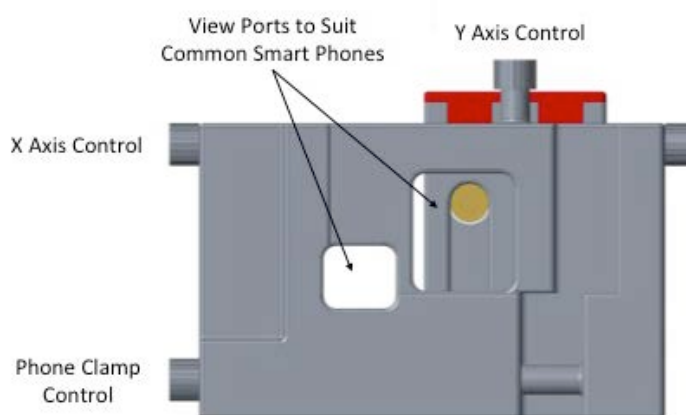
Figure 4- 2: Adjustable viewports and controls

5   Chapter 5: Data Collection

This chapter first reviews previous use of a smartphone as a fluorescence source and detection device, and how the smartphone camera can be used to measure fluorescence and thus determine data values. The second part of the chapter focuses on choosing a proper range of sample concentrations within each grading of proteinuria. The last part of the chapter demonstrates calibration of the camera hardware that must precede the process of capturing images to ultimately generate data.

5.1   Related Work

Karlen, Ansermino, Dumont, and Scheffer (2013) used a mobile phone camera to capture videos for estimating heart rate and blood oxygen saturation. The videos were imported into Matlab and the Red-Green-Blue (RGB) video formats were used for further processing. Each video was split into frames with RGB channels, and the mean values for each of R, G and B were calculated. The intensity mean values were represented as time series. In the proposed research in this thesis, the final graph will show the relationship between the image intensity mean values and the HSA concentrations in artificial urine instead of the intensity mean values in a time series. The collected data in the proposed research are a set of images of carefully prepared samples instead of a video of a continuously changing sample.

Oncescu, Mancuso, and Erickson (2014) suggested quantifying the concentration of cholesterol in blood using a smartphone. Blood glucose meters have been used for over a decade all over the world, but their use has been constrained because of the cost of strips, the difficulty of operation, and the inability to save or process the results. A smartphone application was developed to determine the concentration of cholesterol in blood. Accessories were developed to improve the results across different smartphones. The expanded use of smartphones, the development of image processing technology, and the sophistication of accessories have made cholesterol monitoring more precise and more useful for preventive care for cardiovascular disease. In this research, the prototype was designed to quantify the cholesterol colorimetric reaction that exists on a dry reagent test strip over the whole range of physiological cholesterol values. Also, the smartphone's flash was used to illuminate the strip as it can provide more uniform lighting for accurately imaging the colorimetric reaction on the test strip. The obtained image intensity values of the colorimetric reaction were low (<100 mg dl^{-1}) and high (>400 mg dl^{-1}) cholesterol concentrations. In the proposed research in this thesis, the obtained image intensity values of the HSA and AIE fall within a range of 0 to 20 mg/dl (trace), 20 to 30 mg/dl (1+), 30 to 100mg/dl (2+), 100 to 300 mg/dl

(3+), and 300 to 1000 mg/dl (4+) respectively.

Monošík, dos Santos, and Angnes (2015) developed a simple chromatographic paper-based colorimetric assay for food compound analysis. A coloured reaction on the chromatography paper surface could be analysed by the eye for screening and be recorded by a smartphone camera for quantitative analysis. The colour intensity of a region of an image was evaluated in the RGB colour space. The mean intensity of a homogeneous region and a blank unaffected area was computed. The final mean value was obtained by subtracting the intensity of a reaction area (purple) from the mean intensity of non-reaction area (blank). The quality of images depended on the photographer and the smartphone camera that varied from batch to batch. Ambient light was not controlled so discrepancies and shadows also fluctuated across the surface of the paper. The proposed research in this thesis uses an imaging housing avoids all problems caused by light discrepancies and shadows.

Bueno, Muñoz, and Marty (2016) proposed a method for quantifying concentrations of Ochratoxin A (OTA) using a smartphone camera to generate and detect fluorescence. Fluorescence occurs under stimulation from ultraviolet (UV) light and this fluorescence can be imaged using the smartphone camera. The presence of OTA generates blue fluorescence under UV light. The blue component of image samples is directly proportional to OTA concentrations. In the research presented in this thesis, increasing concentrations of has in urine, in the presence of AIE, results in increasing fluorescence under UV. Captured images were transformed from RGB into HSL to extract the luminance band as the best perceptive representation for urine fluorescence.

Yang and Zhan (2016) developed Quantitative Phase Imaging (QPI) for blood cell screening. Because QPI does not require dyeing or staining of the specimen it avoids the possible damage of cell. QPI was integrated into a smartphone platform that is used to image samples and analyse them. QPI is based on solving the intensity transport equation (ITE) from two images captured by the smartphone camera at two different levels. This method requires accurate handling/placement of the system. The two images have the problem of co-registration since they are captured at different times due to the need for moving the sensor between the two levels. However, living bio-samples change with time, so capturing images for these samples at different times would not be precise. A solution to this problem using two sensors and bulky beam splitting optics is not optimal for a smartphone-based system. Images were analysed using a Matlab based client-server architecture. All processing was conducted on a server under direction of a client running on the smartphone. Less than a second was required to generate one group of results. In the proposed research in this thesis, a thin mobile app captures the test image and sends it to the Urinalysis Web

Service provisioned by a cloud through Infrastructure as a Service (IaaS) for imaging processing and analysis.

5.2 Prepare the Samples

This section outlines the data collection process, which is important because inaccurate data collection can affect study results, potentially leading to invalid results. The process of preparing the sample HSA concentrations with AIE needs to be very precise.

(a) Samples in test tubes   (b) The stirrer device for bubble removal

Figure 5- 1: Sample preparation

5.2.1 Considerations in preparing samples

The process of preparing samples, including artificial urine, HSA and a solution of 50 µM BSPOTPE, requires laboratory equipment such as a pipette, test tube, stirrer and digital analytical balance. Preparation of the samples requires high precision as these samples are used as the base from which HSA concentration is correlated with image intensity value. As such, extreme care and cleanliness were practiced. This took some time as the people preparing the samples were untrained to use the equipment and in preparing samples. For instance, one of the difficulties was the use of a pipette to extract out a specific amount of BSPOTPE and HSA and mix them together in a test tube without losing any drops. Another obstacle was to get a homogenous chemical mixture such that the mixture did not contain bubbles that would impact the quality of captured images. Therefore, it was necessary to assess the chemical samples after preparation and decide whether that samples needed to be shaken by a stirrer or not, as shown in Figure 5- 1. On the point of hygiene, it was necessary to use a specific syringe to extract an appropriate urine sample volume, as well as wearing lab gloves, as shown in Figure 5- 2.

(a) A syringe to extract a proper amount of urine sample   (b) Using lab gloves and pipette

(c) The test tubes with plastic caps

Figure 5- 2: Hygiene and precision during measurement handling

Another important point is that the test tube used for preparing samples was equipped with a plastic cap to keep the solution from spilling. It must be noted that all accessories used for preparing samples were disposable including urine sample cup, gloves, syringe, and test tubes. A specified volume of BSPOTPE would be used for one experiment and then disposed of after finishing the experiment preparation.

5.2.2   Process of preparing samples

BSPOTPE is an environmentally stable and synthetically readily accessible FL (Fluorescent Light) probe for albumin detection and quantification (Tong, (2007)) . It is unperturbed by the miscellaneous bioelectrolytes in the artificial urine. The non-luminescent BSPOTPE becomes

emissive in the present of albumin. A set of experiments were conducted to understand how BSPOTPE responds to albumin concentration in Artificial Urine (AU), which was prepared as described previously (Chutipongtanate & Thongboonkerd, 2010), with pH of 6.8 and gravity of 1.010 g/ml. PBS (Phosphate-buffered saline) was made according to the cold spring harbor laboratory protocol (Cold Spring Harbor Protocols, [cited 23/11/2017]) All experiments were performed at room temperature. Stock solutions of BSA (Bovine Serum Albumin) and HSA with a concentration of 8.0 µM were prepared by dissolving appropriate amounts of the protein in the PBS buffer. The solution was stored in aliquots at −20°C.

Initially, sample solutions were prepared by choosing proper concentrations of HSA and BSPOTPE after these concentrations had been converted from mg/dl to µM units based on the molecular weight of HSA (66,437 g/mole) and the molecular weight of BSPOTPE (652 g/mole) to cover the entire range of proteinuria as shown in Table 5- 1.

Table 5- 1: The grading of proteinuria

Designation	mg/dL range	µM/L range	Number of samples
Trace	5-20	$7.5 \times 10-3 - 29 \times 10-3$	22
1+	20 - 30	$30 \times 10-3 - 44 \times 10-3$	15
2+	30 - 100	$45 \times 10-3 - 0.145$	21
3+	100 - 300	0.15 −0.42	10
4+	300 - 1000	0.45 − 1.5	22

BSPOTPE stock solution of 50µM concentration was prepared by dissolving 0.978 mg of BSPOTPE with 50ml distilled water. This is the best concentration of BSPOTPE as higher concentration of BSPOTPE would cause the FL intensity value to exceed the threshold of 1000 a.u. (Akraa et al., 2018). This solution was stored in darkness and in a fridge before use. Similarly, 10 µM of HSA solution was prepared by dissolving 0.0332g of HSA with 50 ml artificial urine. In addition, 0.3 µM of HSA was prepared by diluting the 10 µM HSA solution using the following well-known dilution equation to prepare Trace, 1+, 2+, 3+ and 4+ proteinuria concentrations more accurately: *Initial Concentration x Initial Volume = Final Concentration x Final Volume (commonly abbreviated as: C1V1 = C2V2).*

We prepared the samples using the stock solutions of BSPOTPE, HSA and artificial

urine. For example, a 0.0075 µM HSA concentration sample was prepared using 67.5 µl of 0.3µM HSA stock solution and adding 2632.5 µl of artificial urine. Table 5- 1 lists the number of samples for each grade of proteinuria whose corresponding concentration is reported below.

Table 5- 2: The grade of concentration, urine and BSPOTPE for (Trace) level

	Trace (5-20 mg/dl)				
	HSA(0.3)	V(HSA)	V(Urine)	V(BSPOTPE)	(BSPOTPE)
	(µM)	(µl)	(µl)	(µl)	(µM)
1	0.0075	67.5	2632.5	300	50
2	0.009	81	2619	300	50
3	0.01	90	2610	300	50
4	0.011	99	2601	300	50
5	0.012	108	2592	300	50
6	0.013	117	2583	300	50
7	0.014	126	2574	300	50
8	0.015	135	2565	300	50
9	0.016	144	2556	300	50
10	0.017	153	2547	300	50
11	0.018	162	2538	300	50
12	0.019	171	2529	300	50
13	0.02	180	2520	300	50
14	0.021	189	2511	300	50
15	0.022	198	2502	300	50
16	0.023	207	2493	300	50
17	0.024	216	2484	300	50
18	0.025	225	2475	300	50
19	0.026	234	2466	300	50
20	0.027	243	2457	300	50
21	0.028	252	2448	300	50
22	0.029	261	2439	300	50

Table 5- 3: The grade of concentration, urine and BSPOTPE for 1+level

	1+ (20 mg/dl - 30mg/dl)				
	HSA(0.3)	V(HSA)	V(Urine)	V(BSPOTPE)	(BSPOTPE)
	(µM)	(µl)	(µl)	(µl)	(µM)
1	0.03	270	2430	300	50

2	0.031	279	2421	300	50
3	0.032	288	2412	300	50
4	0.033	297	2403	300	50
5	0.034	306	2394	300	50
6	0.035	315	2385	300	50
7	0.036	324	2376	300	50
8	0.037	333	2367	300	50
9	0.038	342	2358	300	50
10	0.039	351	2349	300	50
11	0.04	360	2340	300	50
12	0.041	369	2331	300	50
13	0.042	378	2322	300	50
14	0.043	387	2313	300	50
15	0.044	396	2304	300	50

Table 5- 4: The grade of concentration, urine and BSPOTPE for 2+level

2+ (30 mg/dl - 100mg/dl)					
	HSA(0.3)	V(HSA)	V(Urine)	V(BSPOTPE)	(BSPOTPE)
	(µM)	(µl)	(µl)	(µl)	(µM)
1	0.045	405	2295	300	50
2	0.05	450	2250	300	50
3	0.055	495	2205	300	50
4	0.06	540	2160	300	50
5	0.065	585	2115	300	50
6	0.07	630	2070	300	50
7	0.075	675	2025	300	50
8	0.08	720	1980	300	50
9	0.085	765	1935	300	50
10	0.09	810	1890	300	50
11	0.095	855	1845	300	50
12	0.1	900	1800	300	50
13	0.105	945	1755	300	50
14	0.11	990	1710	300	50
15	0.115	1035	1665	300	50
16	0.12	1080	1620	300	50

17	0.125	1125	1575	300	50
18	0.13	1170	1530	300	50
19	0.135	1215	1485	300	50
20	0.14	1260	1440	300	50
21	0.145	1305	1395	300	50

Table 5- 5: The grade of concentration, urine and BSPOTPE for 3+level

3+ (100 mg/dl - 300mg/dl)				
	HSA(10µM)	V(HSA)	V(Urine)	V(BSPOTPE)	(BSPOTPE)
	(µM)	(µl)	(µl)	(µl)	(µM)
1	0.15	40.5	2659.5	300	50
2	0.18	48.6	2651.4	300	50
3	0.21	56.7	2643.3	300	50
4	0.24	64.8	2635.2	300	50
5	0.27	72.9	2627.1	300	50
6	0.3	81	2619	300	50
7	0.33	89.1	2610.9	300	50
8	0.36	97.2	2602.8	300	50
9	0.39	105.3	2594.7	300	50
10	0.42	113.4	2586.6	300	50

Table 5- 6: The grade of concentration, urine and BSPOTPE for 4+level

4+ (300 mg/dl - 1000mg/dl)				
	HSA(10µM)	V(HSA)	V(Urine)	V(BSPOTPE)	(BSPOTPE)
	(µM)	(µl)	(µl)	(µl)	(µM)
1	0.45	121.5	2578.5	300	50
2	0.5	135	2565	300	50
3	0.55	148.5	2551.5	300	50
4	0.6	162	2538	300	50
5	0.65	175.5	2524.5	300	50
6	0.7	189	2511	300	50
7	0.75	202.5	2497.5	300	50
8	0.8	216	2484	300	50
9	0.85	229.5	2470.5	300	50
10	0.9	243	2457	300	50

11	0.95	256.5	2443.5	300	50
12	1	270	2430	300	50
13	1.05	283.5	2416.5	300	50
14	1.1	297	2403	300	50
15	1.15	310.5	2389.5	300	50
16	1.2	324	2376	300	50
17	1.25	337.5	2362.5	300	50
18	1.3	351	2349	300	50
19	1.35	364.5	2335.5	300	50
20	1.4	378	2322	300	50
21	1.45	391.5	2308.5	300	50
22	1.5	405	2295	300	50

Afterwards, 300µl of BSPOTPE was added, from the 50µM stock solution, to each sample and was incubated for 15 minutes at room temperature. An ultrasonic bath was used to shake the prepared sample to obtain a homogenous solution without bubble.

5.3 Calibration of Camera Hardware

Different cameras show different colour profiles when they are set to automatic enhancement (Anthimopoulos, Gupta et al. 2016). Different camera makes and different models of the same make cannot substantially exhibit consistent colour responses. These differences can lead to considerable error in scene interpretation (Ilie and Welch 2005). Two calibration phases are used to address this problem. The first phase is to calibrate camera hardware. The second phase calibrates the colour of the images captured by the camera. Three mobiles, the Samsung S3, Samsung Galaxy Note 4, and Samsung Galaxy Note 3, are chosen for calibration before being used to capture images.

5.3.1 Picture size

Successive smartphone models typically bring increasing picture sizes. To ensure consistency, all phones are set to capture images at a fixed size: 3264x2448 (4:3) (8M).

5.3.2 International Standard Organization

The international standards organization (ISO) of a camera is a measure of the sensor sensitivity to light (Nour Abura'ed, 2016). It is also a value that can be set to change the gain of the sensor to make it more sensitive. One of the challenges is to capture a high quality image under low light

conditions. As a consequence, setting for a high-ISO will amplify the gain of the sensor. However, under low light conditions, setting a high-ISO causes the resulting image to be noisy because the ISO tends to amplify the sensor noise along with the image signal (Nour Abura'ed, 2016). ISO has the levels of, for instance, 100, 200, 400 and 800. A low ISO value results in lower noise in the captured image compared with a high ISO value. Therefore, a low ISO (100/200) is used to control noise of images under low light conditions.

5.3.3 Automatic White Balance (AWB)

In digital cameras, auto white balance (AWB) is a critical component (Tai, Liao, Chang, & Yeh, 2012) (B. Zhang & Batur, 2012). AWB algorithms try to account for changes in human visual sensitivity under different ambient illuminant conditions (Xiao, Farrell, DiCarlo, & Wandell, 2003). Many automatic white balance algorithms consist of two stages.

5.3.3.1 Illuminant estimation

This may be done explicitly, where it is chosen from a known set of illuminants, or implicitly, where it is estimated based on assumptions about the effect of such illuminants.

5.3.3.2 Image colour correction

This step results in an image as if it had been captured under a standard illuminant. The correction is often accomplished through an independent effect system of the R, G and B colours. This is known as the Von Kries hypothesis. It is achieved by adjusting the intensities of the red and blue colours only, although AWB cares about the ratio of the three colour signals (Au, 2013).

The AWB process can compromise colour information because it independently adjusts the gains of the three channels in order to meet the proprietary criteria about the colour composition of the scene. To avoid colour-balancing problems, automatic white balancing must be disabled during image acquisition to preserve a constant colour response (Ilie & Welch, 2005).

5.3.4 High Dynamic Range (HDR)

HDR is a process that is used to capture detail of both shadows and highlights in a single image. This is achieved by capturing multiple images at different settings to cover the range of light available in a scene from shadows, mid-tones, and highlights. These images are merged into one unified image with a massive tonal range (Au, 2013). However, each HDR program has different settings, so it is impossible to reproduce the same results for each image. Therefore, HDR must be turned off when capturing urinalysis images.

5.4 Capture of test images

5.4.1 Take photo of fluorescence emitted from the test tube

Each test tube containing a sample is placed in the test tube holder of the imaging housing. A smartphone is placed inside the phone holder of the imaging housing. The smartphone camera is aligned using the phone clamp control. This ensures the camera is lined up with the BSPOTPE tube holder, the UV lighting source and the optical filter. After being sure that the cuvette image is stably focused in the centre of the smartphone screen, the image can be captured. All sample concentrations are imaged with one smartphone before repeating the process with a different smartphone.

5.4.2 Obtain the results

The captured images of the urine fluorescence need to be processed to extract the fluorescent intensity information (Chapter 6). The final result of this processing is the prediction of HSA concentration, identification of CKD stage, and display of results on the smartphone screen (Chapter 7). The users can then consult healthcare staff in order to understand their health condition or get appropriate treatment.

6 Chapter 6: Image Processing and Analysis

This chapter first reviews methods in image processing and analysis, the proposed method features required to process the captured images and accuracy of the novel method to predict concentration values. Next, the chapter describes smartphone camera components, each of which has a particular function which influences the captured image colours. The chapter proceeds with concepts the researcher needs to understand to choose appropriate techniques for processing the captured images, including image colour calibration and gamma correction.

6.1 Related Work

Sicat et al. (2009) reported that the standard way of determining the level of protein, glucose, pH and specific gravity in urine was by wetting a test strip with the urine and then comparing the resultant change in colour with a standard set of reference colours. The researchers proposed a digital imaging and analysis process to conduct these tests. The imaging required consistent lighting conditions and other imaging characteristics, such as distance between camera and test strip, so that the images can be processed by their designed algorithm. The process of comparison was done by sending the captured image to a server, which cropped the coloured boxes of the reference colours into fixed dimension arrays. These boxes were scaled into pixels with an RGB colour for each pixel. The mean of each box was calculated and then compared with the captured image to choose the most similar sample box to the captured image. However, the RGB colour space had a shortfall because, in general, the colour of urine was affected by many factors, such as diseases or infections like haemolytic anaemia or Hepatitis, medicines like Rifampicin, fasting or having consumed food like beets or fava beans. The colour of urine may change to brown, red, or none in some cases like the urine of diabetes patients. So in these cases, the colour of the patient's urine absolutely will not be similar to any of the reference colours. Therefore, even similar lighting conditions and similar distance between camera and test strip may not necessarily produce precise results. The proposed method in this thesis depends on the intensity of colour that is extracted from HSL colour space. Then, the average intensity of an image is calculated in relation to the HSA concentration of the patient's urine. In addition, supervised machine learning is used to model and validate the correlation between them.

Velikova, Lucas, Smeets, and van Scheltinga (2012) suggested using a mobile phone to capture an image of a colour strip. The image should be cropped to reduce processing time and allow more images to be stored in the phone. The same process was used to create colour references to be compared with the imaged strips. Analysis and classification of the image used a histogram to

calculate the mean distance of the R, G and B values of the image with the reference colours. However, the RGB colour space was psychologically non-intuitive and perceptually non-uniform and therefore not very efficient when dealing with real world images. So the RGB model of the images was transformed to the HSL model, which is intuitive and efficient for real world applications (Sicat et al., 2009) and the effect was that an increase in the protein in a patient's urine resulted in a brighter image especially under UV light. The proposed research in this thesis also converts images from the RGB to HSL colour space with the L value representing the luminance of an image. The mean of the luminance across a captured image is used as its intensity value.

Martinez et al. (2008) developed a system that used paper-based microfluidic devices to run multiple assays simultaneously. A mobile phone camera was used to digitise the colour intensity of each colorimetric assay and communicate the data from the assay site to an off-site laboratory for analysis by a trained medical professional. The diagnosis will be returned to the healthcare provider. One example was calculating the concentration of glucose and protein in artificial urine. For the glucose assay, each image was converted into 8-bit grayscale, and a test zone was then chosen. The mean of pixel intensity was calculated. The same process happened with protein, but the images were converted into CMYK colour using the cyan channel that provided a larger dynamic range than grayscale as well as improved precision in the analysis. The intensity values of colours were compared with calibration curves, so the results of the assays were quantified. The researcher chose the CMYK colour space while the proposed research in this thesis uses the HSL colour space. This is important because the colour of urine may change for various reasons, for example, diseases, some types of food taken, or some types of medicines. Therefore, intensity is more important than actual colour. As the amount of protein in urine increases, the colour of the urine will be brighter, especially under UV light.

Chiu and Urban (2015) proposed a format for microscale chemical assays that do not require test tubes, microchips or microtitre plates. A reaction between to coalescing aqueous droplets in a Petri dish was detected via colorimetry, spectrophotometry, or fluorimetry under illumination from a monochromatic LED. Imaging was conducted in the dark using a transparent acrylic box covered with one layer of a drawing paper. The Petri dish was placed on black paper and an image captured under illumination for fluorometric detection and no illumination for chemiluminescence detection. Analysis was conducted on the RGB values obtained from the digital images. Raw images were saved in the JPEG file format while videos were saved in the MOV format. Individual frames of recorded movies were exported as JPEG files. The JPEG files analysed on a computer. The green channel of and image was used for the calorimetric and fluorometric measurements

while the blue channel was used for the chemiluminescence measurement. In the proposed research in this thesis, high quality images are captured one by one and their RGB values were transformed into HSL values. The luminescence (L) value of the images were used as representative of the intensity of captured fluorescence. Images were captured, rather than a movie recorded, due to better image quality.

Neumeyer et al. (2016) proposed a method to test the urine of pregnant women with a mobile application and an attached secure light box. These tests can help detect warning symptoms for common health risks early in pregnancy and increase preventative healthcare. The application used the mobile's camera to capture and digitise the colours within the urinalysis test strip. Then, it compared these colours with the baseline colours to determine the chemical levels in the urine. Colours were processed into hue, saturation and intensity value (HSV) and, for each, an average was calculated over the image. Each average value was correlated with the concentration of respective biological markers and stored as a reference. The captured colour values were compared with stored HSV colour values by calculating the differences between them. The summation of the differences were compared with the stored reference colour intensity. The minimum value between the actual and the expected colour intensity value was chosen as the corresponding concentration value. The method suggested in this thesis does not depend on exclusive actual and expected values to determine the concentration. It can estimate all concentration values from given images using a pre-trained mathematical model created using supervised machine learning techniques.

Yetisen, Martinez-Hurtado, Garcia-Melendrez, da Cruz Vasconcellos, and Lowe (2014) proposed a method of using a smartphone placed perpendicularly over an assay at a fixed distance. An app was calibrated for measurements of pH, glucose and protein. It defined reference colours and transformed and averaged the CMOS data into non-linear RGB values (Rc, Gc, Bc) for each pixel. Subsequently, the app linearised the RGB values (Rl, Gl, Bl). The linear RGB values were then converted to tristimulus values, X, Y, Z, which were finally converted into the 2D (x, y) CIE colour band. The app defined these values of intensity for concentrations and saved the results in an internal database. For calibration, the Euclidean plane equation specified the shortest distance from the measurement value to a calibration point, and the shortest two distances to the sample point was determined to find the corresponding concentrations. One of the main problems with this approach is that the concentration value determined may not be precise enough because it depends on measuring the shortest distance between two points such that the determined concentrations only represent approximate values.

Ginardi et al. (2014) proposed an intelligent method that helps people look after their health via self-urinalysis using a smartphone. The method of Lcolour sensing using a smartphone camera was designed to define the value of a reagent strip in a urinalysis dipstick. The change of the reagent strip's colour came from the reaction of the dipstick to the chemical contents of urine including pH, Protein, Glucose, Ketones, Leucocyte, Nitrite, Bilirubine, and Urobilinogen. Using a smartphone camera, the proposed method involved a framework for colour acquisition, including the colour management system, colour correction, colour matching, and quantification. In the colour management, RGB and CIELAB colour spaces were used for representing colours of an image, which were compared with reference reagent strips colours. However as the reference reagent strip values are limited, most of the captured image intensity values may not match any value.

Priye et al. (2016) developed a portable biochemical analysis platform for rapid field deployment of nucleic acid-based diagnostics using consumer-class quadcopter drones. In this method, a polymerase chain reaction (PCR) was created with one heater powered from a standard 5V USB source connected to a battery, solar panels, or hand crank. Fluorescence detection was achieved through a smartphone camera and an image analysis app. A clip-on magnifying lens was used to provide the camera a 10x optical zoom. The app developed for this system provided another 6x digital zoom. The focus and exposure of the camera were fixed to ensure constant lighting. A selected region of an image was transformed into a bitmap format containing 4 bits per pixel in the RGBA colour model. The average of green values of these bitmaps was used for analysis of fluorescence intensity. A gamma correction, with a gamma value of 2.2, was applied to the intensity values. The fluorescence of the analysed regions were normalised across images by subtracting the fluorescence of the background, captured at the start of the imaging session, in the region of interest. In the proposed research in this thesis, the selected region of a captured image was transformed from RGB to HSL to calculate the intensity values through the L band. For the non-linear relation of intensity values, blind inverse gamma correction was applied to the intensity values of images by estimating the unknown gamma values for each image individually.

Madooei and Drew (2016) proposed a method of enabling clinicians to use computer vision to aid in early detection of melanoma by dermatological image analysis (dermoscopy images, in particular). Cutaneous melanoma is one form of skin cancer that is life threatening. Mostly, advanced melanoma is regarded as incurable, but if it is detected and treated early, the prognosis is promising. Colour assessment is considered a basic issue for the clinical diagnosis of skin cancers. As a result of this diagnostic significance, lots of studies have either concentrated on or

used colour features as a constituent part of the analysis systems of skin lesions. In the image acquisition process, the accuracy of colour is necessary because imaging setup changes, like varying illumination or altering acquisition device, can result in dramatic changes in captured image colour. Therefore, an image processing algorithm, which depends on colour information, is subject to disruption. In an accurate colour calibration, it is necessary to provide an image with reproducible colours; such that, it is independent of the capturing system and the illuminant characteristics. This is often accomplished by finding a relation between the device-dependent output colour of a camera—usually in RGB—and a standard colour space like—the CIE *XYZ* or sRGB. The calibration process usually includes imaging a calibrated target, which is often a colour checker. A least-squares regression is performed in order to find a transformation matrix that converts the camera's RGB of each colour checker patch to the corresponding standard colour values. The reference colours were chosen from the standard colour checker patch in their research, while the proposed research in this thesis chooses images from one of the smartphones as the reference.

Collings et al. (2016) suggested detection of anaemia by measuring conjunctival pallor from digital images captured by a consumer camera and a smartphone. The objective was to develop a non-invasive screening test for anaemia. Images were captured of a patient's eye, with the lower conjunctive drawn down, and a colour calibration card. Automatic focus was used and photos were captured without flash. The white balance feature was used in the Panasonic LX5 digital camera with a white sheet paper used as a reference. Images captured using an iPhone also used automatic white balance and no flash and were saved in the JPEG file format. Reproducibility of results across different lighting conditions was tested using five conjunctival photos, across different ambient light settings, from each of the three healthy participants. When used for diagnosis, three photos were captured from patients using both cameras in ambient environment lighting. Each colour channel of the image data was multiplied by 200/MB, where MB is the mean brightness of the colour calibration card's white square. These values were merged to generate a 24-bit white-balanced image, which was saved as a TIFF file for future assessment by a clinician. In the proposed research in this thesis, three photos must be captured for test samples as reference colours and at least three photos must be used for calibration so that they can be analysed into R, G and B for each to get the calibration matrix. The calibration matrix is used to calibrate any new test sample that is captured by three photos.

Sari, Ginardi, and Sarno (2013) proposed a method for monitoring plant performance through comparing leaf colour with its corresponding colour in a Leaf Colour Chart (LCC) using a

smartphone camera. A relative colour calibration enabled the system to learn the colour chart automatically without relying on specific standard colours. A colour calibration was necessary for a smartphone before it can be used to capture and interpret leaf colour. The calibration process evaluated the camera performance with the operational lighting conditions and determined whether the smartphone camera can be used for leaf colour interpretation or not. In a calibration stage, the datasets were classified into three types: the standard LCC benchmark, the captured image for LCC's photo in typical lighting conditions, and the captured image in non-typical lighting conditions. The first type of photos were obtained from the IRRI's - International Rice Research Institute - website, which included six level ribbons of green colour and were used as colour reference data. The standard LCC was then printed on a glossy photo paper with a white background. After that, the captured photo from smartphone camera of the printed LCC was the second data. Two types of smartphones were used: Samsung Galaxy ACE and LG Optimus. With a good camera and good lighting conditions, the printed LCC can be reproduced digitally, i.e., it can produce a distinct colour for each level ribbon of LCC. Pictures were taken on the same day at varying times. Each colour level of the captured image was compared with its corresponding colour in LCC, and each colour was split into its basic colours R, G, and B. For data training via supervised classification, each colour element, mean and modus values were used. The classification was based on the nearest similarity to data test, i.e., K-nearest neighbour (KNN) classification was used for colour learning process in the RGB colour space. The test showed an average accuracy above the threshold value of 83%.

S. D. Kim, Koo, and Yun (2017) proposed a smartphone-based colorimetric pH detection method for point-of-care applications that uses a colour adaptation algorithm. The adaptation algorithm makes use of reference images captured together with pH strips. The algorithm normalises colours captured in images to account for changes in ambient light and automatic image correction that takes place within camera systems. The adaptation algorithm can produce calibrated colour information even if the camera characteristics change.

Dang, Cho, Kim, Kwon, and Chong (2017) suggested applying colour correction to images captured from different smartphones by automatically discovering differences in colour properties of captured images. This method was based on capturing and comparing images taken, without flash, from different devices of an X-rite ColorChecker Classic containing 24 colour patches. The process was evaluated using a Samsung Galaxy S6 and Motorola G4 with the mean, standard deviation and histogram of each RGB channel calculated for images captured. Least squares estimation was used to compute a colour correcting matrix from the image data. The original

image, denoted O, was represented as a 24 (number of colour patches) x 3 (number of colour channels) matrix. This image was processed, using the colour correction matrix, to create image P, also represented as a 24x3 matrix.

6.2 Image Transformation

Colour can be described using a variety of colour models. A simple colour model, and the one used by most camera sensors and visual displays, is to represent a colour as a mixture of Red, Green and Blue (RGB). However, RGB is unrelated to human perception. Moreover the time required for processing RGB is much longer than other colour spaces, especially for large-sized images. Also, an output image may have many colours, leading to patches in the resulting image (Lin, Liao, Hsu, & Wang, 2015).

Hue-saturation-luminescence (HSL) is widely adopted as an alternative to RGB due to fast processing time and its similarity to the traditional artist's colour theory. One of the most important features of HSL is that it can rearrange the geometry of RGB. Therefore, HSL is more perceptually pertinent than the Cartesian representation of RGB (Lin et al., 2015).

Image processing starts with transforming the captured images into the HSL colour space. This is done to capture the luminance intensity of these images. This process includes the identification of a region of uniform and homogeneous colour within the centre of the image (the same region must be selected consistently on all the captured images), the transformation of the RGB colour space of the selected region into the HSL colour space, and the calculation of the mean value of the intensity band of the HSL colour space from the selected region.

Image transformation is conducted through the steps described in Algorithm **1**.

Algorithm 1: $IMAGE\_L\ (image\_rgb)\colon MeanValue\_L$

Input: $image\_rgb$: a vector of standard RGB colour images captured by the smartphone

Output: $MeanValue\_L$: a vector of the mean intensity values (L band of HSL colour space)

1:    **for** $(\forall I_i \in image\_rgb)$ **do**

2:       $Icrp_i \leftarrow cropped\ (I_i, P, W, H)$ {(Image, Position, Width, Height): the same region is

                                        selected for all the captured images}

3:       $Icrp_i^{HSL} \leftarrow RGBtoHSL\ (Icrp_i^{RGB})$

4:　　　　$Icrp_i^L \leftarrow Icrp_i^{HSL\ (:,:,3)}$

5:　　　　$MeanValue_{i}\_L \leftarrow mean2(Icrp_i^L)$ {the average of Intensity for the cropped image}

6:　**end for**

7: **return** $MeanValue\_L$

Transforming image from RGB to HSL colour mode is conducted through the steps described in Algorithm **2**

Algorithm 2: $RGBtoHSL$ ($Icrp^{RGB}$): $Icrp^{HSL}$

Input: $Icrp^{RGB}$: a vector of cropped RGB colour image

Output: $Icrp^{HSL}$: a vector of HSL colour image

1:　R $\leftarrow Icrp^{RGB}(:,:,1)$

　G $\leftarrow Icrp^{RGB}(:,:,2)$

　　B $\leftarrow Icrp^{RGB}(:,:,3)$

2:　numi $\leftarrow$ ½*((R-G)+(R-B))

　　denom $\leftarrow$ ((R-G).^2+((R-B) .* (G-B))).^0.5

3:　　　　H$\leftarrow$ acosd(numi /(denom+0.000001)) {a small number is added in the

　　　　　　　　　　　　　　　　　denominator to avoid divide

　　　　　　　　　　　　　　　　　by zero }

4:　　　　If B>G then H$\leftarrow$360-H

5:　　　　　H $\leftarrow$ Normalize (H) {Hue: rescale H band to [0,1]}

6:　　　　　　S $\leftarrow$ 1 - (3/(sum($Icrp_i^{RGB}$,3)+0.000001)) * min($Icrp_i^{RGB}$,[],3) { Saturation }

7:	$L \leftarrow \text{sum}(Icrp_i^{RGB}, 3)/3$ { Intensity}

8: $HSL(:,:,1) \leftarrow H$

$HSL(:,:,2) \leftarrow S$

$HSL(:,:,3) \leftarrow L$

9: $Icrp^{HSL}: \leftarrow HSL$

10: **return** $Icrp^{HSL}$

6.3 Image Colour Calibration

Before presenting image colour calibration, we need to discuss the factors that impact the colours of an image from the moment when the image is captured by the smartphone's camera to that when the image is created and saved. It is worth clarifying that our discussion is only limited to the physical parts and algorithms of a smartphone.

6.3.1 Mobile phone camera

The addition of a camera to mobile phones has been a strong attraction to people. Combining telecommunication connectivity and photography has proven very popular in the history of both photography and mobility (Matasaru, 2014). Cameras have become an important feature of mobile phones and often serve as the main camera for many people (Cohen & Wang, 2014). Mobile phone cameras have developed many functions and some are equal to dedicated digital cameras (Q. Chen, Yan, Liao, & An, 2013). The process of creating a digital image from a camera is very similar to what happens in the human visual system. Light reflects from an object and enters the camera through a lens that focuses the light onto a filter and sensor. The sensor output is recorded as the digital representation of the image. The sensor plays a key function in the creation of a digital image (Matasaru, 2014). Generally, a mobile phone camera contains four parts: the sensor itself, the camera module, the image processing pipeline, or image signal processor (ISP), and, finally, the flash system (Peltoketo, 2016).

6.3.2 Sensors

Colour can be defined as: "*the visible electromagnetic spectrum reflected by an object and perceivable by a sensor within its detection range*" (Menesatti et al., 2012). Two dominant technologies are used to create the image sensor of a camera: Charge-coupled Device (CCD) and Complementary Metal-oxide Semiconductor (CMOS), as shown in Figure 6- 1 (Trappey et al.

2018) (Bravo et al., 2011). CCD and CMOS technologies have similarities and differences in their signal processing, performance and cost. Both are metal oxide semiconductors that convert light into electrical charges that are recorded as digital signals. Each pixel of a CCD generates an analog signal requiring an external analog to digital converter to create the digital signal. A CMOS sensor has each pixel generate a digital signal directly. Until recently, CCD has been more widely used, possibly due to its earlier and more mature development. While CCD images are theoretically superior, CMOS works faster and can be manufactured at a cheaper price and this has seen CMOS being overwhelmingly adopted as the sensor technology in all types of digital image-based systems (Lahuerta-Zamora & Mellado-Romero, 2017).
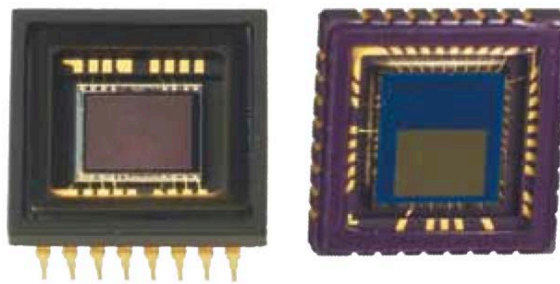
Figure 6- 1: Image sensors: CCD (left) and CMOS (right) (Trappey et al. 2018)

6.3.2.1 CCD

CCD cameras are widely used as imaging sensors in computer vision systems (Tsin, Ramesh, & Kanade, 2001). CCD sensors have advantages such as better light sensitivity and less noise over CMOS sensors. However, these differences have narrowed in recent years. Disadvantages of CCD sensors include: (a) the need for more electronic circuitry to integrate their analog components, (b) they are more expensive to produce, and (c) they can consume up to one hundred times more power than CMOS sensors. Excessive power consumption may cause heat problems in the camera, which in turn can negatively impact image quality. Figure 6- 2 illustrates a conceptual model of a CCD device (Trappey et al. 2018).
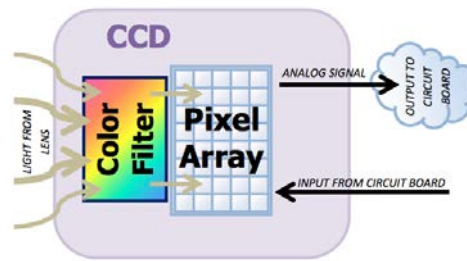
**Figure 6- 2: Parts of CCD - Charged-Coupled Device (Holms & Quach, 2010)**

6.3.2.2 CMOS

Early CMOS chips used for imaging purposes produced poor quality images due to poor light sensitivity. Modern CMOS sensors use more specialised technology that have resulted in improved image quality and light sensitivity. CMOS sensors have been used as a back-illuminated (BI) or a backside illumination (BSI) sensor, which uses a new layout of the imaging elements to boost the amount of captured light and, thereby, improve the performance in low light. The Toshiba Company has declared the launch of a BSI CMOS image sensor that introduces iris recognition into mobile devices. This increased security over passwords or fingerprints has allowed Toshiba to capture a market segment thanks to the introduction of its near infrared CMOS image sensor for iris recognition (Trappey et al. 2018) (Bigas et al. 2006).

The solid-state CMOS image-sensing device leverages attributes of CMOS technology ("Semiconductor- Memory Chip Companies: Patent Issued for Image Sensor, Operation Method Thereof, and System Including the Same (USPTO 9204143)," (2015, December 15)). CMOS chips have various advantages over CCD sensors. Recent refinements in the performance of CMOS image sensors have resulted in wide adoption in both non-portable home devices and in portable devices like smartphones and digital cameras. The CMOS chip integrates amplifiers and A/D-converter, which decreases the cost of cameras because it contains all the logic circuits required to generate an image. A related point to consider is that low power consumption in mobile devices is regarded as a high design priority, and research has occurred to decrease the power consumption of CMOS image sensors. "*Generally, there is a trade-off between reduced power consumption and increased performance, and in the field of CMOS image sensors, efforts continue to maximize the reduction of power consumption while maintaining necessary operational characteristics*" ("Semiconductor- Memory Chip Companies: Patent Issued for Image Sensor, Operation Method Thereof, and System Including the Same (USPTO 9204143)," (2015, December 15)). CMOS sensors are simpler at their external interfaces than CCD devices and hence have better integration possibilities. However, this comes at the cause of added circuitry inside the chip that can lead create a risk of structured noise such as stripes and other patterns. Other advantages

50

of CMOS sensors include: faster readout, lower power consumption, higher noise immunity, high-speed imaging, avoidance of blooming and smearing effects, random access of image data and a smaller system size. A conceptual model of a CMOS based device is shown in Figure 6-3.(Trappey et al. 2018) (Yoo, Lee, Choe, & Kim, 2007) (Bigas, Cabruja, Forest, & Salvi, 2006) (Choubey & Gouveia, 2014).
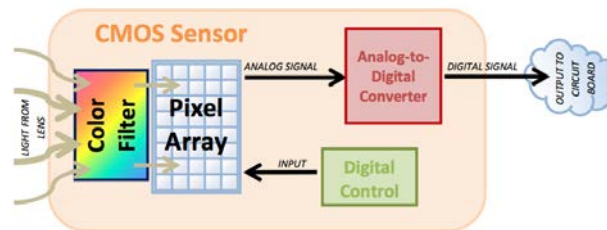
Figure 6- 3: Parts of a CMOS sensor (Holms & Quach, 2010)

6.3.3 Colour Filters

Image sensors, both CMOS and CCD, score the amount of light from brightness to darkness without any colour information, i.e., in monochrome. CMOS and CCD image sensors are referred to as being 'colour blind' (Trappey et al. 2018). A colour image is typically created by recording a Red, Green, and Blue value for each pixel. This was achieved, before the advent of colour detecting sensors, by superimposing three similar images captured by sensors sensitive to each colour channel (ON Semiconductor, 2015).

A colour filter array (CFA), or colour filter mosaic (CFM), is manufactured as a part of the image sensor and is positioned over the sensor pixels to capture colour information, as shown in Figure 6- 4. The colour filters absorb or pass light over a range of wavelengths allowing separate signal intensities to be captured, each containing information about a particular colour of light (Sumner, 2014; Tsin et al., 2001; Wang et al., 2017).

Typical CFAs used in image sensors include: Bayer filter, RGBE (red, green, blue, emerald-cyan) filter, CYYM (cyan, two yellow, magenta) filter, CYGM (cyan, yellow, green, magenta) filter, and RGBW (red, green, blue, white) filter, as listed in Table 6- 1. The Bayer-pattern or Foveon X3 colour filter pattern turns the image sensor into a natural multicolour receiver (Wang et al., 2017). A Bayer array filter (with RGB being the most common) has 50% green coverage and 25% each for red and blue arranged in alternating rows of red-green and blue-green (Tsin et al., 2001). The extra green coverage is due to the human eye being more sensitive to this colour. Bayer array and CMYG colour filters are illustrated in Figure 6- 5 (Trappey et al. 2018).
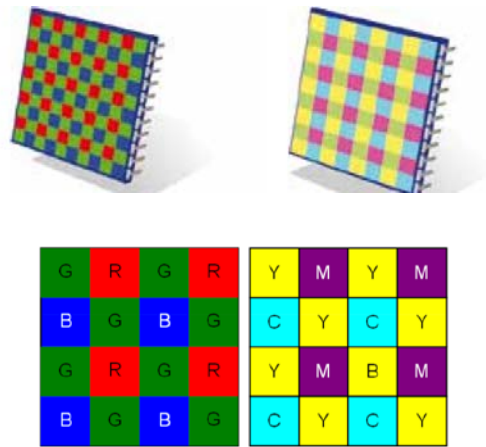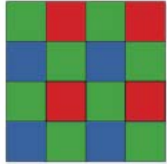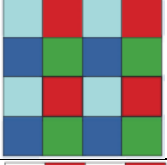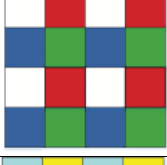
51
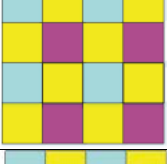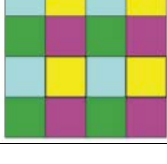
Figure 6- 4: Bayer array colour filter (left) and CMYG colour filter array (right) (Trappey et al. 2018)

Table 6- 1: Typical CFAs in image sensors (Wang et al., 2017)

Pattern	Name	Description	Pattern size
	GRGB Bayer filter	The Bayer pattern (green, red, green, blue) CFA is the most commonly used for image sensors	2×2
	RGBE filter	Red, green, blue, emerald-cyan CFA can reduce colour reproduction errors and record images that are closer to the natural signal	2×2
	RGBW filter	Red, green, blue, white CFA allows the sensor pixels to respond to all colours of light with more light being detected rather than absorbed	2×2
	CYYM filter	Cyan, two yellow, magenta CFA results in a more sensitive imager with less light absorption over each pixel	2×2
	CYGM filter	Cyan, yellow, green, magenta) CFA uses mostly secondary colours to allow more incident light to be detected	2×2
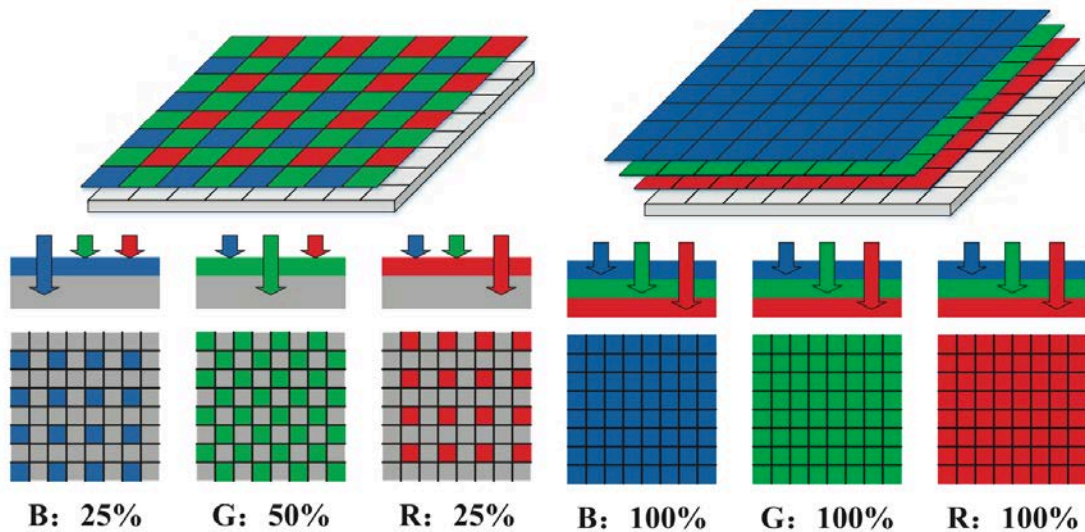
(a) Bayer pattern colour filter　　　　　　　　　　(b) Foveon X3 pattern colour filter

Figure 6- 5: Colour filter arrays in image sensors (Wang et al., 2017).

Data recorded at each pixel contains information about one only colour only. Which colour depends on the colour filter over that pixel. Information from all three basic colours is required at each pixel to create a colour image. Missing information can be recreated from information present in neighbouring pixels. The process of recreating missing colour information is called colour interpolation and this may require dedicated hardware to process the image data in real-time (X. Chen, He, Jeon, & Jeong, 2014). The Foveon X3 colour filter pattern image sensor can avoid some of these drawbacks. As shown in Figure 6- 5(b)*, "the Foveon X3 image sensor directly measures red, green, and blue colours at each location by stacking colour pixels on top of one another, increasing the sampling density in the image plane. It also enhances sharpness in luminance and chrominance, as well as robustness to colour aliasing artifacts*" (Wang et al., 2017).

Interpolation methods include Nearest Neighbour Interpolation, Bilinear Interpolation, and Bi-cubic Interpolation. The quality of the final image largely depends on the algorithm used. For this reason, many camera manufacturers hold their best colour interpolation algorithms as trade secrets that are not published (ON Semiconductor, 2015).

The colour values acquired by the colour interpolation process are called native colours. However, the native RGB data recorded by a sensor may not provide a true colour rendition of a scene due to other characteristics of the imaging system, such as the optics, the lighting conditions and the characteristics of the colour filters (ON Semiconductor, 2015).

As a result, an additional step, called colour correction, is performed to enhance the captures colours. In most cases, the native RGB is converted into a standard RGB (sRGB) colour space using a 3x3 colour correction matrix. sRGB is the standard colour format for most digital I/O imaging devices. Generating the correct values for the 3x3 colour matrix requires detailed knowledge in image science. However, the spectral response of the sensor like CCD is different from the spectral response of an output device. Also, the spectral response of the output device is not like the spectral response of the human eye (ON Semiconductor, 2015).

Therefore, the sensor of a digital camera plays an important role in determining colour characteristics. For a given camera, the essential colour quality of the images captured depends on the spectral characteristics of the sensor. The main reason for inter-camera colour variations is due to differences in the sensors' spectral characteristics. Even for cameras of the same model (Joshi & Jensen, 2004), imperfections in the fabrication of light sensors and filter arrays mean that spectral sensitivity functions cannot be assumed equal (Slavkovikj, 2011).

As a result, multi-camera systems, even if the cameras are of the same type, usually do not have consistent colour responses. Some researchers mention that the artifacts due to interpolation when the colours of images are not consistent is largely due to aperture and fabrication variations or electrical noise (Ilie & Welch, 2005) (K. Li, Dai, & Xu, 2011).

6.3.4 The Output of Sensors

Both human visual sensors and CCD sensors commonly used in scanners and video and digital cameras respond linearly to incident light spectra. Mathematical methods that deal with linear models can yield a relatively simple formulation of colour estimation (Sherman & Farrell, 1994).

However, CMOS image sensors may have non-linear pixel responses. That non-linearity can be a piecewise linear response, a logarithmic response or a blend of responses (Maddalena, Darmon, & Diels, 2005).

6.4 Calibration of Mobile Phone Camera Colour Images

A more accurate improvement must be applied to images captured with the already calibrated cameras. However, the effect of software improvement must be kept to a minimum in order to avoid amplifying noise, clamping and colour space distortion errors. Three different post-processing methods are found to improve results: linear least squares matching, a 3x3 RGB to RGB linear transform, and a general polynomial transform (Ilie & Welch, 2005).

A common way to account for the effects for inter-channel is a 3x3 RGB to RGB transform. The 3x3 matrix is calculated to transform the 24 colour samples of a camera image into the parallel colour samples of a target image. The matrix is the key solution to the over-constrained matrix system, as described by Equation (6-1).

$$
\begin{bmatrix} \vec{I_1} \\ \vec{I_2} \\ ... \\ \vec{I_{24}} \end{bmatrix}_{24 \times 3} \times \begin{bmatrix} t_{rr} & t_{rg} & t_{rb} \\ t_{gr} & t_{gg} & t_{gb} \\ t_{br} & t_{bg} & t_{bb} \end{bmatrix}_{3 \times 3} \simeq \begin{bmatrix} \vec{T_1} \\ \vec{T_2} \\ ... \\ \vec{T_{24}} \end{bmatrix}_{24 \times 3}
$$

(6-1)

This system can be rewritten as the linear system:

$$
\begin{bmatrix} \vec{I_1} & \vec{O_3} & \vec{O_3} \\ \vec{O_3} & \vec{I_1} & \vec{O_3} \\ \vec{O_3} & \vec{O_3} & \vec{I_1} \\ \vec{I_2} & \vec{O_3} & \vec{O_3} \\ \vec{O_3} & \vec{I_2} & \vec{O_3} \\ \vec{O_3} & \vec{O_3} & \vec{I_2} \\ ... & ... & ... \\ \vec{I_{24}} & \vec{O_3} & \vec{O_3} \\ \vec{O_3} & \vec{I_{24}} & \vec{O_3} \\ \vec{O_3} & \vec{O_3} & \vec{I_{24}} \end{bmatrix}_{72 \times 9} \times \begin{bmatrix} t_{rr} \\ t_{rg} \\ t_{rb} \\ t_{gr} \\ t_{gg} \\ t_{gb} \\ t_{br} \\ t_{bg} \\ t_{bb} \end{bmatrix}_{9} \simeq \begin{bmatrix} \vec{T_1^T} \\ \vec{T_2^T} \\ ... \\ \vec{T_{24}^T} \end{bmatrix}_{72}
$$

(6-2)

$$ \Leftrightarrow A \times \vec{t} \simeq \vec{T} \Leftrightarrow \simeq Pinv(A) \times \vec{T} $$

The matrix elements are grouped into vectors as follows:

1. The first vector denotes the colour of the camera image samples in the format I = [Ir, Ig, Ib],
2. The second vector denotes the colour of the target image sample in the format Ts = [Trs, Tgs, Tbs],
3. The third vector denotes the 3-component null vector in the format O = [0, 0, 0].

The term t_{xy} captures how much the input from colour channel x contributes to the output of colour channel y. Singular value decomposition is used to compute the pseudo-inverse of matrix A and back substitution to compute the solution t $\vec{t}$.

Despite the fact that the RGB to RGB matrix transform calculates for inter-channel effects, it does not have a translation component. Also, it does not compensate for nonlinearities in the response

functions. To account for these remaining shortcomings, a general polynomial transform is devised. The 3x3 RGB to RGB transform is generalised to a non-linear transform by introducing higher degree terms to recompense for the nonlinearities in the response functions and a bias term to allow translations. The general formula for colour c $\in$ {r, g, b} of sample s is:

$$\sum_{k=1}^{D} \left(t_{rc_k} Ir_s^k + t_{gc_k} Irg_s^k + t_{bc_k} Irb_s^k \right) + t_{c0} \simeq T_{C_s} \tag{6-3}$$

Where D is the degree of the polynomial approximation; Ir_s^k , Ig_s^k and Ib_s^k are the red, green and blue values for camera image sample s, raised to power k, respectively; T_{C_s} is the value for colour channel c of the target image sample s; t_{xc_k} is the polynomial coefficient of the kth order term that designates how much the input from colour channel x $\in$ {r, g, b} subscribes to the output of colour channel c; t_{c0} is an additional term that allows translating the output of channel c.

Our experiments have shown that D = 2 is sufficient to fulfil the level of accuracy required by typical applications. For D = 2, we can re-write Equation (6-3) for all the 24 samples of the colour chart into equivalent matrix form as follows:

$$\begin{bmatrix} Ir_1 & Ir_1^2 & Ig_1 & Ig_1^2 & Ib_1 & Ib_1^2 & 1 \\ Ir_2 & Ir_2^2 & Ig_2 & Ig_2^2 & Ib_2 & Ib_2^2 & 1 \\ \dots \dots \dots \dots \dots \dots \dots \dots \dots \dots \dots \dots \dots \dots \dots \dots \\ Ir_{24} & Ir_{24}^2 & Ig_{24} & Ig_{24}^2 & Ib_{24} & Ib_{24}^2 & 1 \end{bmatrix}_{24 \times 7} \tag{6-4}$$

$$\times [t_{rc1} \quad t_{rc2} \quad t_{gc1} \quad t_{gc2} \quad t_{bc1} \quad t_{gc2} \quad t_{r0}]_7^T$$

$$\Leftrightarrow B \times \overrightarrow{t_c} \simeq \overrightarrow{T_C} \Leftrightarrow \overrightarrow{t_c} \simeq Pinv(B) \times \overrightarrow{T_C}, c \in \{r, g, b\}$$

Each matrix equation is solved using singular value decomposition in order to compute the pseudo-inverse of matrix B and back substitution to compute the three solutions $\overrightarrow{t_r}$, $\overrightarrow{t_g}$ and $\overrightarrow{t_b}$. It is worth mentioning that matrix B is the same for all three-color channels; therefore, there is a need to perform the inversion of the matrix only once (Ilie & Welch, 2005).

Algorithm **3** describes the image calibration process for one smartphone. Images captured by each smartphone needs to be individually calibrated.

Algorithm 3: $ImgCal(img_{rgb}, img_{scr})$: $im\square_{\square\square\square}$

Input: img_{rgb}: vector of standard RGB colour images captured by the smartphone

Input: img_{src}: vector of urinalysis images captured by the smartphone

Output: $im\square_{\square\square\square}$: vector of calibrated urinalysis images for the smartphone

1: $\square\square\square_{\square\square\square} \leftarrow \overline{img_{rgb}} \times \square\square d_{\square\square\square}$ {$\square\square d_{\square\square\square}$: vector of standard RGB colours}

2:    **for** $(\forall \square_{\square} \in img_{scr})$ **do**

3:       $im\square_{\square\square\square}[\square] \leftarrow \square_{\square} \times \square\square\square_{\square\square\square}$

4:   **end for**

5: **return** $im\square_{\square\square\square}$

6.5 Gamma Correction

The human vision system, which includes the mechanism of the human eye and visual perception, is considered to be the basis for traditional imaging. Light is electromagnetic radiation that makes vision possible via the human eye. However, the human eye can sense only a limited band of the electromagnetic spectrum, between 380 and 780 nm. This is known as the visible spectrum.

In a camera system, the process of creating the captured image for any scene is similar to the process of creating an image for that scene in the human visual system. In a camera, light reflected from an object enters the camera through a lens. The function of the lens is to focus the light onto a set of a sensor and filter. The light is recorded as electronic signals generated by the sensor. Therefore, the sensor plays an important role in the process of creating a digital image (Matasaru, 2014).

The capabilities of CMOS sensors and the new optics have already promoted novel camera architectures that boost the original Bayer RGB design. "*To develop these opportunities requires that we innovate on the third fundamental component of image systems, the image processing pipeline. The pipeline is the set of algorithms, including de-mosaicking, noise reduction, colour management, and display nonlinear transforms (gamma curves), that convert the sensor data into a rendered image*", as shown in Figure 6- 6 (Jiang, Tian, Farrell, & Wandell, 2017) (E.-S. Kim, Jang, Lee, Song, & Sohng, 2006) (Yoon, Kim, Lee, & Lee, 2002).
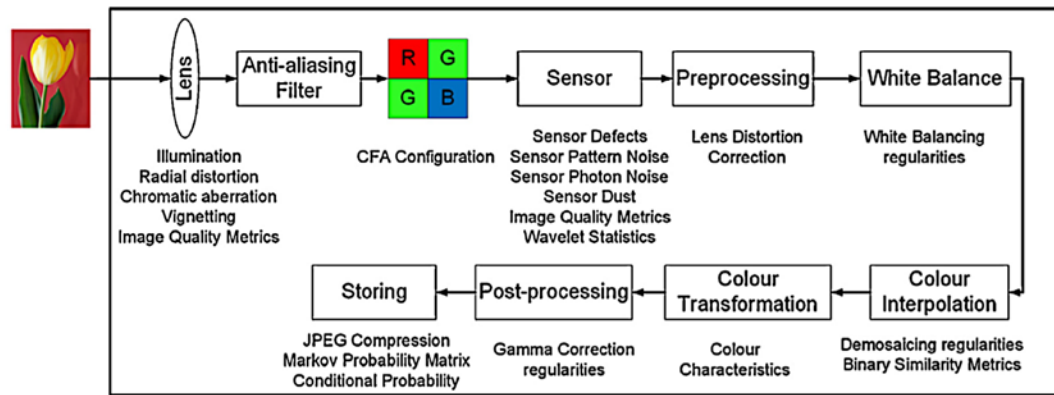
(a) The pipeline structure (Jahanirad, Wahab, & Anuar, 2016)
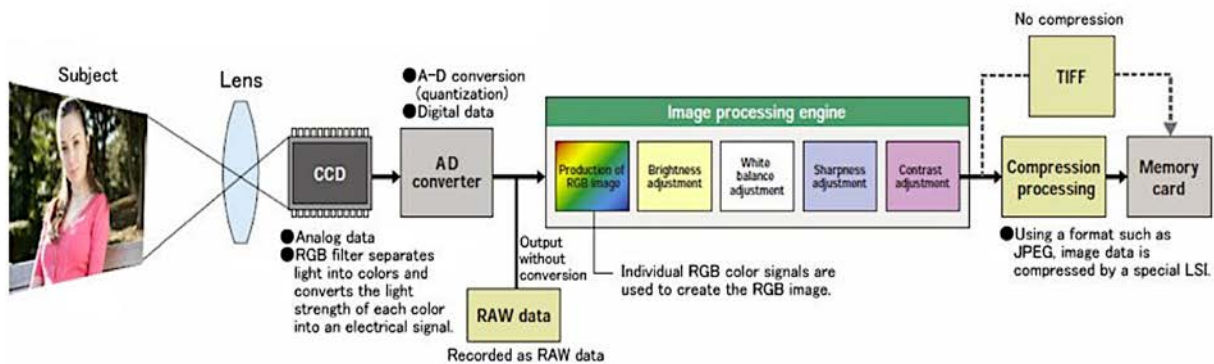
(b) Digital camera signal pipeline(Matasaru, 2014)

Figure 6- 6: Digital camera signal pipeline

The main objective of the image pipeline is to make the image convenient for human perception by transforming the image from raw data to the final compressed image (Huang & Fuh, 2005). The response of image sensors is mostly linear, but the response of the human visual system is nonlinear, so there is a need to compensate the difference between sensors and the human visual system by adjusting the original linear curve to a nonlinear curve. This is known as gamma correction or gamma mapping. However, the human vision response varies. For instance, some people may feel a gamma-corrected image too bright while others may think the image perfectly matches the scene. Sensor manufacturers supply their special gamma lookup tables according to the sensor sensitivity image (Huang & Fuh, 2005). So "*Gamma correction is defined as a mainstream technique to improve image quality. It is used to compensate and correct the errors caused by the non-linear response of modern CMOS image sensors*" (Cao et al., 2014). An important reason that highlights the need for transforming pixel value to a "gamma corrected"

scale is that the human visual system is mostly more sensitive to changes in light intensity at low background illumination than at high background illumination. Most digital imaging devices internally implement "gamma correction" before they save the image data. Consequently, most digital images are already in a gamma corrected scale. Sometimes situations arise where gamma transformation must be considered. For instance, if the gamma, which is significantly related to an image capture device, does not correspond with the gamma of the display device. For instance, most LCD displays use correction tables to imitate the response of a CRT, whose relationship between applied voltage (V) and light intensity (I) is a power relationship, as described by equation (6-5).

$$I = V^{\gamma} \tag{6-5}$$

The exponent value is called the gamma (γ) of the display, and a typical CRT gamma is around 2.5. If we relate equation (6-5) to the pixel values in an 8-bit image, we get the following relationship,

$$y(x) = 255 * (x/255)^{\gamma} \tag{6-6}$$

Where x is the original pixel value, and y is the pixel light intensity produced by the display. This relationship is illustrated in Figure 6- 7 ("Digital Image Processing Laboratory:

Pointwise Operations and Gamma," 2011; University, 2011).
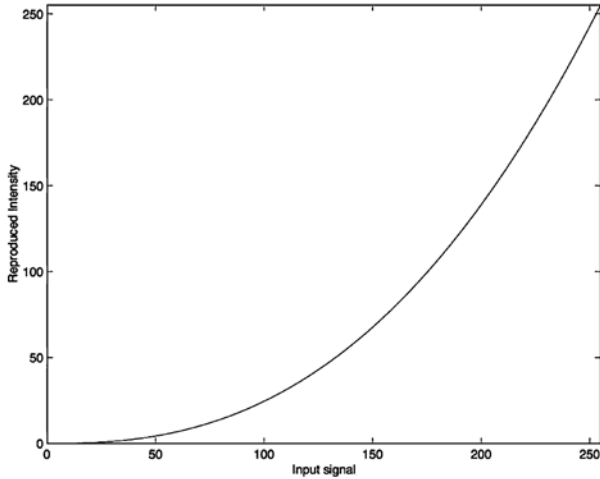
Figure 6- 7: Nonlinear behaviour of a display device having a γ of 2.2 ("Digital Image Processing Laboratory: Pointwise Operations and Gamma," 2011; University, 2011)

Because of the power relationship, linearly- scaled light intensity of the image will appear

mostly too dark on the display, especially for small- and mid-range pixel values. There is a need to compensate for this impact by applying a process called gamma correction. Gamma correction consists of applying the inverse of equation (6-6) on the pixel values, which are raised to the power $1/\gamma$ before display. After gamma correction, pixels with low values become brighter while pixels with high values become darker. Equation 6-7 deals with illumination in a flexible way. Gamma correction is able to lighten shadows and darken highlights automatically (Shi, Yang, & Wu, 2007).

$$y(x) = 255 * (x/255)^{1/\gamma(x)} \tag{6-7}$$

Generally speaking, the standard value of Gamma used to encode RGB image data, whose values are from 0 to 255, equals 2.2. All pixel values are converted to a floating-point value between 0.0 and 1.0. After that, values are raised to the power of 2.2, which are a little bit more than the square values and then converted back to the original range from 0 to 255(ON Semiconductor, 2015).

Smartphone manufacturers often preserve their gamma values as a trade secret and do not share them at all. Consequently, the obstacle is to remove the gamma correction effect when the gamma value is unknown and a technique is needed to choose a proper gamma value, such that it can remove gamma correction from all the images in order to recover the intensity values of the raw images. One of the techniques that can estimate gamma value is called blind inverse gamma correction.

6.6   Blind Inverse Gamma Correction

The value of γ is typically determined experimentally in the absence of any calibration information or knowledge of the imaging device, for example, for an image downloaded from the web. Moreover, most commercial digital cameras dynamically vary the amount of gamma. The blind inverse gamma correction technique is used to estimate the amount of gamma correction in an image. The basic tactic exploits the fact that "*gamma correction introduces specific higher-order correlations in the frequency domain. These correlations can be detected using tools from polyspectral analysis. The amount of gamma correction is then determined by minimizing these correlations*" (Farid, 2001). The method assumes that gamma correction can be modelled with the one-parameter family of functions where $g(u) = u^\gamma$ indicates the image pixel intensity. It is worth mentioning that the scaling of intensities into a new range [0, 1] does not affect the bicoherence. Only the gamma corrected image is given, so the main task is to determine the value of γ. To accomplish this objective, we apply a range of inverse gamma values to the image and

select the value that minimises the third-order correlations as in equation (6-8):

$$\sum_{w1=-\pi}^{\pi} \sum_{w2=-\pi}^{\pi} \left| \hat{b}(w1, w2) \right| \tag{6-8}$$

Where $\hat{b}(w1, w2)$ is the bicoherence, which is defined in equation (6-9).

$$\hat{b}(w1, w2) = \tag{6-9}$$

$$\frac{\left| \frac{1}{N} \sum_k Y_k(w1) Y_k(w2) Y_k^*(w1+w2) \right|}{\sqrt{\frac{1}{N} \sum_k |Y_k(w1) Y_k(w2)|^2 \frac{1}{N} \sum_k |Y_k(w1+w2)|^2}}$$

To avoid the excessive demands on memory and computing resources caused by considering an image's full four-dimensional bicoherence, our analysis is bounded to the one-dimensional horizontal scan lines of an image. One example to get the bicoherence for each 1-D image slice y(n) is computed by dividing the signal, which has one dimension, into overlapping segments each of which has a length 64 with an overlap of 32. A 128-point windowed DFT $Y_k(w)$ is estimated for each segment from which the bicoherence $\hat{b}(w1, w2)$, as in equation (6-9), is estimated. Also, there should be a balance between the segment length and the number of samples from which average is computed. Empirically, the offered parameters have presented a good compromise (Farid, 2001).

Algorithm **4** describes the blind inverse gamma correction process.

Algorithm 4: $BlnGamma(img_{cal}): img_{big}$

Input: img_{cal}: vector of calibrated urinalysis images

Output: img_{big}: vector of images after blind inverse gamma correction

1: $range \leftarrow [0.1: 0.1: 3.8]$ {the potential gamma values}

2: **for** ($\forall \square_\square \in img_{cal}$) **do** {Read image data one by one from the vector of the calibrated

urinalysis images}

3: $\quad I_i^{HSL} \leftarrow RGBtoHSL(I_i^{RGB})$ {Convert image data from RGB to HSL}

4: $\quad I_i^L \leftarrow$ Normalize (I_i^L) {Rescale L band to [0,1]}

5:   **for** $\left(\forall S_j \in \square_\square\right)$ **do**   {Process each Section}

6:     **for** $(\forall \gamma \in range)$ **do**

7:       $bic \leftarrow$ bispec $(S_j^{1/\gamma})$ {Calculate bicoherence}

8:     **end for**

9:     $B(\gamma) \leftarrow$ mean (bic)   {Put the mean of bicoherence in a vector B}

10: **end for**

11: **for** $((\forall k \in vector\,(B))$ **do**

12:     $[val, ind] \leftarrow min\,(B(k))$ {find the value and the index for the minimum value of the

                         bicoherence vector B}

13:     $\overline{\gamma_{est}} \leftarrow range\,[ind]$ {Pick the estimated gamma from the certain range based on the

                     index of the minimum value of the bicoherence vector}

14: **end for**

15:   $\overline{\gamma_{est}} \leftarrow mean\,(\gamma_{est})$

16:   $I_i^L \leftarrow (I_i^L)^{1/\overline{\gamma_{est}}}$ {Apply $\overline{\gamma_{est}}$ as an inverse gamma to I_i^L}

17:   $I_i^{RGB} \leftarrow HSLtoRGB\,(I_i^{HSL})$ {Convert I_i^{HSL} with the new I_i^L into I_i^{RGB}}

18:   $img_{big}[i] \leftarrow I_i^{RGB}$ {Put the image in a vector of images after blind inverse gamma

               correction}

19: **end for**

20: **return** img_{big}

Then transforming image from HSL back to RGB colour mode is conducted through the steps described in Algorithm **5**.

Algorithm   **5:** $HSLtoRGB\,(I^{HSL})$:

I^{RGB}

Input: I^{HSL}: a vector of HSL colour image

Output: I^{RGB}: a vector of RGB colour image

1:   $H \leftarrow I^{HSL}(:,:,1)$

  $S \leftarrow I^{HSL}(:,:,2)$

   $L \leftarrow I^{HSL}(:,:,3)$ {Obtain the Hue, Saturation and Intensity components}

2:      lowLidx $\leftarrow L < (1/2)$

      $q \leftarrow (L * (1+S)) * \text{lowLidx} + (L+S-(L *S)) *(\sim \text{lowLidx})$

      $p \leftarrow 2*L - q$

      hk $\leftarrow H$ {this is already divided by 360}

3:              $t \leftarrow \text{zeros} ([\text{length} (H), 3])$ {1=R, 2=B, 3=G}

      $t (:,1) \leftarrow hk+1/3$

      $t (:,2) \leftarrow hk$

      $t (:,3) \leftarrow hk-1/3;$

4:              underidx $\leftarrow t < 0$

      overidx $\leftarrow t > 1$

      $t \leftarrow t+\text{underidx} - \text{overidx}$

5:                range1 $\leftarrow t < (1/6)$

      range2 $\leftarrow (t >= (1/6) \ \& \ t < (1/2))$

      range3 $\leftarrow (t >= (1/2) \ \& \ t < (2/3))$

      range4 $\leftarrow t >= (2/3)$

6:                P $\leftarrow$ repmat $(p, [1,3])$ {replicate matrices (one per colour) to

make

the final expression simpler}

$$Q \leftarrow \text{repmat} (q, [1,3])$$

rgb_c← (P + ((Q-P) * 6 *t)) * range1 + Q * range2 + (P + ((Q-P) * 6 *(2/3 - t))) * range3 + P * range4

7:     rgb_c ← round (rgb_c*10000)/10000

     rgb ← reshape(rgb_c, size(I^{HSL}))

8:   I^{RGB} : ← rgb

10: **return** I^{RGB}

64

7 Chapter 7: Modelling Correlation between Image Intensity and HSA Concentration

This chapter first presents the theoretical concepts about K-fold cross validation, Principal Component Analysis (PCA) and simple linear regression. To pick the best predictive model, the main function is to pick the best predictive model through machine learning from the obtained data. Basically, both K-fold cross validation and Principal Component Analysis (PCA) are used to obtain eventually the best model where that best model is used to get a simple linear regression with 95% confidence limits for all points on the regression line. An inverse prediction procedure is used to predict HSA concentration values (s) at the value (s) of the Image Intensity. After that, the chapter presents a modelling correlation between image intensity and HSA concentration that can determine the level of CKD based on the grading of concentration. Finally, the chapter presents a urinalysis mobile app that shows the quantified results and the level of CKD.

7.1 Related Work

7.1.1 K- Fold Cross Validation

In statistics or data mining, a standard function is to derive a model that can learn from obtainable data (Refaeilzadeh, Tang, & Liu, 2009). That model could be a regression model or a classifier. One problem of evaluating the model is that while it is able to predict based on the training data, it may not be able to predict future unseen data. So "*cross-validation is a procedure for estimating the generalization performance in this context*"(Refaeilzadeh et al., 2009). The concept of cross-validation was found in the 1930s (Refaeilzadeh et al., 2009), where one sample was used for regression while a second sample was used for prediction. In the 1970s, both Stone and Geisser (Refaeilzadeh et al., 2009) used cross-validation as a means to choose appropriate model parameters, as opposed to using cross-validation purely for estimating model performance. Presently, cross-validation is vastly accepted in both data mining and machine learning communities, and serves as a typical procedure for performance estimation and model selection (Refaeilzadeh et al., 2009).

Stone (1974, 1977) promoted the concept of splitting a dataset and using one part of the data to develop the model and the other part of the data to evaluate the model (Ellis & Mookim, 2013). The two most popular ways are data splitting and K-Fold cross-validation. Also, Tsamardinos, Rakhshani, and Lagani (2014) stated that K-fold cross validation is probably the most popular process to estimate the performance of a learning method for small and medium sample sizes. Despite the popularity of K-fold cross validation, the theoretical properties are not especially recognised outside the machine learning community.

In general, cross-validation is appropriate for supporting scenarios that have low sample sizes, because it is able to reduce over-fitting by splitting the data into two alternately exclusive subsets, each acting as a training set and a validation set (Nematzadeh et al., 2015). The training set is used to estimate a function that is then used to predict output values for the data from the validation set. The predicted values may not match the known values from the validation set. These residual errors are accumulated to calculate the mean squared error (MSE) for the validation set. The function that results in the smallest MSE is regarded as the best-fit function. The dataset is divided into k subsets. Each time, only one of the k data subsets is used as the validation set while the residual k-1 data subsets are jointly used as the training set. Each time, the average MSE of all models is compared so that the model that has the smallest average MSE is selected as the best model (Alpaydin, 2010).

One special case of K-fold cross-validation is called leave-one-out cross-validation (LOOCV) where k equals the number of instances in the data. In other words, in each iteration, nearly all the data is used for training with only a single observation used to test the model. Generally, an accurate estimate obtained using LOOCV is mostly unbiased, but it has high variance, and that leads to unreliable estimates. However, it is still used when the available data is very small, especially in bioinformatics where only dozens of data samples are available (Refaeilzadeh et al., 2009). LOOCV can be defined as "… *an N- fold cross-validation, as it uses only one sample as a test set and the rest of the samples are used as a training set*" (Vasinek, Plato, & Snasel, 2016).

In general, an accurate application of K-fold cross validation conducting multiple splits of samples requires multiple passes through the dataset and consequently can be computationally time consuming especially when the sample size is very large and involves explanatory variables (Ellis & Mookim, 2013).

7.1.2 Principal Component Analysis

Principal component analysis (PCA) is a technique that uses sophisticated underlying mathematical rules to convert a number of correlated variables into a smaller number of variables called principal components (Richardson, 2009). PCA can be defined as a method that produces new uncorrelated variables, called principal components, from the original correlated measured variables (Saad et al., 2015). In addition, PCA is a method of identifying patterns in data, and it involves a mathematical procedure that converts a number of likely correlated variables into a smaller number of uncorrelated variables—the principal components. Principal components are the generation of a new set of variables by PCA, and they have a linear combination of the original variables (Suryanarayana & Mistry, 2016).

Let X represent an (m x n) data matrix, where m denotes number of features and n denotes number of data points:

$$X = \begin{pmatrix} X_{1,1} & \cdots & X_{1,n} \\ \vdots & \ddots & \vdots \\ X_{m,1} & \cdots & X_{m,n} \end{pmatrix} = (X_1 \quad X_2 \quad X_3 \quad \cdots \quad X_n) \tag{7-1}$$

We define the overall mean of X as:

$$\mu = \begin{pmatrix} \bar{x}_1 \\ \vdots \\ \bar{x}_m \end{pmatrix} = \begin{pmatrix} \dfrac{1}{n}\displaystyle\sum_{i=1}^{n} x_{1i} \\ \vdots \\ \dfrac{1}{n}\displaystyle\sum_{i=1}^{n} x_{mi} \end{pmatrix} \tag{7-2}$$

The deviation from the mean can be written as:

$$\phi = (\phi_1 \quad \cdots \quad \cdots \quad \phi_n) \tag{7-3}$$

Where $\phi_i = X_i - \mu$ and i = 1,2...n.

The covariance scales the degree of the linear relationship between two variables. While a large positive value indicates positively correlated data, a large negative value indicates negatively correlated data. The covariance matrix is given as:

$$V = \frac{1}{n}\,\phi\phi^t \tag{7-4}$$

Where ϕ^t is the transpose of ϕ.

By applying Singular Value Decomposition to the covariance matrix, we obtain the eigenvalues $(\lambda_1, \lambda_2, \dots \lambda_m)$ and the eigenvectors $(u_1, u_2, \dots u_m)$.

We choose the p eigenvectors corresponding to the most representative eigenvalues $(\lambda_1 < \lambda_2 < \cdots < \lambda_p)$ such as p<m. The principal components matrix is constituted from the eigenvectors $W_{m,p} = (u_1, \dots, \dots u_p)$. By projecting the original data into the new subspace spanned by principal components, we obtain the following representation:

$$Y_{p,n} = W^t \phi \tag{7-5}$$

"*To classify a new test sample into normal or abnormal data, the first step is to project the test data matrix into new dimensions with principal components. The second step is to use the K-Nearest-Neighbours (KNN) algorithm to compute Euclidean distance between all vectors of projected training data and all vectors of projected testing data, and assign them to the class for which we have the smallest Euclidean distance*" (Saad et al., 2015).

7.1.3 The Method of Least Squares

"*For most quantitative experiments, the method of least squares is the best analytical technique for extracting information from a set of data*" (Wolberg, 2006). The method is implemented first in the simplest case of a straight-line fitting.

$$y = a + bx. \tag{7-6}$$

Accordingly, a and b are chosen so as to minimise the sum of squares:

$$SS = \sum_{i=1}^{n} \epsilon_i^2 = \sum_{i=1}^{n} (y_i - a - bx_i)^2 \tag{7-7}$$

Taking $\partial SS / \partial a = 0$ and $\partial SS / \partial b = 0$ gives:

$$\frac{\partial SS}{\partial a} = -2 \sum_{i=1}^{n} e_i = -2 \sum_{i=1}^{n} (y_i - a - bx_i), \tag{7-8}$$

$$\frac{\partial SS}{\partial b} = -2 \sum_{i=1}^{n} x_i e_i = -2 \sum_{i=1}^{n} x_i (y_i - a - bx_i).$$

To find the minimum, we equate both of these equations to zero:

$$\sum_{i=1}^{n} (y_i - a - bx_i) = 0 \ and \ \sum_{i=1}^{n} x_i (y_i - a - bx_i) = 0 \ . \tag{7-9}$$

Two simultaneous linear equations are obtained, in the two unknowns a and b, called the normal equations. Using the 'bar' marking

$$\bar{x} = \frac{1}{n} \sum_{i=1}^{n} x_i, \tag{7-10}$$

both sides are divided by n and rearranged to reveal the normal equations:

$$a + b\bar{x} = \bar{y} \quad and \quad a\bar{x} + b\overline{x^2} = \overline{xy}. \qquad (7\text{-}11)$$

Multiplying the first by x and subtracting from the second:

$$b = \frac{\overline{xy} - \bar{x}.\bar{y}}{\overline{x^2} - (\bar{x})^2}, \qquad (7\text{-}12)$$

And then

$$a = \bar{y} - b\bar{x}.$$

This bar notation will be used throughout this thesis. It refers to the sample mean, or average, of x1, ..., xn, and similarly for y. The sample variance is defined as the average, written s_x^2 or s_{xx}. Then using linearity of average, or 'bar',

$$s_x^2 = s_{xx} = \overline{(x - \bar{x})^2} = \overline{x^2 - 2x.\bar{x} + \bar{x}^2} = \overline{(x^2)} - 2\bar{x}.\bar{x} + (\bar{x})^2 = \overline{(x^2)} - (\bar{x})^2, \qquad (7\text{-}13)$$

Since $\overline{x.\bar{x}} = (\bar{x})^2$. Similarly the sample covariance of x and y is defined as the average of $(x - \bar{x})(y - \bar{y})$, written $as\ s_{xy}$. So:

$$s_{xy} = \overline{(x - \bar{x})(y - \bar{y})} = \overline{xy - x.\bar{y} - \bar{x}.y + \bar{x}.\bar{y}} \qquad (7\text{-}14)$$

$$= \overline{(xy)} - \bar{x}.\bar{y} - \bar{x}.\bar{y} + \bar{x}.\bar{y} = \overline{(xy)} - \bar{x}.\bar{y}.$$

Therefore, the slope b is given by the sample correlation coefficient

$$b = s_{xy}/s_{xx}, \qquad (7\text{-}15)$$

the ratio of the sample covariance to the sample x-variance. Using the alternating 'sum of squares' marking, we get:

$$S_{xx} = \sum_{i-1}^{n}(x_i - \bar{x})^2, \quad S_{xy} = \sum_{i-1}^{n}(x_i - \bar{x})(y_i - \bar{y}), \qquad (7\text{-}16)$$

$$b = S_{xy}/S_{xx}, \quad a = \bar{y} - b\bar{x}.$$

The least-squares line that we have fitted is: $y = a + bx$ with this a and b, or

$$S_{xx} = \sum_{i-1}^{n}(x_i - \bar{x})^2, \quad S_{xy} = \sum_{i-1}^{n}(x_i - \bar{x})(y_i - \bar{y}), \tag{7-17}$$

$$y - \bar{y} = b(x - \bar{x}), \qquad b = s_{xy}/s_{xx} = S_{xy}/S_{xx}.$$

This line is called the sample regression line. It is worth mentioning that the line goes through the point $(\bar{x}, \bar{y})$—the centroid, or centre of mass, of the scatter diagram $(x_1, y_1), \ldots, (x_n, y_n)$ (Bingham & Fry, 2010).

### 7.1.4   The simple Linear Regression Equation

The simple linear regression is defined as "*the simplest functional relationship of one variable to another in a population*". Equation (7-18) is the general equation for a straight line

$$Y_i = \alpha + \beta X_i, \tag{7-18}$$

where $\alpha \; and \; \beta$ are population parameters. However, it is unlikely for data to be precisely in a straight line. Therefore, Y might be related to X by equation (7-19):

$$Y_i = \alpha + \beta X_i + \epsilon_i, \tag{7-19}$$

where ϵ_i is an "error" or "residual" that is a divergence of a real y value from what Equation (7-18) predicts y to be, and it is worth mentioning that the sum of the ϵ_i equals zero. For example, data is collected representing bird characteristics, with the length of a bird's wing as the dependent variable and bird age as the independent variable. Figure 7- 1 shows a scatter of data representing sample measurements of a community consisting of 13 birds where wing length is linearly related to age, as listed in Table 7- 1 (Zar, 2010). Therefore, the question is to estimate the values α and β that characterise the functional relationship in that population.
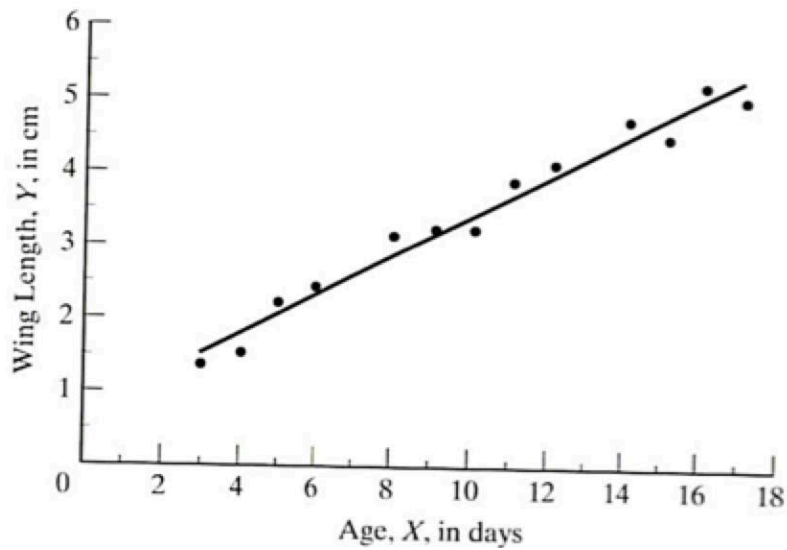
Figure 7- 1: Bird wing length as a function of age (Zar, 2010)

It is unusual, or an exceptional situation, if all data in the scatter diagram exists on a straight line. In Figure 7- 1, it is noticeable that there is significant variability in the data around any straight line that can be drawn through the data. What we are trying to find is commonly named the "best-fit" line through the data. The "best-fit" criterion mostly uses the concept of least squares. Figure 7- 2 is an enlarged part of Figure 7- 1, where it can be noted that each value of X has a corresponding value of Y occurring on the line that we may sketch through the scattered data points.

Table 7- 1: Wing Length of 13 Sparrows of Various Ages (Zar, 2010)

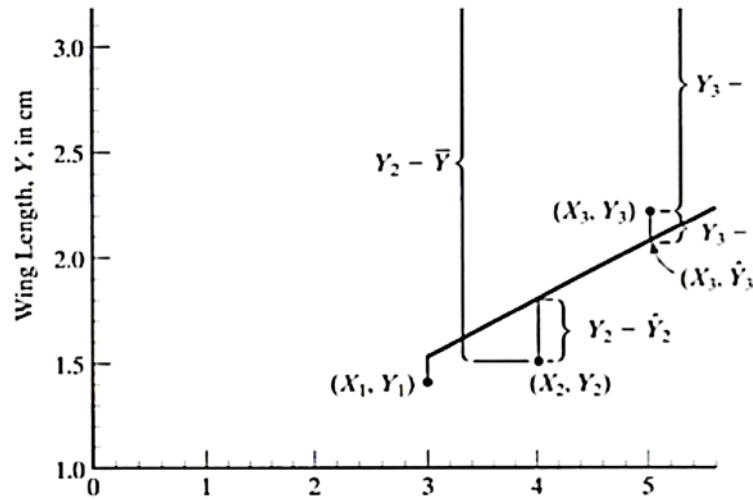| No.	Age (days) (X)	Wing length (cm) (Y)
1	3.0	1.4
2	4.0	1.5
3	5.0	2.2
4	6.0	2.4
5	8.0	3.1
6	9.0	3.2
7	10.0	3.2
8	11.0	3.9
9	12.0	4.1
10	14.0	4.7
11	15.0	4.5
12	16.0	5.2
13	17.0	5.0
N = 13		

Figure 7- 2: An enlarged portion of Figure 7- 1, showing the portioning of Y deviations (Zar, 2010)

The linearly predicted value of Y can be represented as $\hat{Y}$ to distinguish it from the original Y value. An observed data point is denoted (X_i, Y_i) while a point on the regression line is denoted as $(X_i, \hat{Y}_i)$. The norm of the least square takes into account the vertical deviation of each point from the line, i.e., the deviation can be described as $Y_i - \hat{Y}_i$. The best-fit line is obtained when the total deviation across all samples is minimized. Thus, $\sum_{i=1}^{n}(Y_i - \hat{Y}_i)^2$ is to be a minimum, where n is the number of data points that comprise the sample. The sum of squares of these deviations is called the residual sum of squares or the error sum of squares. Because of the fact that the only method to locate the population parameters α and β is to possess the whole population data, this is nearly impossible. Therefore, there is a need to estimate these parameters from a sample of n pairs of X and Y values. Calculations are required to obtain such estimates and to carry out the testing of a diversity of significant hypotheses, including the calculation of the sums of squared deviations from the mean. We have to remember that the "sum of squares" of X_i values is defined as $\sum(X_i - \bar{X})^2$ that is obtained readily on a calculator as $\sum X_i^2 - (\sum X_i)^2/n$. It will be appropriate to define $x_i = X_i - \bar{X}$, so the sum of squares can be shortened to $\sum x_i^2$ or merely as $\sum x^2$. Another necessary quantity for regression analysis is the sum of the cross products of deviations from the mean:

$$\sum xy = \sum (X_i - \bar{\bar{X}})(Y_i - \bar{Y}). \tag{7-20}$$

"*Where y denotes a deviation of a Y value from the mean of all Y's just as x denotes a deviation of*

72

an X value from the mean of all X's. The sum of the cross products, analogously to the sum of squares, has a simple-to-use "machine formula" (Zar, 2010):

$$\sum xy = \sum X_i Y_i - \frac{(\sum X_i)(\sum Y_i)}{n} . \tag{7-21}$$

It is recommended formula (7-21) be used when the calculation is not performed by a computer.

7.1.4.1 The regression Coefficient

In formula ((7-19) parameter β is called the regression coefficient, or the slope of the best-fit regression line. The best sample estimate of β is:

$$b = \frac{\sum xy}{\sum x^2} = \frac{\sum(X_i - \bar{X})(Y_i - \bar{Y})}{\sum(X_i - \bar{X})^2} = \frac{\sum X_i Y_i - \frac{(\sum X_i)(\sum Y_i)}{n}}{\sum X_i^2 - \frac{(\sum X_i)^2}{n}} . \tag{7-22}$$

Despite the fact that the denominator in this computation is always positive, the numerator might be positive, negative, or zero, and theoretically the value of b can extend from $-\infty$ to $+\infty$, including zero, as shown in Figure 7- 3.
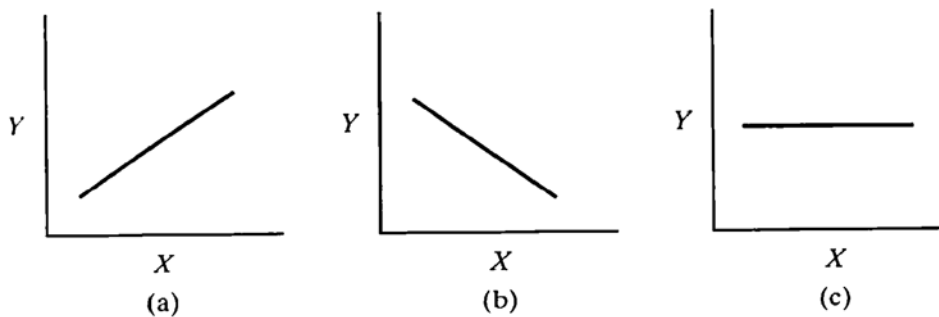

Figure 7- 3: The slope of a linear regression line may be (a) positive, (b) negative, or (c) Zero (Zar, 2010)

7.1.4.2 The Y Intercept

There are an infinite number of parallel lines possessing the same slope, as shown in Figure 7- 4. However, each line can be defined by stating, in addition to β, any one point on the line, i.e., any pair of coordinates $(X_i, \hat{Y}_i)$. It is typical to choose the point on the line where X = 0. The value of Y in the population of this point is the parameter α, which is called the Y intercept. Mathematically, the point $(\bar{X}, \bar{Y})$ lies on the best-fit regression line. Therefore, substituting $\bar{X}$ and Y in Equation (7-18) we find that:

$$\bar{Y} = \alpha + \beta\bar{X} \tag{7-23}$$

73

and

$$\alpha = \bar{Y} + \beta\bar{X}. \qquad (7\text{-}24)$$

The best estimate of the population parameter α is the sample statistic:

$$a = \bar{Y} + b\bar{X}. \qquad (7\text{-}25)$$

The sample regression equation that estimates the relationship between Y and X, which is stated in Equation (7-18), can be rewritten as:

$$\hat{Y}_i = a + bX_i, \qquad (7\text{-}26)$$

or equivalently

$$\hat{Y}_i = \bar{Y} + b(X_i - \bar{X}). \qquad (7\text{-}27)$$

Figure 7- 4 and Figure 7- 5 clearly show that the knowing either a or b provides an incomplete description of a regression function while knowing or specifying both a and b allows a line to be uniquely defined. "*Also, because a and b were calculated using the criterion of least squares, the residual sum of squares from this line is smaller than the residual sum of squares that would result from any other line, i.e., a line with any other a or b that could be drawn through the data points. This regression line, i.e., the line with this a and b is not the same line that would result if Y where the independent variable and X the dependent variable*" (Zar, 2010).
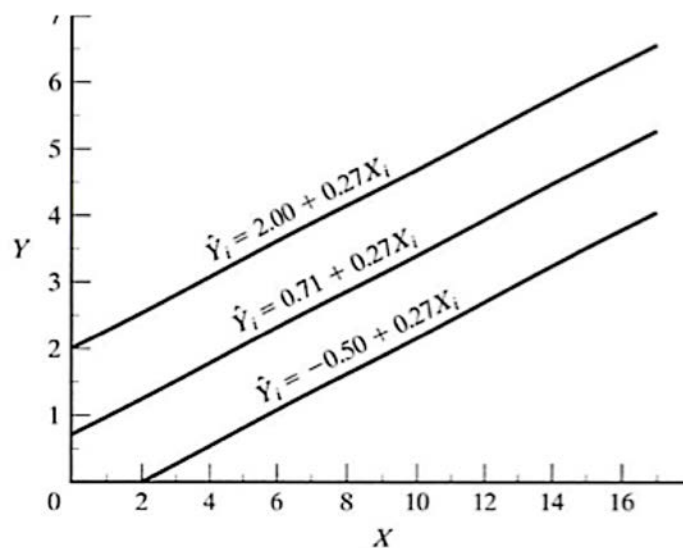

Figure 7- 4: For any given slope, there exist an infinite number of possible regression lines, each with a different

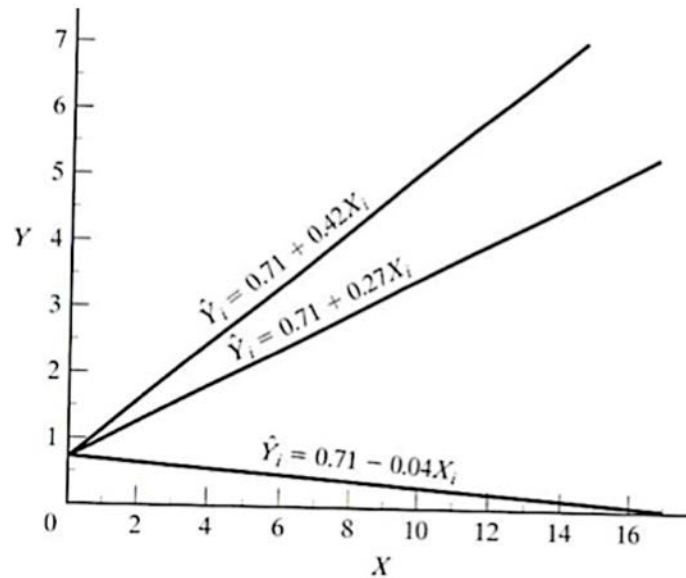Y intercept. Three lines are shown here (Zar, 2010).

Figure 7- 5: For any given Y intercept, there exist an infinite number of possible regression lines, each with a different slope. Three lines are shown here (Zar, 2010).

7.1.4.3 Confidence Intervals in Regression

Generally speaking, the standard error of a statistic allows us to calculate a confidence interval for the parameter that has been estimated as:

$$confidence\ interval\ =\ statistic\ \mp\ (t)(SE\ of\ statistic). \qquad (7\text{-}28)$$

For the $(1 - \alpha)$ confidence limits of β,

$$b \mp t_{\alpha(2),(n-2)}s_b. \qquad (7\text{-}29)$$

Therefore,

$$L_1 = b - t_{\alpha(2),(n-2)}s_b \qquad (7\text{-}30)$$

and

$$L_2 = b + t_{\alpha(2),(n-2)}s_b. \qquad (7\text{-}31)$$

It is worth mentioning that 95% confidence means that there is no greater than a 5% chance that we are wrong. As Figure 7- 6 shows, the dashed lines represent the confidence limits of the regression line slope, and within these limits, the various possible values of b rotate the line about the point.

75
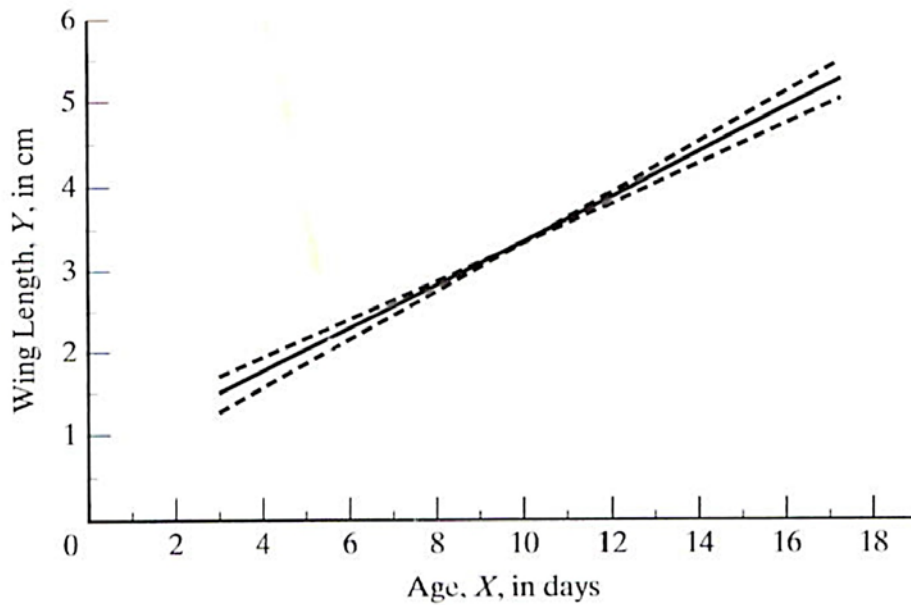
Figure 7- 6: The regression line from, showing by dashed lines, the lines with slopes equal to the upper and lower 95% confidence limits for β(Zar, 2010).

As mentioned before, a regression equation allows estimating the value of Y at a given value of X in the population, and the standard error of such a population estimate is

$$S_{\hat{Y}_i} = \sqrt{s_Y^2 \cdot X \left[\frac{1}{n} + \frac{(X_i - \bar{X})^2}{\sum x^2} \right]}.$$

(7-32)

Note that, if the confidence limits were calculated for all points on the regression line, the result would be the curved confidence bands shown in Figure 7- 7.
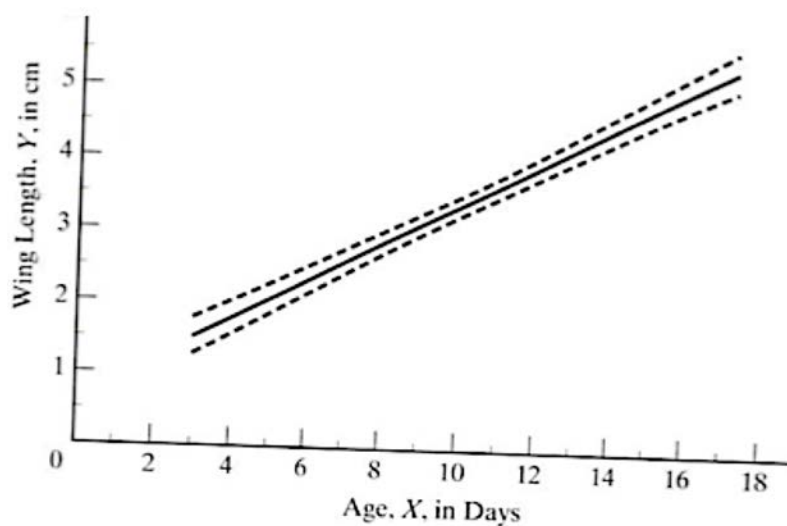
Figure 7- 7: The 95% confidence bands (dashed lines) for the regression line from Figure 7- 1 (the regression of the previous example) (Zar, 2010).

76

7.1.4.4 Inverse Prediction

Occasionally there is a need to predict the independent variable (X_i) at the value of the dependent variable (Y_i) in the population. Therefore, a procedure is followed that is called an inverse prediction. In the previous example we may ask, "*How old is a bird that has a wing 4.5 cm long?*" This can be achieved by rearranging the linear regression relationship of equation 7-26:

$$\widehat{X_\iota} = \frac{Y_i - a}{b}. \tag{7-33}$$

From Figure 7- 7, it is obvious that confidence limits calculated around the predicted $\widehat{Y_\iota}$ are symmetric above and below $\widehat{Y_\iota}$ while confidence limits related to the predicted $\widehat{X_\iota}$ are not symmetric to the left and to the right of $\widehat{X_\iota}$. The $1 - \alpha$ confidence limits for the X predicted at a given Y can be calculated as follows:

$$\bar{X} + \frac{b(Y_i - \bar{Y})}{K} \mp \frac{t}{K} \sqrt{s_Y^2 . x \left[\frac{(Y_i - \bar{Y})^2}{\sum x^2} + K \left(1 + \frac{1}{n} \right) \right]}, \tag{7-34}$$

where $K = b^2 - t^2 s_b^2$. This computation is a special situation of the prediction of the $\widehat{X}$ that is associated with numerous values of Y at that X. For the study of the previous example, age can be predicted for m birds taken from the population and having a mean body weight of $\bar{Y_i}$ (Zar, 2010):

$$\widehat{X_\iota} = \frac{\bar{Y_\iota} - a}{b}. \tag{7-35}$$

7.2   Modelling the Correlation

As detailed in Chapter 5 (Data Collection), many samples were made with various HSA concentration values and different units. The final experiment included images of all five levels of CKD starting from trace and ending with the 4+ level. The unit used to prepare the concentration was µM/L. The materials used were BSPOTPE bioprobes for urine specimens with HSA concentration levels in the range 0–1000 mg/dL. Samsung Galaxy N3, Galaxy Note 4 and Samsung S3 phones were used to capture these images. Figure 7- 8 shows the urinalysis images captured by the three smartphones.

Samsung Galaxy N3

Samsung S3

Samsung Galaxy Note 4
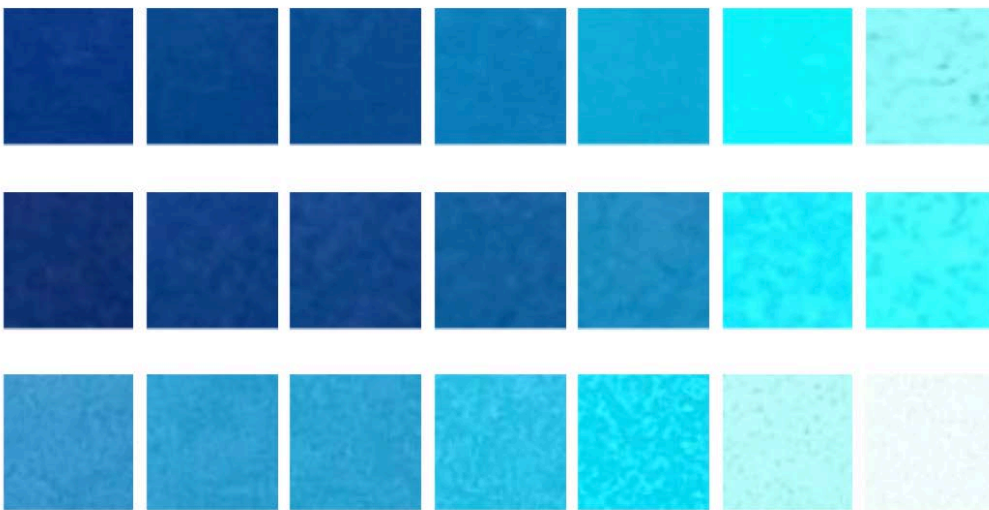
Figure 7- 8: Sample images of different HSA concentration levels taken by three smartphones

More details on the data, for example, how many photos in total for each phone, a table listing all the samples (concentration, intensity)

Figure 7- 9 shows three irregular, non-linear relationships, each representing the image colour intensity value (μM/L) versus the HSA concentration value captured by one of the three smartphones.

These irregular relationships are made regular by first identifying a best fit function for each dataset. Most relationships behave as either logarithmic or power functions. For instance, the intensity values extracted from the images captured by the Samsung S3 phone have a best fit with a logarithmic function, rather than a power function, as determined by the root-square (R^2) error (as shown in Figure 7- 10 and Figure 7- 11). Table 7- 2 summarises the identification of best fit for each smartphone with a logarithmic or power function. The S3 results match best with a logarithmic function, as described above. In contrast, the N3 and N4 results best match with power functions.

Mobiles' Intensity Data

The Concentration Values (µM/L)

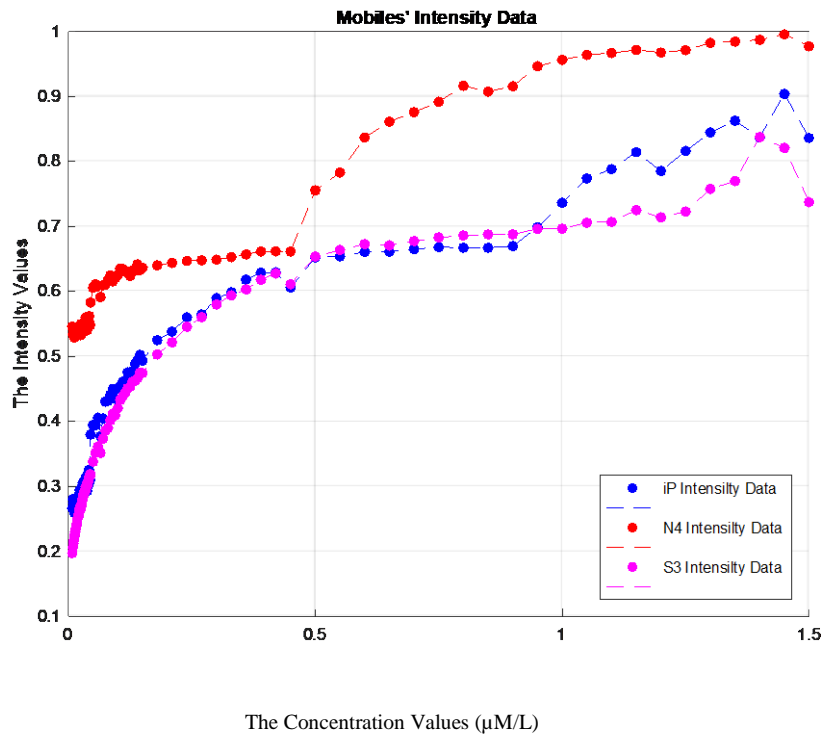**Figure 7- 9: Image intensity values versus HSA concentration (µM/L) for Samsung Galaxy N3, Samsung Galaxy N4 and Samsung S3 mobiles.**

Mobiles' Data and The Logarithmic Function.

The Concentration Values (µM/L)
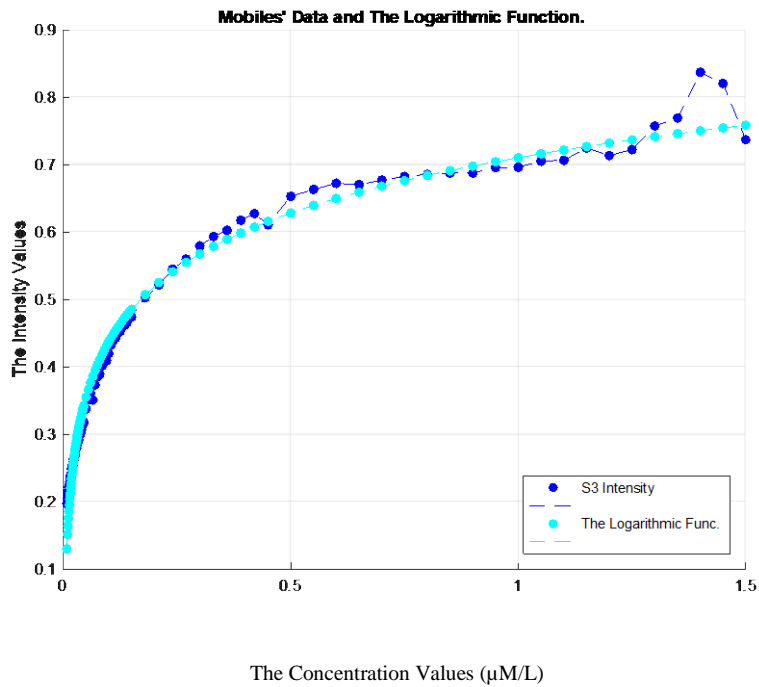
Figure 7- 10: The logarithmic fit function for S3.

79
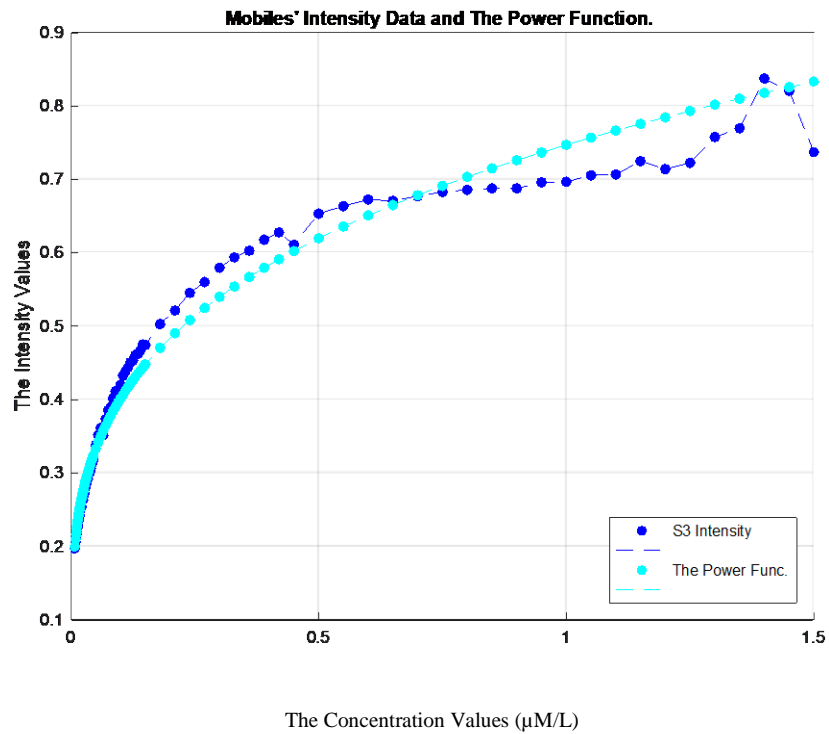
Figure 7- 11: The Power fit function for S3.

Table 7- 2: The best-fit function for each smartphone based on R^2

Mobile Name	General Model: y = a + b*log(x) Coefficients (with 95% confidence bounds):	R^2	General Model: y = a*x^ b Coefficients (with 95% confidence bounds):	R^2	The best fit function
Samsung S3	a = 0.7108 (0.7024, 0.7193) b = 0.1186 (0.1155, 0.1217)	**0.985136**	a = 0.7471 b = 0.2695	0.978745	Logarithm function 99%
Samsung Galaxy N3	a =0.738 (0.7235, 0.7525) b =0.1192 (0.1139, 0.1245)	0.958023	a = 0.762486 b = 0.249242	**0.97880**	Power function 98%
Samsung Galaxy N4	a = 0.8717 (0.8488, 0.8946)	0.844299	a = 0.867252 b = 0.128359	**0.88532**	Power function 89%

	b=0.09178 (0.08343, 0.1001)				

Figure 7- 12 displays the best fit functions for each of the three relations generated by the smartphones. The relationships generated by the smartphones are enhanced using these best fit functions by having each image intensity value be enhanced by the corresponding value in the best fit curve. The reason for this step is preparation for the calibration stage.

An enhancement process for any of relationships is conducted through the steps described in Algorithm 6.

Algorithm 6: Int_Enh (*MeanValue$_L$*): *MeanValue$_{Enh}$*

Input: *MeanValue$_L$*: a vector of the mean intensity values (L band of HSL colour space)

Input: x {Concentration values}

Output: *MeanValue$_{Enh}$*: a vector of the mean intensity values (L band of HSL colour space) after the enhancement.

1: $Intensity \leftarrow MeanValue_L$

2:    $[a, b] \leftarrow Trans2Log(x, Intensity)\{$ to extract the coefficients of log fun.$\}$

3:    $y_{log} \leftarrow b + a * log(x)$

4:    $rsq_{log} \leftarrow rsqFun(x, Intensity, y_{log})$

5:    $[coeff1, coeff2] \leftarrow Trans2Power(x, Intensity)$ { to extract the coeff. of power

fun.$\}$

6:   $y_{Power} \leftarrow coeff1 * x^{\wedge}coeff2$

7:   $rsq_{Power} \leftarrow rsqFun(x, Intensity, y_{Power})$

8:      **if** $rsq_{log} > rsq_{Power}$

$BestFitFun \leftarrow y_{log}$

$rsq \leftarrow rsq_{log}$

else

$$BestFitFun \leftarrow y_{Power}$$

$$rsq \leftarrow rsq_{Power}$$

    end if

      9:        $MeanValue_{Enh} \leftarrow BestFitFun$

10: **return** $MeanValue_{Enh}$

A logarithmic fit function is conducted through the steps described in Function 1.

Function 1: $Trans2Log(x, y): [a, b]$

Input: y: a vector of the mean intensity values (L band of HSL colour space)

Input: x:{Concentration values}

Output: a, b: parameters

1: *myfit ← fittype('a + b*log(x)',...'dependent',{'y'},'independent',{'x'},...'coefficients',{'a','b'})*

2:     *fit(x',y',myfit)*

3:    $p \leftarrow polyfit\,(log(x), y, 1)$

4:    $a \leftarrow p\,(1)$

      $b \leftarrow p\,(2)$

6: $f \leftarrow fit(x, y, 'a + b * log(x)')$

10: **return** a, b

A power fit function is conducted through the steps described in Function 2.

Function 2: $Trans2Power(x, y): [a, b]$

Input: y: a vector of the mean intensity values (L band of HSL colour space)

Input: x:{Concentration values}

Output: a, b: parameters

1: $f \leftarrow fit(x, y,' power1')$

2: $p \leftarrow polyfit(\log(x), \log(y), 1)$

3: $a \leftarrow p(1)$

   $b \leftarrow p(2)$

4: $f \leftarrow fit(x, y,' b * x^{a'})$

10: **return** a, b

Compute $R^2$is conducted through the steps described in Function 3.

Function 3: $rsqFun\ (x, y, yfit): rsq$

Input: y: a vector of the mean intensity values (L band of HSL colour space)

Input: x:{Concentration values}

Input: *yfit:* the function of y $[y_{log}/y_{Power}]$

Output: a, b: parameters

1: $yresid \leftarrow y - yfit$ {Compute the residual values as a vector of signed numbers}

2: $SSresid \leftarrow \sum yresid^2$ {Square the residuals and total them to obtain the residual

   sum of squares}

3: $SStotal \leftarrow (length(y) - 1) * var\ (y)$ {Compute the total sum of squares of y by

   multiplying the variance of y by the number

   of observations minus 1}

4: $rsq \leftarrow 1 - SSresid/SStotal$ {Compute R^2}

5: return rsq

The Concentration Values (µM/L)
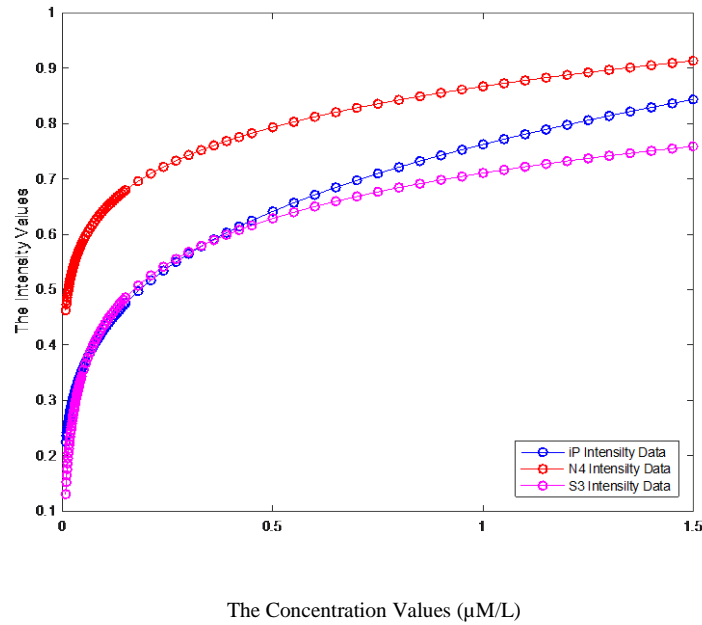
Figure 7- 12: The best fit functions for the three relationships.

Figure 7- 13 shows the relationships between HSA concentration levels and the intensity values of the images after the enhancement. Figure 7- 14 shows the relationships between HSA concentration levels and the intensity values of the calibrated images. All the curve fittings in Figure 7- 13 and Figure 7- 14 reveal a power or logarithmic correlation. While the curves for the original images show considerable discrepancy, those for the calibrated images display reasonably consistent results as listed in Table 7- 3. The N4's curve is slightly better than the other two and is subsequently chosen to proceed with blind inverse gamma correction, as listed in Table 7- 4. The results have confirmed that the calibration process is able to tackle the diversity of smartphone cameras.

The Concentration Values (μM/L)
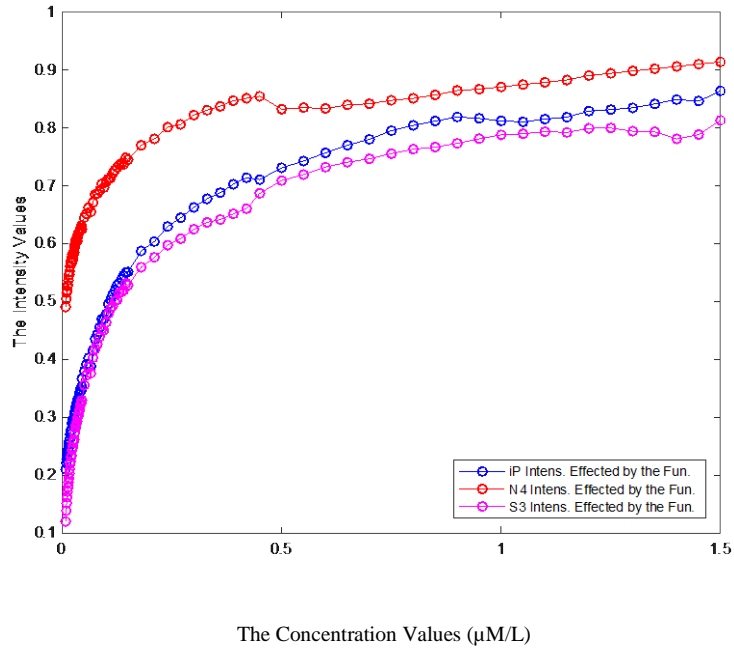
Figure 7- 13: Concentration vs. intensity of images after the enhancement

The Concentration Values (μM/L)
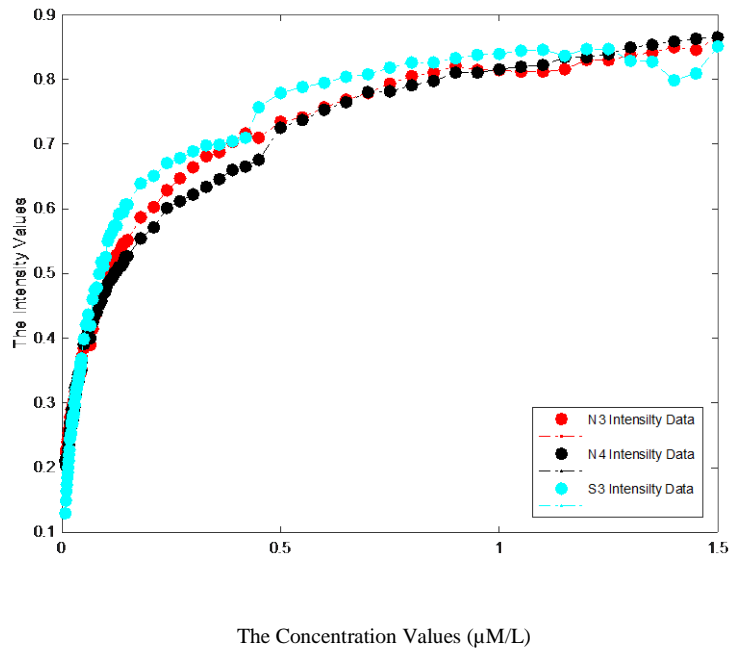
Figure 7- 14: Concentration vs. intensity of calibrated images

Table 7- 3: The general model and R2 for the three relationships after enhancement

Mobile Name	General Model: f(x) = a+b*log(x) Coefficients (with 95% confidence bounds):	R^2	General Model: f(x) = a*x^b Coefficients (with 95% confidence bounds):	R^2	The best fit function
Samsung S3	a =0.8446 (0.8337, 0.8555) b = 0.1487(0.1447, 0.1526) SSE: 0.07428 R-square: 0.9843 Adjusted R-square: 0.9841 RMSE: 0.02905	**0.9841**	a = 0.8525 (0.8275, 0.8774) b = 0.2618 (0.2452, 0.2785) SSE: 0.3303 R-square: 0.9303 Adjusted R-square: 0.9295 RMSE: 0.06126	0.9303	Logarithm function 98%
Samsung Galaxy N3	a = 0.8106 (0.8026, 0.8185) b =0.1374 (0.1345, 0.1403) SSE: 0.03956 R-square: 0.9902 Adjusted R-square: 0.9901 RMSE: 0.0212	**0.9902**	a = 0.8289 (0.8154, 0.8423) b = 0.2572 (0.2481, 0.2664) SSE: 0.09613 R-square: 0.9761 Adjusted R-square: 0.9758 RMSE: 0.03305	0.9761	Logarithm function 99%
Samsung Galaxy N4	a =0.8029 (0.7963, 0.8095) b =0.138 (0.1355, 0.1404) SSE: 0.02753	**0.9932**	a = 0.8238 (0.8133, 0.8342) b = 0.2648 (0.2575, 0.272)	0.9856	Logarithm function 99%

	R-square: 0.9932 Adjusted R-square: 0.9931 RMSE: 0.01769		SSE: 0.05816 R-square: 0.9856 Adjusted R-square: 0.9855 RMSE: 0.02571		

Table 7- 4: Curve fittings for the 3 smartphones

Phone	RMSE	Variance	St. Dev.	$R^2 (y = a + b * log(x))$
Galaxy N3	0.02120	0.0452	0.2126	0.9902
Galaxy N4	0.01769	0.0454	0.2132	0.9932
Samsung S3	0.02905	0.0532	0.2308	0.9841

After performing blind inverse gamma correction on the calibrated images from Galaxy N4, Figure 7- 15 (a) shows how image intensity responds to HSA concentration.

The Concentration Values (μM/L)
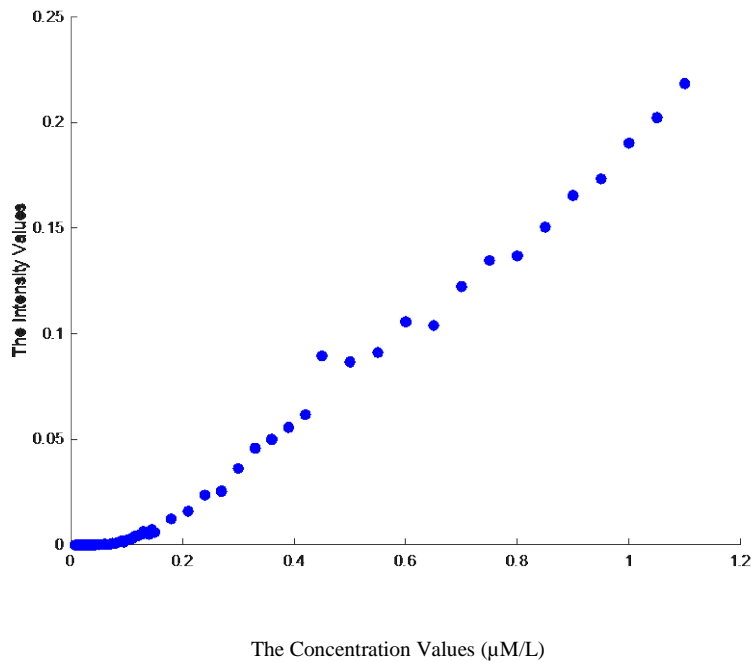
(a) Concentration vs. intensity of blind inverse gamma corrected images of N4

Recovered Original Data using one eignvalue (Reduced dimension)

The Concentration Values (μM/L)

(b) Principle component analysis (PCA)

The Concentration Values (μM/L)
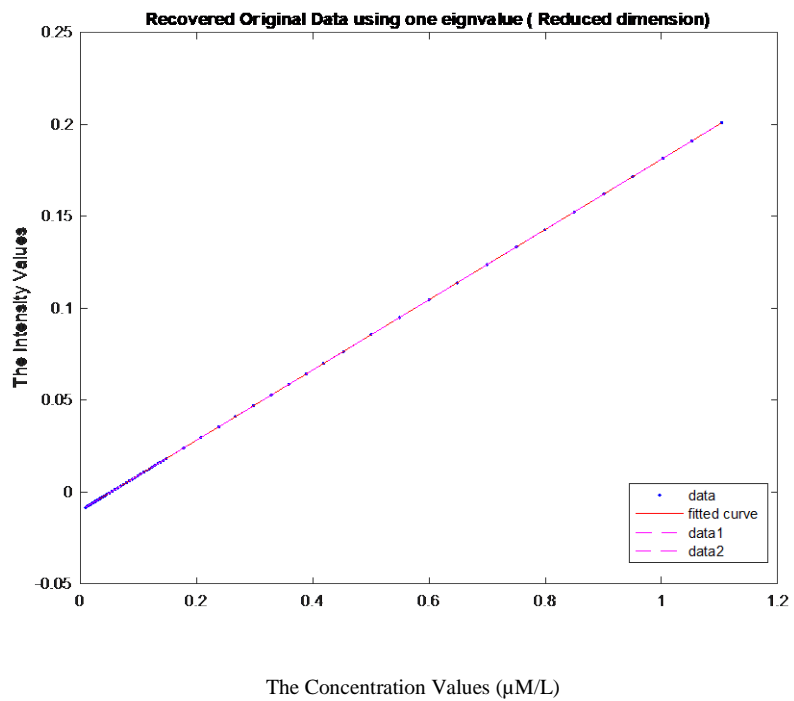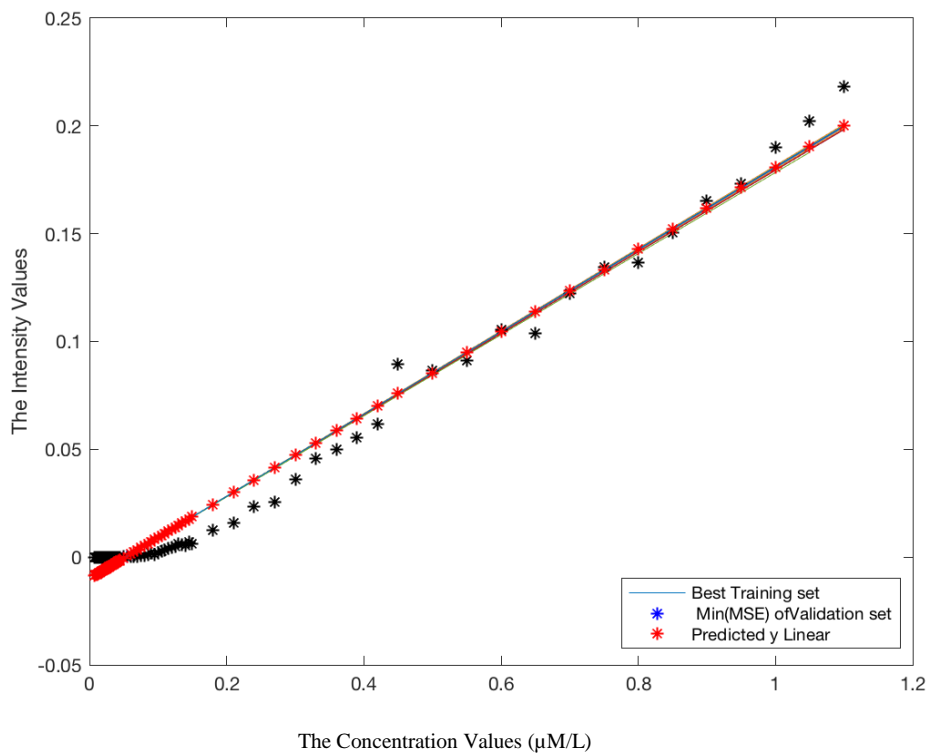
(c) K-fold cross-validation
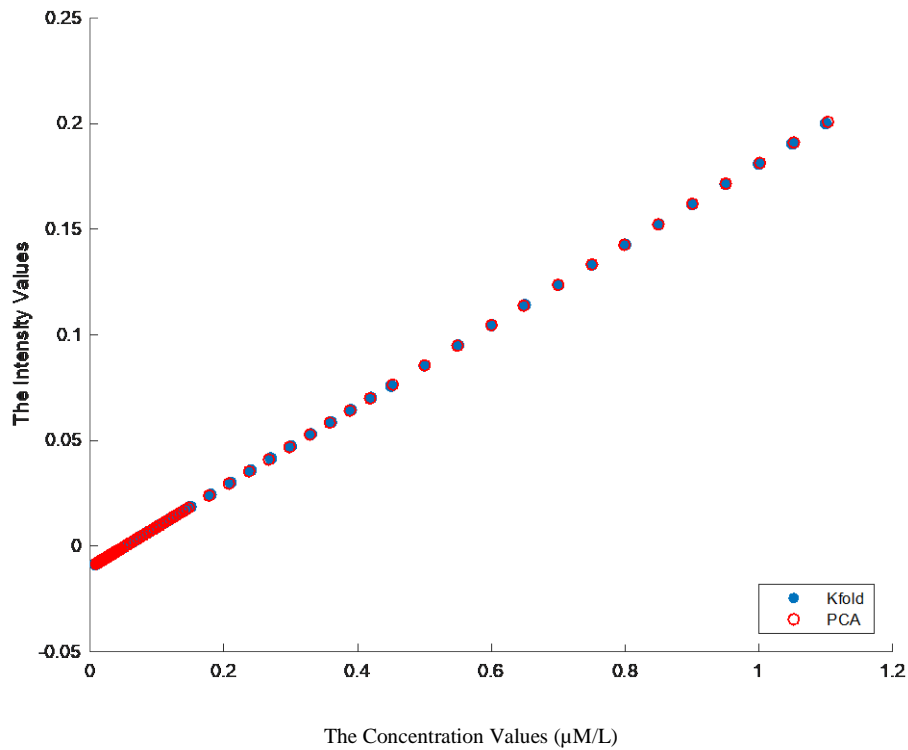
(d) PCA vs. K-fold

Figure 7- 15: Relationship between HSA concentration levels and intensity values after blind inverse gamma correction

Figure 7- 15(b) depicts a linear relationship between the HSA concentration levels and the intensity values of the blind inverse gamma corrected images after performing Principle Component Analysis (PCA). To verify this linear relationship, we also use K-fold cross validation to model the correlation, which again exhibits a linear relationship as shown in Figure 7- 15(c). Figure 7- 15(d) reveals that the regression models derived independently with the two different techniques are almost identical. Table 7- 5 lists some random data points predicted by the two regression models. The results confirm that the blind inverse gamma correction process is able to mitigate the nonlinear correspondence between the image intensity values and the HSA concentration levels.

Table 7- 5: Random data predicted by PCA and K-fold models

No.	Concentration (PCA) (μM/L)	Intensity(PCA)	Concentration (K-fold) (μM/L)	Intensity (K-fold)	Microalbuminuria Grading
1	0.05981252	0.001360709	0.06	0.0014	2+
2	0.08409214	0.005999681	0.085	0.0062	2+
3	0.08409214	0.005999681	0.085	0.0062	2+
4	0.098730964	0.008796639	0.1	0.0091	2+
5	0.11358716	0.011635129	0.115	0.0119	2+
6	0.128441313	0.014473229	0.13	0.0148	2+
7	0.143073718	0.017268961	0.145	0.0176	2+

89

8	0.177793708	0.023902715	0.18	0.0243	3+
9	0.267042658	0.040955013	0.27	0.0415	3+
10	0.358398589	0.05840988	0.36	0.0587	3+
11	0.45251649	0.076392461	0.45	0.0759	4+
12	0.500214243	0.085505804	0.5	0.0854	4+
13	0.600195623	0.104608688	0.6	0.1045	4+
14	0.750257155	0.133280105	0.75	0.1332	4+
15	0.849654035	0.152271311	0.85	0.1523	4+
16	0.900636983	0.162012338	0.9	0.1618	4+
17	1.001690384	0.181320047	1	0.1809	4+
18	1.103352918	0.200744139	1.1	0.2	4+

7.3 Urinalysis Mobile Application

A urinalysis mobile application is specially designed to complete the urinalysis device referred to as uTester. Three design considerations are taken into account to ensure device-agnostic functionality: a) the application needs to be cross-platform including both Android and iOS, b) the application has low requirements on smartphone hardware including CPU, GPU, RAM, and storage, and c) the application adopts a minimal user interface design so that it does not require too much screen real estate and is easy to use by most users.
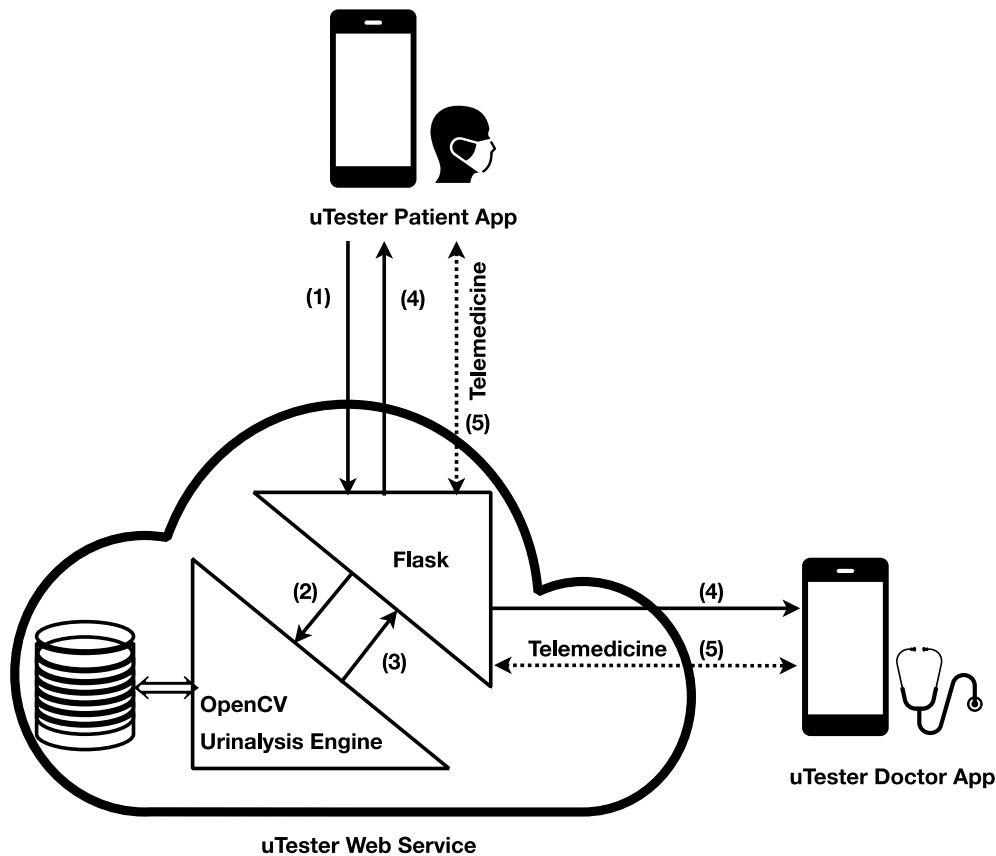
Figure 7- 16: Architecture of the uTester mobile application

The final design is a hybrid thin mobile client—uTester Patient App—that is connected to a uTester Web Service provisioned in the cloud via an Infrastructure as a Service (IaaS) provider (W. Li et al., 2016). The Patient App has two main functions: urinalysis and telemedicine. Figure 7- 16 illustrates the architecture and workflow of the mobile application.

1. The uTester Patient App captures the test image and sends the image to the Web Service.
2. The uTester Web Service, which is developed using Flask (Ronacher, 2010), a micro web framework built in Python for fast development of scalable web applications, receives the

image, checks its validity, stores it in the database, and invokes OpenCV (Open Source Computer Vision Library) (Kaehler & Bradski, 2016), a library of programming functions aimed at real-time computer vision, to process and analyse the image before passing on the retrieved image intensity value to the Urinalysis Engine.

3. The Urinalysis Engine uses the prediction model to derive the albumin level in urine and passes the result on to Flask. Figure 7- 17 shows a linear prediction model (R2 = 0.9828, SSE = 0.00427, and RMSE = 0.007352) with internals:

$$x = \frac{y - a}{b},$$

where y is the image intensity value, x is the predicted albumin level in urine, and a = 0.1909 ∈ [0.1853, 0.1966] and b = -0.01004 ∈ [-0.01204, -0.008043] are the coefficients (with 95% confidence bounds) derived from the training data.

The Concentration Values (μM/L)
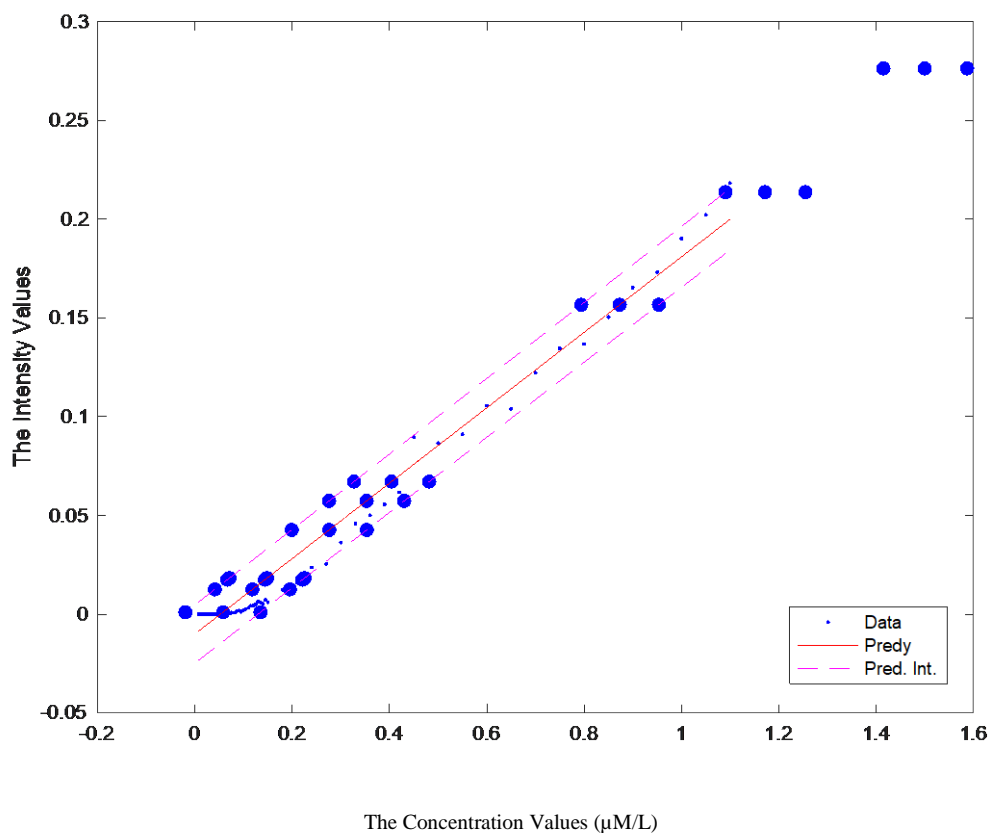
Figure 7- 17: Linear prediction model with internals

4. Flask sends the test result in JSON (JavaScript Object Notation) format back to the Patient App, which displays (as shown in Figure 7- 18 (a)) it to the patient. The result is also sent to the patient's doctor.

5. The doctor uses the uTester Doctor App to perform various telemedicine activities, for instance, electronic consultation (Stoves et al., 2010) where the Doctor App interacts with the Patient App via the uTester Web Service.

This design has a number of advantages, including: a) the native mobile client is simple, easy to develop, and does not require much hardware resource, b) the urinalysis application is adaptable to changes as new image processing and analysis techniques and more accurate urinalysis prediction models can be adopted without the need to update the mobile client, c) the urinalysis application is scalable with the growing number of images and test results, and d) the urinalysis application is resilient to the loss or replacement of smartphone as all the test images and results are securely stored in the cloud. An alternative design would be a fat native mobile application into which all the processing is built and all the data is stored, making it extremely heavyweight, inflexible and vulnerable to device agnosticism.

(a) Display the result   (b) Viewing the trend

Figure 7- 18: The minimal user interface of the uTester native mobile client

A pure web-client, instead of a thin native mobile client, would be naturally cross-platform, however this is not a viable approach, since a web client cannot access a smartphone's camera. Therefore, the native mobile client is implemented separately for Android and iOS devices. The Xamarin platform was used to develop the native mobile clients in order to allow for maximum code sharing between mobile platforms. The Doctor App can be implemented as a pure web client if it does not

need to access the smartphone's built-in sensors or peripheral devices. Although, if electronic consultation requires audiovisual communication between the doctor and the patient, it would have to be implemented as a native mobile client.

Figure 7- 18(a) shows the minimal user interface of the mobile client displaying the current urinalysis result. It uses a traffic light metaphor to visualise the result: red denotes 2+ or above microalbuminuria (>30 mg/dL), yellow denotes 1+ microalbuminuria (20-30 mg/dL), green denotes trace (<20 mg/dL), and grey denotes no trace, followed by explanatory notes elaborating on the current test result. All test images and results are time-stamped and stored in the cloud so that the patient can view their urinalysis trend, as shown in Figure 7- 18(b). Table 7- 6 (referring to Figure 7- 17 Figure 7- 17) shows examples of smartphone-based urinalysis. In particular, for the image intensity of 0.067121of a testing image, its HSA concentration is 0.4041± 0.0772 µM/L, which corresponds to 3+ microalbuminuria, as shown in Figure 7- 18 (a).

Table 7- 6: Examples of smartphone-based urinalysis

Image Intensity	Albumin Level (µM/L)	Lower Bound	Upper Bound	Microalbuminuria Grading
0.00099869	0.057809	-0.01959	0.13495	2+
0.012562	0.11837	0.041103	0.19548	2+
0.017448	0.14396	0.066736	0.22107	2+
0.018262	0.14822	0.071006	0.22534	3+
0.042692	0.27617	0.19905	0.3534	3+
0.057349	0.35293	0.27579	0.43033	3+
0.067121	0.4041	0.32691	0.48165	3+
0.1567	0.87325	0.79418	0.95348	4+
0.2137	1.1718	1.0903	1.2549	4+
0.27637	1.5	1.4149	1.5873	4+

Chapter 8: Conclusions and Future Work

This thesis has presented the design and development of a smartphone-based urinalysis device that provides CKD patients the ability to conduct rapid, quantitative diagnosis of HSA in urine. A key focus in the development of the device was to ensure success was independent of smartphone model. The solution comprises: a custom imaging housing that can be attached to smartphones of varying dimensions and camera positions; image processing and analysis that can retrieve accurate urinalysis data; and, a specially designed, cross-platform urinalysis mobile application. Preliminary evaluation of the device has confirmed its effectiveness in terms of device agnosticism and the viability of a smartphone-based device for point-of-care (POC) quantitative urinalysis.

There are limitations with the current uTester prototype and its underpinning techniques. There is still a long way to go before the device is ready to be used by patients. The first limitation is the ability to only detect HSA. Since HSA concentration in a urine sample is affected by hydration, it is not necessarily the best indicator for CKD. It has become customary to measure albumin-to-creatinine ratio (ACR) as creatinine excretion is considered to be fairly constant throughout the day (Andrassy, 2013). Therefore, as a part of future work, we are in the process of synthesising an aggregation induced emission (AIE)-based creatinine bioprobe.

The second limitation is with regard to the imaging housing. More work is required to make it more affordable, portable, and usable by older people, the main demographic of CKD patients. A systematic evaluation of the device is required that includes testing with more brands of smartphones, verifying device accuracy through controlled artificial urine samples and real urine samples. The evaluation would also include a usability study of the device with regards to the ergonomics of the device, the usability of the mobile application interface, and the physical, physiological, psychological, emotional, and cognitive factors involved in using the device.

An important point is that during the calibration stage, we must understand smartphone image quality and elect images from one smartphone as the reference colours. For instance, for smartphone images, we need to recognise, through the human visual system or the graph model, which one has the widest range of colour intensity, starting with the darkest colour and ending with the brightest colour. Images with narrow ranges of colour intensity may not cover the real intensity values corresponding to the HSA concentration values. Consequently, choosing low quality images as reference colours, the resulting model—the calibrated images—would not cover all levels of CKD, i.e., we may be unable to detect one or more of the five levels of CKD. This knowledge is related to the camera sensor response because some sensors have very high

sensitivity, which would result in intensity values exclusive only in the high range.

Concentration values of HSA were calculated and prepared in the lab with high accuracy, and the concentration values across samples grow steadily and precisely. Though an increment value between each concentration value and the next is very small, the proposed method can estimate all values between these two concentration values via a machine learning technique that estimates concentration value from intensity value and vice versa. This ability to estimate an explicit concentration value is a key contribution of this research. Most traditional methods for determining concentration depend on a table lookup from a reference colour value to a corresponding concentration value. Often the captured image colour may not match any of the reference colours, so the nearest reference colour is chosen. This can result in over or under estimation of HSA concentration rather than representing the real value.

One important observation is that the experiment must be prepared on the same day. Test samples covering all levels must be imaged within the same day with the preference being that imaging occur within one to two hours. The reason for doing this is that the separation of levels in order to be prepared and imaged alone will produce inconsistencies of the image intensity values; such that, the nonlinear relation tends to be fragmented into five separated relations and not as a one continuous relation on the graph.

Also, using three mobiles for imaging may not obtain precise results because as the number of mobiles increases in the experiment, the number of resulting relations increases too. This gives more opportunity to elect the best relation to represent a robust model for the calibration process while neglecting the worst curve relation(s).

Often PCA and K-fold supervised machine learning affect the resulting linear relation. Image intensity values for the first two levels may be negative, losing the ability to classify the Trace and 1+ levels. Therefore, about five test images must be captured before adding HSA and AIE. On the other hand, for the prepared samples, it is preferred not to exceed fifteen samples for each level for time, effort and consistency reasons.

8   Bibliography

Agu, E., Pedersen, P., Strong, D., Tulu, B., He, Q., Wang, L., & Li, Y. (2013). *The smartphone as a medical device: Assessing enablers, benefits and challenges.* Paper presented at the Sensor, Mesh and Ad Hoc Communications and Networks (SECON), 2013 10th Annual IEEE Communications Society Conference on.

Akraa, S., Tam, A. P. T., Shen, H., Tang, Y., Tang, B. Z., Li, J., & Walker, S. (2018). A smartphone-based point-of-care quantitative urinalysis device for chronic kidney disease patients. Journal of Network and Computer Applications, 115, 59-69.

Alpaydin, E. (2010). Introduction to Machine Learning. [Sl]: The MIT Press.

Andrassy, K. M. (2013). Comments on 'KDIGO 2012 clinical practice guideline for the evaluation and management of chronic kidney disease'. Kidney international, 84(3), 622-623

Archibong, E., Konnaiyan, K. R., Kaplan, H., & Pyayt, A. (2017). A mobile phone-based approach to detection of hemolysis. *Biosensors and Bioelectronics, 88*, 204-209.

Au, PPY. (2013). 'HDR luminance measurement: Comparing real and simulated data', University of Wellington.

Bigas, M., Cabruja, E., Forest, J., & Salvi, J. (2006). Review of CMOS image sensors.*Microelectronics journal, 37*(5), 433-451.

Bingham, N. H., & Fry, J. M. (2010). *Regression: Linear models in statistics*: Springer Science & Business Media.

Boulos, M. N. K., Wheeler, S., Tavares, C., & Jones, R. (2011). How smartphones are changing the face of mobile and participatory healthcare: an overview, with example from eCAALYX. *Biomedical engineering online, 10*(1), 24.

Bourouis, A., Zerdazi, A., Feham, M., & Bouchachia, A. (2013). M-health: skin disease analysis system using smartphone's camera. *Procedia Computer Science, 19*, 1116-1120.

Brandtweiner, R., Donat, E., & Kerschbaum, J. (2010). How to become a sophisticated user: a two-dimensional approach to e-literacy. New media & society, 12(5), 813-833.

Bravo, I., Baliñas, J., Gardel, A., Lázaro, J. L., Espinosa, F., & García, J. (2011). Efficient smart CMOS camera based on FPGAs oriented to embedded image processing. *Sensors, 11*(3), 2282-2303.

Bueno, D., Muñoz, R., & Marty, J. L. (2016). Fluorescence analyzer based on smartphone camera and wireless for detection of Ochratoxin A. *Sensors and actuators B: Chemical, 232*, 462-468.

Cao, Y., Pan, X., Zhao, X., & Wu, H. (2014). An analog gamma correction scheme for high dynamic range CMOS logarithmic image sensors. *Sensors, 14*(12), 24132-24145.

Celler, B. G., & Sparks, R. S. (2015). Home Telemonitoring of Vital Signs—Technical Challenges and Future Directions. *IEEE journal of biomedical and health informatics, 19*(1), 82-91.

Cevenini, L., Calabretta, M. M., Tarantino, G., Michelini, E., & Roda, A. (2016). Smartphone-interfaced 3D printed toxicity biosensor integrating bioluminescent "sentinel cells". *Sensors and actuators B: Chemical, 225*, 249-257.

Chen, Q., Yan, B. F., Liao, J., & An, G. (2013). *Analysis of mobile phone camera performance estimation method.* Paper presented at the Applied Mechanics and Materials.

Chen, T., Xie, N., Viglianti, L., Zhou, Y., Tan, H., Tang, B. Z., & Tang, Y. (2017). Quantitative urinalysis using aggregation-induced emission bioprobes for monitoring chronic kidney disease. Faraday discussions, 196, 351-362.

Chen, X., He, L., Jeon, G., & Jeong, J. (2014). Local adaptive directional color filter array interpolation based on inter-channel correlation. Optics Communications, 324, 269-276.

Chiu, S.-H., & Urban, P. (2015). Fusion of microlitre water-in-oil droplets for simple, fast and green chemical assays. *Analyst, 140*(15), 5145-5151.

Choubey, B & Gouveia, L. (2014). 'On evolution of CMOS image sensors'. http://eprints.gla.ac.uk/96924/1/96924.pdf

Chutipongtanate, S., & Thongboonkerd, V. (2010). Systematic comparisons of artificial urine formulas for in vitro cellular study. Analytical biochemistry, 402(1), 110-112.

Cohen, R., & Wang, T. (2014). Intel embedded hardware platform *Android Application Development for the Intel® Platform* (pp. 19-46): Springer.

Cold Spring Harbor Protocols. ([cited 23/11/2017]).

Collings, S., Thompson, O., Hirst, E., Goossens, L., George, A., & Weinkove, R. (2016). Non-invasive detection of anaemia using digital photographs of the conjunctiva. *PloS one, 11*(4), e0153286.

Coresh, J., Astor, B. C., Greene, T., Eknoyan, G., & Levey, A. S. (2003). Prevalence of chronic kidney disease and decreased kidney function in the adult US population: Third National Health and Nutrition Examination Survey. *American journal of kidney diseases, 41*(1), 1-12.

Coskun, A. F., Nagi, R., Sadeghi, K., Phillips, S., & Ozcan, A. (2013). Albumin testing in urine using a smart-phone. *Lab on a Chip, 13*(21), 4231-4238.

Couser, W. G., Remuzzi, G., Mendis, S., & Tonelli, M. (2011). The contribution of chronic kidney disease to the global burden of major noncommunicable diseases. *Kidney international, 80*(12), 1258-1270.

Cruz-Fernández, M., Luque-Cobija, M., Cervera, M., Morales-Rubio, A., & de la Guardia, M. (2017). Smartphone determination of fat in cured meat products. *Microchemical Journal, 132*, 8-14.

Dang, D., Cho, C. H., Kim, D., Kwon, O. S., & Chong, J. W. (2017). *Efficient color correction method for smartphone camera-based health monitoring application.* Paper presented at the Engineering in Medicine and Biology Society (EMBC), 2017 39th Annual International Conference of the IEEE.

Debus, B., Kirsanov, D., Yaroshenko, I., Sidorova, A., Piven, A., & Legin, A. (2015). Two low-

cost digital camera-based platforms for quantitative creatinine analysis in urine. *Analytica chimica acta, 895*, 71-79.

Diamantidis, C. J., & Becker, S. (2014). Health information technology (IT) to improve the care of patients with chronic kidney disease (CKD). *BMC nephrology, 15*(1), 7.

Ekstrom, MP. (2012). Digital image processing techniques, vol. 2, Academic Press.

El Kaoutit, H., Estévez, P., García, F. C., Serna, F., & García, J. M. (2013). Sub-ppm quantification of Hg (II) in aqueous media using both the naked eye and digital information from pictures of a colorimetric sensory polymer membrane taken with the digital camera of a conventional mobile phone. *Analytical Methods, 5*(1), 54-58.

Ellis, R., & Mookim, P. (2013). *K-Fold Cross-Validation is Superior to Split Sample Validation for Risk Adjustment Models*. Retrieved from

Farid, H. (2001). Blind inverse gamma correction. *IEEE Transactions on Image Processing, 10*(10), 1428-1433.

Ford, A., & Roberts, A. (1998). Colour space conversions. *Westminster University, London, 1998*, 1-31.

Ginardi, R. H., Saikhu, A., Sarno, R., Sunaryono, D., Kholimi, A. S., & Shanty, R. N. T. (2014). *Intelligent Method for Dipstick Urinalysis Using Smartphone Camera*. Paper presented at the Information and Communication Technology-EurAsia Conference.

Global Urinalysis Market: Rising Demand for Point-of-care Testing (POCT) Strongly Impacting Growth, Notes TMR. ((2016, October 04), Oct 4, 2016). PR Newswire, p. PR Newswire,.

Gupta, D., Khare, S., & Aggarwal, A. (2016). *A method to predict diagnostic codes for chronic diseases using machine learning techniques*. Paper presented at the Computing, Communication and Automation (ICCCA), 2016 International Conference on.

Gupta, S., Liaw, H. C., Vadakkepat, P., & Starmer, C. F. (2015). *Smartphone spectrophotometer for point-of-care diagnostics in low-resource settings*. Paper presented at the Humanitarian Technology Conference (R10-HTC), 2015 IEEE Region 10.

Hamer, R. A., & El Nahas, A. M. (2006). The burden of chronic kidney disease. *Bmj, 332*(7541), 563-564.

Herman, B., Lakowicz, J., Murphy, D., Fellers, T. J., & Davidson, M. W. (2009). Fluorescence excitation and emission fundamentals.

Holms, A., & Quach, A. (2010). Complementary Metal-Oxide Semiconductor Sensors.

Hoy, W. E., Wang, Z., Baker, P. R., Mcdonald, S. M., & Mathews, J. D. (2001). The natural history of renal disease in Australian Aborigines. Part 2. Albuminuria predicts natural death and renal failure. *Kidney international, 60*(1), 249-256.

Huang, B.-C., & Fuh, C.-S. (2005). *Image pipeline algorithms for standard mobile imaging architecture sensors*. Paper presented at the 18th IPPR Conference on Computer Vision, Graphics and Image Processing (CVGIP 2005).

Ilie, A., & Welch, G. (2005). *Ensuring color consistency across multiple cameras.* Paper presented at the Computer Vision, 2005. ICCV 2005. Tenth IEEE International Conference on.

Iseki, K., Ikemiya, Y., Iseki, C., & Takishita, S. (2003). Proteinuria and the risk of developing end-stage renal disease. *Kidney international, 63*(4), 1468-1474.

Jahanirad, M., Wahab, A. W. A., & Anuar, N. B. (2016). An evolution of image source camera attribution approaches. *Forensic science international, 262*, 242-275.

Jayashree, R. A. (2013). *RGB to HSI color space conversion via MACT algorithm.* Paper presented at the Communications and Signal Processing (ICCSP), 2013 International Conference on.

Jiang, H., Tian, Q., Farrell, J., & Wandell, B. (2017). Learning the image processing pipeline. *IEEE Transactions on Image Processing*.

Johnson, D. (2004). Evidence-based guide to slowing the progression of early renal insufficiency. *Internal medicine journal, 34*(1-2), 50-57.

Joshi, N., & Jensen, H. (2004). Color calibration for arrays of inexpensive image sensors. *Stanford University, Tech. Rep.*

Juang, J.-G., Tsai, Y.-J., & Fan, Y.-W. (2015). Visual Recognition and Its Application to Robot Arm Control. *Applied Sciences, 5*(4), 851-880.

Kaehler, A., & Bradski, G. (2016). Learning OpenCV 3: computer vision in C++ with the OpenCV library: " O'Reilly Media, Inc.".

Karlen, W., Ansermino, J. M., Dumont, G. A., & Scheffer, C. (2013). *Detection of the optimal region of interest for camera oximetry.* Paper presented at the Engineering in Medicine and Biology Society (EMBC), 2013 35th Annual International Conference of the IEEE.

Keane, W. F., & Eknoyan, G. (1999). Proteinuria, albuminuria, risk, assessment, detection, elimination (PARADE): a position paper of the National Kidney Foundation. *American journal of kidney diseases, 33*(5), 1004-1010.

Kessler, M. A., Meinitzer, A., Petek, W., & Wolfbeis, O. S. (1997). Microalbuminuria and borderline-increased albumin excretion determined with a centrifugal analyzer and the Albumin Blue 580 fluorescence assay. Clinical Chemistry, 43(6), 996-1002.

Kharrazi, H., Chisholm, R., VanNasdale, D., & Thompson, B. (2012). Mobile personal health records: An evaluation of features and functionality. *International journal of medical informatics, 81*(9), 579-593.

Kim, E.-S., Jang, S.-W., Lee, S.-H., Song, I.-H., & Sohng, K.-I. (2006). *Color Correction for the Mobile Phone Camera.* Paper presented at the IPCV.

Kim, S. C., Jalal, U. M., Im, S. B., Ko, S., & Shim, J. S. (2017). A smartphone-based optical platform for colorimetric analysis of microfluidic device. *Sensors and actuators B: Chemical, 239*, 52-59.

Kim, S. D., Koo, Y., & Yun, Y. (2017). A Smartphone-Based Automatic Measurement Method for Colorimetric pH Detection Using a Color Adaptation Algorithm. *Sensors, 17*(7), 1604.

Kim, U., Ghanbari, S., Ravikumar, A., Seubert, J., & Figueira, S. (2013). Rapid, Affordable, and Point-of-Care Water Monitoring Via a Microfluidic DNA Sensor and a Mobile Interface for Global Health. *Translational Engineering in Health and Medicine, IEEE Journal of, 1*, 1-7.

Lahuerta-Zamora, L., & Mellado-Romero, A. M. (2017). Video approach to chemiluminescence detection using a low-cost complementary metal oxide semiconductor (CMOS)-based camera: determination of paracetamol in pharmaceutical formulations. *Analytical and bioanalytical chemistry, 409*(15), 3891-3898.

Landman, A., Emani, S., Carlile, N., Rosenthal, D., Semakov, S., Pallin, D., & Poon, E. A mobile app for securely capturing and transferring clinical images to the electronic health record: Description and preliminary usability study. JMIR Mhealth Uhealth. 2015; 3 (1): e1. doi: 10.2196/mhealth. 3481.

Lee, D.-S., Jang, W. I., Jung, M. Y., Jeon, B. G., & Ihm, C. (2011). *A pocket-sized colorimetric urine reader for telemedicine in the developing countries.* Paper presented at the Sensors, 2011 IEEE.

Lenart, M., Mascarenhas, N., Xiong, R., & Flower, A. (2016). *Identifying risk of progression for patients with Chronic Kidney Disease using clustering models.* Paper presented at the Systems and Information Engineering Design Symposium (SIEDS), 2016 IEEE.

Levey, A. S., Eckardt, K.-U., Tsukamoto, Y., Levin, A., Coresh, J., Rossert, J., . . . Eknoyan, G. (2005). Definition and classification of chronic kidney disease: a position statement from Kidney Disease: Improving Global Outcomes (KDIGO). *Kidney international, 67*(6), 2089-2100.

Li, K., Dai, Q., & Xu, W. (2011). Collaborative color calibration for multi-camera systems. *Signal Processing: Image Communication, 26*(1), 48-60.

Li, W., Wu, L., Xia, Y., Wang, Y., Guo, K., Luo, X., . . . Zheng, W. (2016). On stochastic performance and cost-aware optimal capacity planning of unreliable infrastructure-as-a-service cloud. Paper presented at the International Conference on Algorithms and Architectures for Parallel Processing.

Lin, T., Liao, B.-H., Hsu, S.-L., & Wang, J. (2015). *Experimental investigation of HSL color model in error diffusion.* Paper presented at the Ubi-Media Computing (UMEDIA), 2015 8th International Conference on.

Maddalena, S., Darmon, A., & Diels, R. (2005). Automotive CMOS image sensors *Advanced Microsystems for Automotive Applications 2005* (pp. 401-412): Springer.

Madooei, A., & Drew, M. S. (2016). Incorporating colour information for computer-aided diagnosis of melanoma from dermoscopy images: a retrospective survey and critical analysis. *International journal of biomedical imaging, 2016*.

Martinez, A. W., Phillips, S. T., Carrilho, E., Thomas III, S. W., Sindi, H., & Whitesides, G. M. (2008). Simple telemedicine for developing regions: camera phones and paper-based microfluidic devices for real-time, off-site diagnosis. *Analytical Chemistry, 80*(10), 3699-3707.

Matasaru, C. (2014). 'Mobile Phone Camera Possibilities for Spectral Imaging', Master thesis, University of Eastern

Mei, Q., Jing, H., Li, Y., Yisibashaer, W., Chen, J., Li, B. N., & Zhang, Y. (2016). Smartphone based visual and quantitative assays on upconversional paper sensor. *Biosensors and Bioelectronics, 75*, 427-432.

Menesatti, P., Angelini, C., Pallottino, F., Antonucci, F., Aguzzi, J., & Costa, C. (2012). RGB color calibration for quantitative image analysis: the "3D Thin-Plate Spline" warping approach. *Sensors, 12*(6), 7063-7079.

Monošík, R., dos Santos, V. B., & Angnes, L. (2015). A simple paper-strip colorimetric method utilizing dehydrogenase enzymes for analysis of food components. *Analytical Methods, 7*(19), 8177-8184.

Moonrungsee, N., Pencharee, S., & Peamaroon, N. (2016). Determination of iron in zeolite catalysts by a smartphone camera-based colorimetric analyzer. *Instrumentation Science & Technology, 44*(4), 401-409.

Mosa, A. S. M., Yoo, I., & Sheets, L. (2012). A systematic review of healthcare applications for smartphones. *BMC medical informatics and decision making, 12*(1), 67.

Nematzadeh, Z., Ibrahim, R., & Selamat, A. (2015). *Comparative studies on breast cancer classifications with k-fold cross validations using machine learning techniques.* Paper presented at the Control Conference (ASCC), 2015 10th Asian.

Neumeyer, J., Prince, J., Miller, A., Koeneman, B., Figueria, S., & Kim, U. (2016). *Mobile urinalysis for maternal screening: Frugal medical screening solution and patient database to aid in prenatal healthcare for expecting mothers in the developing world.* Paper presented at the Global Humanitarian Technology Conference (GHTC), 2016.

Nour Abura'ed, H. B., Faisal Khan. (2016). High-ISO Image De-noising Using Burst Filte. IEEE(59th).

Of, O. (2013). Kidney Disease: Improving Global Outcomes (KDIGO) CKD Work Group. KDIGO 2012 Clinical Practice Guideline for the Evaluation and Management of Chronic Kidney Disease. *Kidney Int. Suppl, 3*, 150.

ON Semiconductor. (2015). TND6114 - Image Sensor Color Correction. Retrieved from http://www.onsemi.com/PowerSolutions/extSearch.do?query=TND6114&param1=type&param1_val=document

Oncescu, V., Mancuso, M., & Erickson, D. (2014). Cholesterol testing on a smartphone. *Lab on a Chip, 14*(4), 759-763.

Park, Y. M., Han, Y. D., Chun, H. J., & Yoon, H. C. (2017). Ambient light-based optical biosensing platform with smartphone-embedded illumination sensor. *Biosensors and Bioelectronics, 93*, 205-211.

Peltoketo, V.-T. (2016). *Benchmarking of Mobile Phone Cameras.* Doctoral thesis in pre-examination phase.

Pike, T. W. (2011). Using digital cameras to investigate animal colouration: estimating sensor

sensitivity functions. *Behavioral Ecology and Sociobiology, 65*(4), 849-858.

Pitas, I. (2000). Digital image processing algorithms and applications, John Wiley & Sons.

Priye, A., & Ugaz, V. (2016). DNA-TO-GO: a portable smartphone-enabled PCR assay platform. *arXiv preprint arXiv:1606.02252*.

Priye, A., Wong, S., Bi, Y., Carpio, M., Chang, J., Coen, M., . . . Keller, A. (2016). Lab-on-a-drone: toward pinpoint deployment of smartphone-enabled nucleic acid-based diagnostics for mobile health care. *Analytical Chemistry, 88*(9), 4651-4660.

Priye, A, Bird, SW, Light, YK, Ball, CS, Negrete, OA & Meagher, RJ 2017, 'A smartphone-based diagnostic platform for rapid detection of Zika, chikungunya, and dengue viruses', Scientific Reports, vol. 7, p. 44778.

Qiu, X., Ge, S., Gao, P., Li, K., Yang, S., Zhang, S., . f. . Qian, S. (2017). A smartphone-based point-of-care diagnosis of H1N1 with microfluidic convection PCR. *Microsystem Technologies, 23*(7), 2951-2956.

Rauh, S. P., Rutters, F., van der Heijden, A. A., Luimes, T., Alssema, M., Heymans, M. W., . . . Dekker, J. M. (2018). External validation of a tool predicting 7-year risk of developing cardiovascular disease, type 2 diabetes or chronic kidney disease. *Journal of general internal medicine, 33*(2), 182-188.

Refaeilzadeh, P., Tang, L., & Liu, H. (2009). Cross-validation *Encyclopedia of database systems* (pp. 532-538): Springer.

Richardson, M., 2009. Principal component analysis. URL: http://people. maths. ox. ac. uk/richardsonm/SignalProcPCA. pdf (last access: 3.5. 2013). Aleš Hladnik Dr., Ass. Prof., Chair of Information and Graphic Arts Technology, Faculty of Natural Sciences and Engineering, University of Ljubljana, Slovenia ales. uni-lj. si, 6, p.16.

Rigon, J., Capuani, S., Fernandes, D., & Guimarães, T. (2016). A novel method for the estimation of soybean chlorophyll content using a smartphone and image analysis. Photosynthetica, 54(4), 559-566.
Ronacher, A. (2010). Welcome—flask (a python microframework). URL: http://flask. pocoo. org/(visited on 02/02/2015), 38.

Rigon, J., Capuani, S., Fernandes, D., & Guimarães, T. (2016). A novel method for the estimation of soybean chlorophyll content using a smartphone and image analysis. *Photosynthetica, 54*(4), 559-566.

Ruggenenti, P., Gaspari, F., Perna, A., & Remuzzi, G. (1998). Cross sectional longitudinal study of spot morning urine protein: creatinine ratio, 24 hour urine protein excretion rate, glomerular filtration rate, and end stage renal failure in chronic renal disease in patients without diabetes. *Bmj, 316*(7130), 504-509.

Saad, A.-A., Khalid, C., & Mohamed, J. (2015). *Network intrusion detection system based on Direct LDA*. Paper presented at the Complex Systems (WCCS), 2015 Third World Conference on.

Sanz, I., Museros, L., Falomir, Z., & Gonzalez-Abril, L. (2015). Customising a qualitative colour description for adaptability and usability. *Pattern Recognition Letters, 67*, 2-10.

Sari, Y. A., Ginardi, R. H., & Sarno, R. (2013). Assessment of color levels in leaf color chart using smartphone camera with relative calibration. *ISICO 2013, 2013*.

Semiconductor- Memory Chip Companies: Patent Issued for Image Sensor, Operation Method Thereof, and System Including the Same (USPTO 9204143). ((2015, December 15)). Electronics Newsweekly(2015).

Shahriyar, R., Bari, M. F., Kundu, G., Ahamed, S. I., & Akbar, M. M. (2009). *Intelligent mobile health monitoring system (IMHMS).* Paper presented at the International Conference on Electronic Healthcare.

Sherman, D., & Farrell, J. E. (1994). *When to use linear models for color calibration.* Paper presented at the Color and Imaging Conference.

Shi, Y., Yang, J., & Wu, R. (2007). *Reducing illumination based on nonlinear gamma correction.* Paper presented at the Image Processing, 2007. ICIP 2007. IEEE International Conference on.

Sicat, R., Tangonan, G. L., Guico, M., Libatique, N. J., Ramos, C., Siapno, M., . . . Velasquez, K. (2009). Patient-Centric Medical Database with Remote Urinalysis Test. Paper presented at the Computer Science and Information Engineering, 2009 WRI World Congress on.

simiconductor, o. Image Sensor Color Correction.

Skandarajah, A., Reber, C. D., Switz, N. A., & Fletcher, D. A. (2014). Quantitative imaging with a mobile phone microscope. *PloS one, 9*(5), e96906.

Slavkovikj, V. (2011). *Color calibration of a multi-camera array.* Masters thesis, Gjøvik university college, Norway.

Soares, S., Lima, M. J., & Rocha, F. R. (2017). A spot test for iodine value determination in biodiesel based on digital images exploiting a smartphone. *Microchemical Journal, 133*, 195-199.

Solomon, D. E., Abdel-Raziq, A., & Vanapalli, S. A. (2016). A stress-controlled microfluidic shear viscometer based on smartphone imaging. *Rheologica Acta, 55*(9), 727-738.

Soria-Olivas, E., Martín-Guerrero, J. D., Redón, J., Tellez-Plaza, M., & Vila-Francés, J. (2015). *Improving mortality prediction in cardiovascular risk patients by balancing classes.* Paper presented at the Data Mining Workshop (ICDMW), 2015 IEEE International Conference on.

Spyrou, E. M., Kalogianni, D. P., Tragoulias, S. S., Ioannou, P. C., & Christopoulos, T. K. (2016). Digital camera and smartphone as detectors in paper-based chemiluminometric genotyping of single nucleotide polymorphisms. *Analytical and bioanalytical chemistry, 408*(26), 7393-7402.

Stankevich, E., Paramonov, I., & Timofeev, I. (2012). *Mobile phone sensors in health applications.* Paper presented at the Proceeding of the 12th Conference of FRUCT Association.

Stoves, J., Connolly, J., Cheung, C. K., Grange, A., Rhodes, P., O'donoghue, D., & Wright, J. (2010). Electronic consultation as an alternative to hospital referral for patients with chronic kidney disease: a novel application for networked electronic health records to improve the accessibility and efficiency of healthcare. Qual Saf Health Care, 19(5), e54-e54.

Sumner, R. (2014). Processing raw images in matlab. *Department of Electrical Engineering, University of California Sata Cruz*.

Suryanarayana, T., & Mistry, P. (2016). *Principal component regression for crop yield estimation*: Springer.

Tai, S.-C., Liao, T.-W., Chang, Y.-Y., & Yeh, C.-P. (2012). *Automatic White Balance algorithm through the average equalization and threshold.* Paper presented at the Information Science and Digital Content Technology (ICIDT), 2012 8th International Conference on.

Takahashi, Y., & Chikatsu, H. (2015). Camera Calibration for Uav Application Using Sensor of Mobile Camera. *The International Archives of Photogrammetry, Remote Sensing and Spatial Information Sciences, 40*(4), 239.

Thanakiatkrai, P., Yaodam, A., & Kitpipit, T. (2013). Age estimation of bloodstains using smartphones and digital image analysis. *Forensic science international, 233*(1), 288-297.

Tong, H., Hong, Yuning, Dong, Yongqiang, Häussler, Matthias, Li, Zhen, Lam, Jacky W Y, . . . Tang, Ben Zhong,. ((2007)). Protein detection and quantitation by tetraphenylethene-based fluorescent probes with aggregation-induced emission characteristics. The Journal of Physical Chemistry(B, 111(40)), 11817-11823.

Trappey, AJ, Trappey, CV, Fan, C-Y & Lee, IJ. (2018). 'Consumer driven product technology function deployment using social media and patent mining', Advanced Engineering Informatics, vol. 36, pp. 120-9.

Tsamardinos, I., Rakhshani, A., & Lagani, V. (2014). *Performance-Estimation Properties of Cross-Validation-Based Protocols with Simultaneous Hyper-Parameter Optimization.* Paper presented at the SETN.

Tsin, Y., Ramesh, V., & Kanade, T. (2001). *Statistical calibration of CCD imaging process.* Paper presented at the Computer Vision, 2001. ICCV 2001. Proceedings. Eighth IEEE International Conference on.

Vacher, M., Istrate, D., Besacier, L., Castelli, E., & Serignat, J.-F. (2003). *Smart audio sensor for telemedicine.* Paper presented at the Smart Object Conference ({SOC}'2003).

Vasinek, M., Plato, J., & Snasel, V. (2016). *Limitations on Low Variance k-Fold Cross Validation in Learning Set of Rules Inducers.* Paper presented at the Intelligent Networking and Collaborative Systems (INCoS), 2016 International Conference on.

Velikova, M., Lucas, P. J., Smeets, R. L., & van Scheltinga, J. T. (2012). *Fully-automated interpretation of biochemical tests for decision support by smartphones.* Paper presented at the Computer-Based Medical Systems (CBMS), 2012 25th International Symposium on.

Wang, Z., Wang, Q., Xu, Z., & Huang, W. (2017). *Visible Light Communications: Modulation*

and Signal Processing: John Wiley & Sons.

Webster, M., Raguse, B., Wieczorek, L., Cooper, J., Chow, E., & Hubble, L. (2012). Towards an inexpensive sensor technology for disease detection in developing countries.

Weiner, DE, Tighiouart, H, Amin, MG, Stark, PC, MacLeod, B, Griffith, JL, Salem, DN, Levey, AS & Sarnak, MJ. (2004). 'Chronic kidney disease as a risk factor for cardiovascular disease and all-cause mortality: a pooled analysis of community-based studies', Journal of the American Society of Nephrology, vol. 15, no. 5, pp. 1307-15.

Wei, M., Huang, S., Wang, J., Li, H., Yang, H., & Wang, S. (2015). The study of liquid surface waves with a smartphone camera and an image recognition algorithm. *European Journal of Physics, 36*(6), 065026.

White, S. L., Polkinghorne, K. R., Atkins, R. C., & Chadban, S. J. (2010). Comparison of the prevalence and mortality risk of CKD in Australia using the CKD Epidemiology Collaboration (CKD-EPI) and Modification of Diet in Renal Disease (MDRD) Study GFR estimating equations: the AusDiab (Australian Diabetes, Obesity and Lifestyle) Study. *American journal of kidney diseases, 55*(4), 660-670.

White, S. L., Yu, R., Craig, J. C., Polkinghorne, K. R., Atkins, R. C., & Chadban, S. J. (2011). Diagnostic accuracy of urine dipsticks for detection of albuminuria in the general community. *American journal of kidney diseases, 58*(1), 19-28.

Wiens, K., Green, S., & Grecov, D. (2014). Novel optical uroflowmeter using image processing techniques. *Measurement, 47*, 314-320.

Winocour, P. (1992). Microalbuminuria. *BMJ: British Medical Journal, 304*(6836), 1196.

Xiao, F., Farrell, J. E., DiCarlo, J. M., & Wandell, B. A. (2003). *Preferred color spaces for white balancing.* Paper presented at the Electronic Imaging 2003.

Yang, Z., & Zhan, Q. (2016). Single-Shot Smartphone-Based Quantitative Phase Imaging Using a Distorted Grating. *PloS one, 11*(7), e0159596.

Yetisen, A. K., Martinez-Hurtado, J., Garcia-Melendrez, A., da Cruz Vasconcellos, F., & Lowe, C. R. (2014). A smartphone algorithm with inter-phone repeatability for the analysis of colorimetric tests. *Sensors and actuators B: Chemical, 196*, 156-160.

Yoo, Y., Lee, S., Choe, W., & Kim, C.-Y. (2007). *CMOS image sensor noise reduction method for image signal processor in digital cameras and camera phones.* Paper presented at the Digital Photography.

Yoon, K., Kim, C., Lee, B., & Lee, D. (2002). Single-chip CMOS image sensor for mobile applications. *IEEE Journal of Solid-State Circuits, 37*(12), 1839-1845.

Zar, J. H., Córdoba-Pachón, José-Rodrigo, & Ochoa-Arias, Alejandro,. (2010). Biostatistical analysis (5th ed ed.). Upper Saddle River, N.J. : Prentice Hall.

Zhang, B., & Batur, A. U. (2012). *A real-time auto white balance algorithm for mobile phone cameras.* Paper presented at the Consumer Electronics (ICCE), 2012 IEEE International Conference on.

Zhang, Y., Wu, Y., Zhang, Y., & Ozcan, A. (2016). Color calibration and fusion of lens-free and mobile-phone microscopy images for high-resolution and accurate color reproduction. *Scientific reports, 6*.